Immune modulating nanomedicine for cancer metabolism reprogramming and rheumatoid arthritis vaccination

암 대사 리프로그래밍 및 류마티스 관절염 백신을
위한 면역조절 나노의약품의 활용

2023년 8월

서울대학교 대학원

약학과 약제학 전공

YINA WU

Immune modulating nanomedicine for cancer metabolism reprogramming and rheumatoid arthritis vaccination

암 대사 리프로그래밍 및 류마티스 관절염 백신을
위한 면역조절 나노의약품의 활용

지도 교수 김 대 덕

이 논문을 약학박사 학위논문으로 제출함
2023년 5월

서울대학교 대학원
약학과 약제학 전공
YINA WU

YINA WU의 약학박사 학위논문을 인준함
2023년 7월

위 원 장 _____ 변 영 로 _____ (인)

부위원장 _____ 이 우 인 _____ (인)

위   원 _____ 윤 유 석 _____ (인)

위   원 _____ 심 가 용 _____ (인)

위   원 _____ 김 대 덕 _____ (인)

Abstract

Immune modulating nanomedicine for cancer metabolism reprogramming and rheumatoid arthritis vaccination

YINA WU

Department of Pharmacy

Pharmaceutics Major

The Graduate School

Seoul National University

The immune system plays a vital role in safeguarding the body against pathogens and a broad spectrum of diseases. However, when the immune system malfunctions, an imbalance can occur, resulting in either an overactive or underactive immune response. For example, in the context of cancer, the immune system fails to recognize and eliminate abnormal cells, enabling their aggressive growth. In autoimmune diseases, the immune system mistakenly recognizes healthy cells and tissues as foreign invaders, leading to an immune response against them. Consequently, it becomes crucial to modulate the function of immune system to address diverse conditions in cancer and autoimmune disease therapies. Nanomedicine, an exciting field harnessing nanotechnology, holds promise for developing innovative diagnostic and therapeutic tools. By designing nanomaterials, specific immune cells or tissues can be targeted, facilitating the delivery of therapeutic agents to the desired locations. In this Ph.D. dissertation, three nano-delivery systems have been developed to overcome the limitations associated with current immunotherapeutic approaches in cancer and autoimmune disease therapy by effectively modulating immune cells.

In Chapter 1, the current immunotherapy for cancer and autoimmune disease treatment was reviewed. Additionally, the limitations of these approaches in their current status were mentioned, emphasizing the importance of developing nano-delivery systems to effectively modulate immune cells and overcome these challenges.

In Chapter 2, the anticancer functions of T cells were activated by inducing lipid metabolic reprogramming within the glucose-deficient tumor microenvironment using nanomedicine. To achieve this, fenofibrate was encapsulated in poly (γ-glutamic acid)-based nanoparticles (F/ANs), and the surfaces of F/ANs were modified with an anti-CD3e f(ab')2 fragment,

resulting in aCD3/F/ANs. Through the stimulation of fatty acid metabolism, aCD3/F/ANs supported T cell proliferation within the hypoglycemic tumor microenvironment. The treatment of tumor-bearing mice with aCD3/F/ANs enhanced cytokine production within tumor tissues and prevented tumor growth. This study highlights the potential of nanomedicine-enabled fatty acid metabolic reprogramming of tumor-infiltrating lymphocytes as a novel approach to overcome the challenge of nutrient deficiency in immunotherapy.

In Chapter 3, a cationic lipid nanoparticle modified with mannose (M-NP) was developed to deliver the nucleic acid adjuvant polyinosinic:polycytidylic acid (PIC) specifically to antigen-presenting cells. The PIC-loaded M-NP (PIC/M-NP) exhibited stable lipoplexes irrespective of the ligand ratio and showed minimal cytotoxicity in bone marrow-derived dendritic cells (BMDCs). This study demonstrated the uptake of PIC/M-NP by DCs, and an increased mannose ligand ratio improved the efficiency of DC uptake. Moreover, PIC/M-NP significantly enhanced the maturation of BMDCs, and subcutaneous injection of PIC/M-NP in mice facilitated lymphatic delivery and DC activation upon NP uptake. These findings highlight the potential of PIC/M-NP as a promising vaccine delivery system in immunotherapy.

In Chapter 4, a nanovaccine based on tannic acid for the treatment of rheumatoid arthritis was designed, aiming to induce antigen-specific immune tolerance. The nanovaccine, known as CitDTN, was engineered to deliver dexamethasone and citrullinated peptide in a lipid-coated nanoparticle, with tannic acid serving as the core material. The surface of CitDTN was then modified with abatacept, resulting in AbaCitDTN. AbaCitDTN successfully reshaped the properties of dendritic cells towards tolerogenic phenotypes, disrupting the co-stimulatory signals between DCs and T cells. This intervention resulted in suppressed T cell proliferation and reduced secretion of IL-2. In a collagen-induced arthritis DBA/1 mouse model, AbaCitDTN was subcutaneously administered on a weekly basis, totaling four injections. This treatment led to diminished inflammation within the synovial space and decreased autoimmunity against type II collagen and citrullinated peptide. Notably, in vivo administration of AbaCitDTN improved clinical symptoms and provided joint protection against destruction in this animal model. These findings indicate the potential of tannic acid-based nanomaterials to induce antigen-specific immune tolerance as a viable therapeutic approach for rheumatoid arthritis, without causing severe systemic immune suppression that is associated with the side effects of current autoimmune disease immunotherapy.

Keyword: nanomedicine, immunomodulation, metabolic reprogramming, tolerogenic vaccine, cancer, rheumatoid arthritis
Student Number: 2017-28204

Table of Contents

List of Tables

Chapter 4

List of Figures

Chapter 1

Chapter 2

Chapter 3

Chapter 4

Chapter 1

Overview

Chapter 1. Overview

1.1. Imbalance of the immune system

The immune system is responsible for defending the body against pathogens and providing protection against diverse diseases. However, if the immune system does not function properly, it may lead to either an overactive or underactive immune response, resulting in an imbalance in the immune system [1]. In this context, two common types of immune system imbalances will be discussed, including cancer and autoimmune disease.

1.1.1. Cancer

Immune system imbalance in cancer is related to the dysregulation or malfunction of the immune system that fails to recognize and eliminate cancer cells. Cancer cells have changed to an abnormal status and evaded immune surveillance by creating an immunosuppressive tumor microenvironment (TME) that allows them to thrive [2]. Several immunosuppressive factors are shown in Figure 1.

Firstly, cancer cells can express certain molecules, such as PD-1 and CTLA-4, on their cell surface. These molecules act by inhibiting the activation of T cells and hindering their ability to attack cancer cells. Secondly, the presence of chronic inflammation can contribute to the development and progression of cancer. Inflammatory processes release signaling molecules like cytokines and chemokines that can facilitate tumor growth, invasion, and metastasis. Thirdly, within the TME, certain immune cells can secrete factors such as TGF-β. These factors play a role in suppressing immune responses and supporting the survival of tumors [3]. In addition, the functionality of immune cells, particularly T cells, can be impaired due to the nutrient deficiency. This can manifest as T cell exhaustion or malfunction, which restricts their capability to recognize and combat cancer cells [4]. Also, immunosuppressive metabolites such as lactate and adenosine, along with oxidative stress produced by cancer cells, inhibit the functions of immune cells within the TME. Finally, cancer cells can decrease the expression of molecules involved in antigen presentation. Consequently, immune cells face difficulties in identifying and responding to cancer-specific antigens [5].
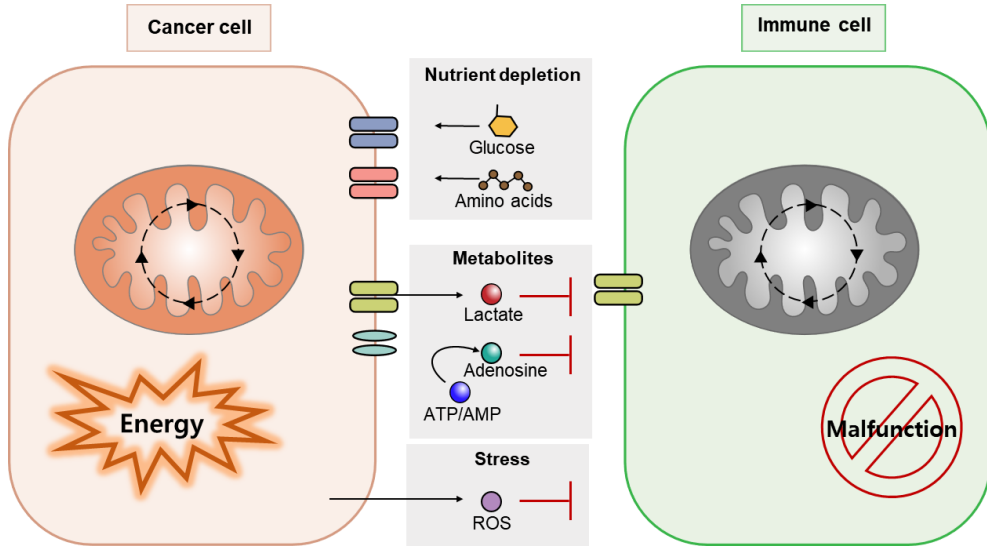
Figure 1. The immunosuppressive factors that inhibit functions of immune cells in the TME are shown.

1.1.2. Autoimmune disease

In autoimmune diseases, there is an imbalance or dysregulation of the immune system that leads to an overactive immune response against the body's own healthy cells and tissues. Instead of protecting the body, the immune system mistakenly attacks and damages various organs and systems [6].

Various mechanisms of immune imbalances contribute to development of autoimmune diseases. Firstly, autoantibodies generated by the immune system specifically target and attack the body's own cells and tissues. These autoantibodies can induce inflammation, tissue damage, and dysfunction in affected organs. Secondly, an imbalance between regulatory T cells and effector T cells can lead to an excessive activation that causes an attack on self-tissues [6]. Thirdly, genetic factors have the potential to contribute to an elevated risk of developing autoimmune diseases. These genetic variations can impact components of the immune system, such as the major histocompatibility complex (MHC) genes, which play a role in regulating immune responses and distinguishing self from non-self [7].

1.2. Current status and limitations of immunotherapy

Immunotherapy utilizes the natural defense and protection mechanism of the body, the immune system, to treat cancer and autoimmune diseases. It works by regulating the immune response to eliminate abnormal cells or modulate autoimmunity. By boosting or ameliorating the immune response under abnormal conditions, immunotherapy is currently an emerging approach in the treatment of various types of cancer and autoimmune diseases [8, 9]. However, there are still limitations that require to be

addressed.

1.2.1. Immunotherapy for cancer

To date, there are several types of immunotherapies in the treatment of cancer. The notable approaches include immune checkpoint inhibitors, CAR T-cell therapy, bispecific antibodies, cancer vaccine, and cytokine therapy [10].

Although immunotherapy has shown remarkable success in treating certain types of cancer, there are still limitations and challenges related to its application. Firstly, tumor can create an immunosuppressive microenvironment including nutrient deficient, secreted factors, and oxidative stress [4]. Secondly, tumor can have genetic alterations and significant heterogeneity, making them less susceptible to immune recognition and elimination [11]. Moreover, some tumors may have a low number of infiltrating immune cells, making it difficult to elicit a robust anti-cancer immune response [12].

1.2.2. Immunotherapy for autoimmune disease

Immunotherapy for autoimmune diseases refers to the use of medications that modulate the immune system to suppress the overactive immune response. Currently, the goal of immunotherapy for autoimmune disease is to reduce inflammation and minimize damage to healthy tissues [13].

The common options of immunotherapy used for autoimmune diseases include corticosteroids, disease-modifying anti-rheumatic drugs, biologic therapies, and immunomodulatory drugs [14]. These therapies have made significant advancements, but they still face certain limitations for autoimmune disease treatment. Current therapies mostly focus on symptom management and inflammation reduction rather than addressing the root cause of the autoimmune diseases. While these treatments can provide relief and improve quality of life, they may not offer a cure or halt disease progression [15]. Also, some immunotherapy can cause systemic immune suppression, increasing susceptibility to infections, gastrointestinal disturbances, and cause liver and lung problems [16, 17]. Moreover, the current therapeutic approaches often lack personalized strategies that consider individual patient characteristics. Individual differences in immune profiles, generics, and environmental factors can affect treatment outcomes [15].

Addressing the limitations and challenges of immunotherapy for cancer and autoimmune diseases requires ongoing research and innovation. Advancements in understating the changes in the TME and the underlying mechanisms of autoimmune diseases hold promise for overcoming these challenges, improving the efficacy of immunotherapy for cancer and autoimmune diseases.

1.3. Nanomedicine for modulating immune cells

Nanomedicine refers to the application of nanotechnology in the realm of medicine. It employs materials at the nanoscale to diagnose, treat, and prevent diseases at the molecular and cellular levels. Due to the unique advantages in targeting ability, nanomedicine has emerged as a promising approach for modulating immune cells, overcoming the limitations of current immunotherapy.

1.3.1. Nanomedicine for modulating T cells

T cells have a significant impact on the development and progression of cancer. In cancer, tumor-infiltrating lymphocytes (TILs), especially cytotoxic CD8^{+} T cells are associated with a better response for cancer immunotherapy. However, TME is a glucose-deficient condition caused by the glucose consumption of rapidly dividing cancer cells. TILs also require glucose for their activation and effector functions [4]. The limited glucose availability impairs TILs activity, leading to the inefficient outcome of immunotherapy.

Nanomaterials can be used to modulate exhausted TILs in the hypoglycemic TME. By modifying the surface of nanomaterials with T cell targeting ligands, such as CD3, metabolic regulating agents can be selectively delivered to TILs. This enables TILs to utilize alternative nutrients as their energy source, overcoming the nutrient deprivation present within the TME (Figure 2).
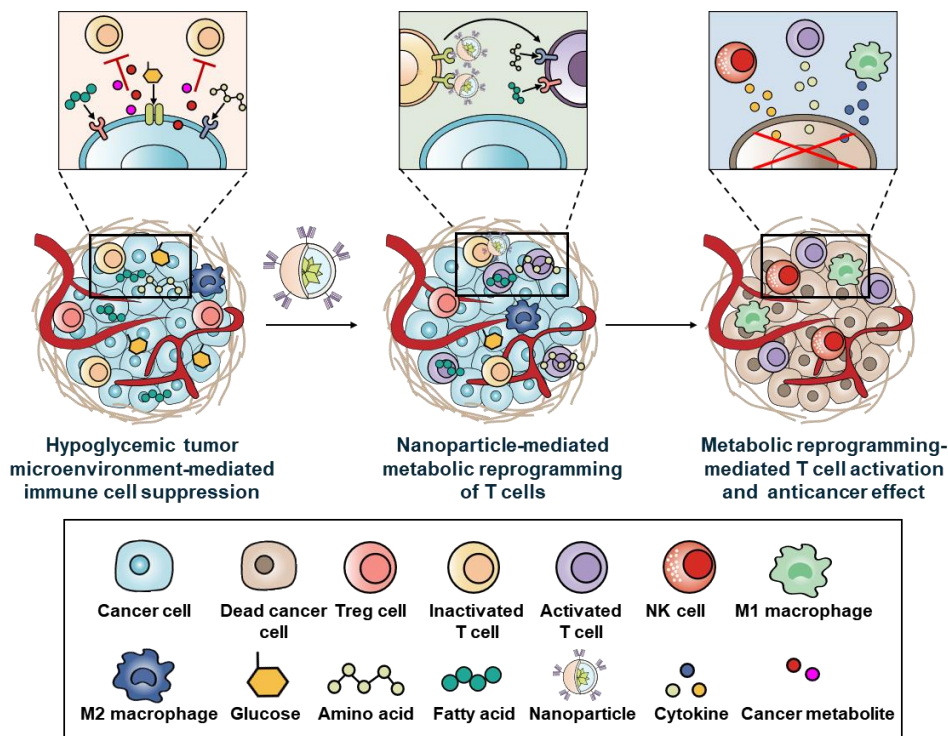
Figure 2. Strategy to enhance anticancer effect of TILs in the hypoglycemic

TME by nanomedicine is illustrated.

1.3.2. Nanomedicine for modulating antigen-presenting cells

Antigen-presenting cells (APCs) play a vital role in initiating and regulating immune responses by presenting antigens to T cells, thereby eliciting specific immune responses [18]. Therefore, modulating APCs is a promising approach in immunotherapeutic strategies (Figure 3).

Nanomaterials can be designed to carry both antigens and adjuvants, substances that regulate immune responses. By co-delivering these components, nanomaterials promote efficient antigen uptake by APCs and provide immune-stimulating signals, leading to enhanced antigen presentation and T cell activation. Moreover, nanomaterials can also be used to modulate the regulatory functions of APCs, such as promoting immune tolerance or dampening excessive immune responses. They can carry both antigens and immunomodulatory drugs that selectively target regulatory pathways in APCs, influencing their ability to modulate immune responses [19].
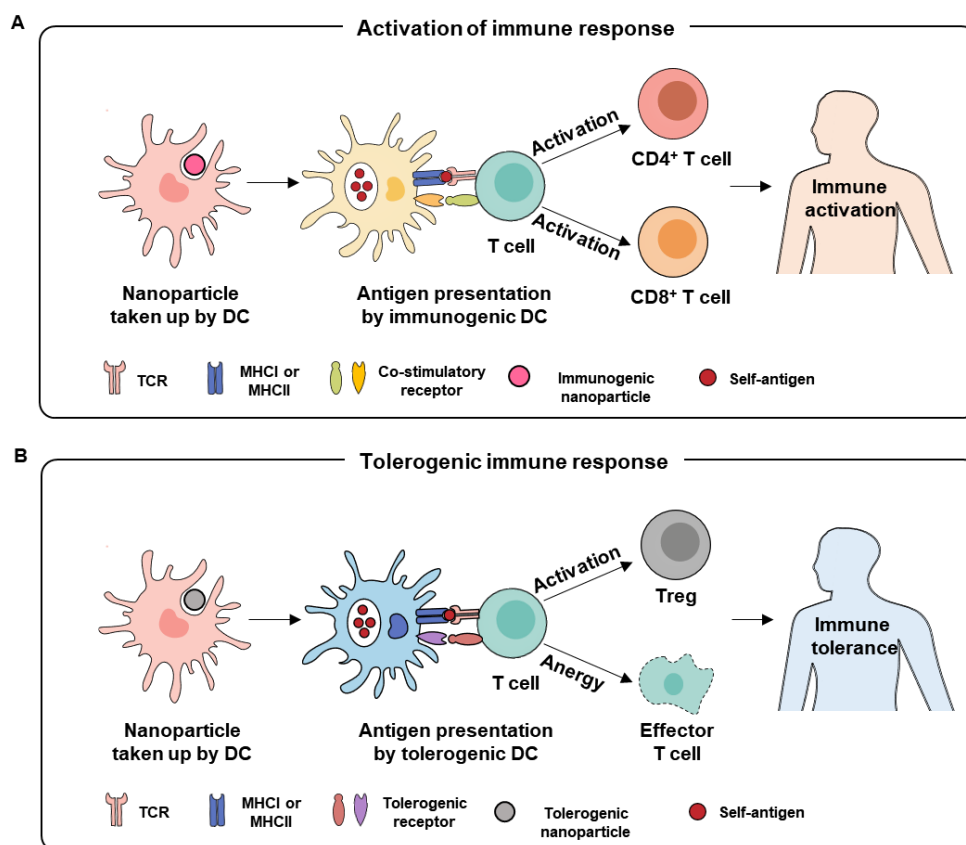
Figure 3. Nanomedicine-mediated DC modulation for immunotherapy. A) Activation of immune response can be achieved by delivering immunogenic nanoparticles. Induction of immunogenic DC differentiation can promote CD4$^+$ and CD8$^+$ T cell differentiation, enhancing immune activation. B)

Tolerogenic immune response can be achieved by delivering tolerogenic nanoparticles. Antigen-presentation by tolerogenic DC can facilitate regulatory T cells (Tregs) differentiation and disarm effector T cells, inducing immune tolerance against self-antigens.

1.3.3. Advantage of nanomedicine for immune cell modulation

The important aspect in which antibody-conjugated nanomedicines are suitable for modulating immune cells is that they lack in vivo antibody-dependent cytotoxicity (ADCC) or complement-dependent cytotoxicity (CDC) towards immune cells. In order to specifically target immune cells, targeting ligands such as antibodies are required. The antibody-drug conjugate (ADC) is a targeted therapy composed of monoclonal antibodies and potent drugs that are used for specifically targeting cells. Currently, FDA-approved ADCs are used to target and kill cancer cells by specifically targeting them and delivering potent cytotoxic drugs. In addition to the direct cancer-killing effect due to the cytotoxic drugs, the ADCC and CDC, caused by the interaction between the Fc segment and Fc receptors on the surface of effector cells (NK cells, neutrophils, macrophages, etc.), or protein C1q, can facilitate the anticancer effect of ADCs. These mechanisms are effective for cancer-killing effects; however, they are not suitable for immune cell modulation. It has been reported that antibody-conjugated nanomedicines lack ADCC or CDC [20]. The binding orientation of the antibody with Fc receptor is important for the potency of ADCC [21]. The antibody conjugated on the surface of nanomedicines may not have the proper binding orientation with the Fc receptor, thus limiting the initiation of ADCC. Additionally, the structure of nanomedicines may hinder the Fc segment, preventing the interaction between the Fc segment and the Fc receptor. In this aspect, nanomedicines provide benefits compared to ADCs for modulating immune cells to overcome the limitations of current immunotherapy.

1.4. Scope of study

While immunotherapy has shown promise in the treatment of cancer and autoimmune diseases, there are situations in which it may fail or not provide the desired outcomes. In this research, various nano-delivery systems were developed to enhance the outcomes and address the limitations of immunotherapy in cancer and autoimmune diseases.

In Chapter 2, activation of the anticancer effector functions of T cells through nanoparticle-induced lipid metabolic reprogramming was reported. To this end, fenofibrate was encapsulated in amphiphilic poly (γ-glutamic acid)-based nanoparticles (F/ANs), and the surfaces of F/ANs were modified with an anti-CD3e f(ab')2 fragment, yielding aCD3/F/ANs. Activation of fatty acid metabolism by aCD3/F/ANs supported the proliferation of T cells in a glucose-deficient environment mimicking the TME. In vivo administration of aCD3/F/ANs increased infiltration of T cells

into tumor tissues. The treatment of tumor-bearing mice with aCD3/F/ANs enhanced production of various cytokines in tumor tissues and prevented tumor growth. Based on these findings, it is suggested that nanomedicine-enabled reprogramming of lipid metabolism in T cells holds potential as a novel approach in immunometabolic therapy. This approach aims to address the current challenges of immunotherapy caused by the nutrient-deficient TME

In Chapter 3, a mannose-modified cationic lipid nanoparticle (M-NP) was developed to deliver the nucleic acid adjuvant, polyinosinic:polycytidylic acid (PIC), to antigen-presenting cells (APCs). PIC-loaded M-NP (PIC/M-NP) showed stable lipoplexes regardless of the ligand ratio and negligible cytotoxicity in bone marrow-derived dendritic cell (BMDC). DC uptake of PIC/M-NP was demonstrated, and an increased mannose ligand ratio improved DC uptake efficiency. PIC/M-NP significantly promoted the maturation of BMDC, and local injection of PIC/M-NP to mice facilitated lymphatic delivery and activation (upon NP uptake) of DC. These results support the potential of PIC/M-NP in delivering adjuvants as a promising vaccine delivery system for immunotherapy.

In Chapter 4, a tannic acid-based nanomaterial was designed to treat rheumatoid arthritis by inducing antigen-specific immune tolerance. The tolerogenic nanovaccine was designed for targeted delivery of dexamethasone and citrullinated peptide in a lipid-coated nanoparticle consisting of tannic acid as core nanomaterial (CitDTN). The surface of CitDTN was modified with abatacept to yield AbaCitDTN. AbaCitDTN reprogrammed the properties of dendritic cells toward tolerogenic phenotypes and interrupted co-stimulatory signals between DC and T cells, leading to suppressed T cell proliferation and IL-2 secretion. Collagen-induced arthritis DBA/1 model mice were subcutaneously administered with AbaCitDTN weekly for a total of four injections. This reduced inflammation in the synovial space and decreased autoimmunity against type II collagen and citrullinated peptide. In vivo administration of AbaCitDTN improved clinical symptoms and protected joints from destruction in this animal model. These findings suggest that tannic acid-based nanomaterials have the potential to induce antigen-specific immune tolerance for the treatment of rheumatoid arthritis. Importantly, it can be achieved without causing significant systemic inflammation, which is commonly associated with current immunotherapy approaches for autoimmune diseases.

1.5. Reference

[1]   G. Eberl. Immunity by equilibrium. *Nat. Rev. Immunol.* **2016**, *16*, 524-32.

[2]   K. J. Hiam-Galvez, B. M. Allen, M. H. Spitzer. Systemic immunity in cancer. *Nat. Rev. Cancer* **2021**, *21*, 345-359.

[3] A. Labani-Motlagh, M. Ashja-Mahdavi, A. Loskog. The Tumor Microenvironment: A Milieu Hindering and Obstructing Antitumor Immune Responses. *Front Immunol*. **2020**, *11*, 940.

[4] Y. Zhang, R. Kurupati, L. Liu, X. Y. Zhou, G. Zhang, A. Hudaihed, F. Filisio, W. Giles-Davis, X. Xu, G. C. Karakousis, L. M. Schuchter, W. Xu, R. Amaravadi, M. Xiao, N. Sadek, C. Krepler, M. Herlyn, G. J. Freeman, J. D. Rabinowitz, H. C. J. Ertl. Enhancing CD8+ T Cell Fatty Acid Catabolism within a Metabolically Challenging Tumor Microenvironment Increases the Efficacy of Melanoma Immunotherapy. *Cancer Cell* **2017,** *32*, 377-391.

[5] K. Dhatchinamoorthy, J. D. Colbert, K. L. Rock. Cancer Immune Evasion Through Loss of MHC Class I Antigen Presentation. *Front Immunol*. **2021**, *12*, 636568.

[6] L. Wang, F.-S. Wang, M. E. Gershwin. Human autoimmune diseases: a comprehensive update. *J. Intern. Med*. **2015**, *278*, 369-95.

[7] V. Matzaraki, V. Kumar, C. Wijmenga, A. Zhernakova. The MHC locus and genetic susceptibility to autoimmune and infectious diseases. *Genome Biol*. **2017**, 18, 76.

[8] S. Tan, D. Li, X. Zhu. Cancer immunotherapy: Pros, cons and beyond. *Biomed. Pharmacother*. **2020**, *124*, 109821.

[9] S. M. Jung, W.-U. Kim. Targeted Immunotherapy for Autoimmune Disease. *Immune Netw*. **2022**, *22*, e9.

[10] S. L. Gupta, S. Basu, V. Soni, R. K. Jaiswal. S. L. Gupta, S. Basu, V. Soni, R. K. Jaiswal. *Mol. Biol. Rep*. **2022**, *49*, 9903-9913.

[11] N. El-Sayes, A. Vito, K. Mossman. Tumor Heterogeneity: A Great Barrier in the Age of Cancer Immunotherapy. *Cancers (Basel)*. **2021**, *13*, 806.

[12] C. Jochems, J. Schlom. Tumor-infiltrating immune cells and prognosis: the potential link between conventional cancer therapy and immunity. *Exp. Biol. Med. (Maywood)*. **2011**, *6*, 67-79.

[13] R. R. Caspi. Immunotherapy of autoimmunity and cancer: the penalty for success. *Nat. Rev. Immunol*. **2008**, *8*, 970-6.

[14] P. Li, Y. Zheng, X. Chen. Drugs for Autoimmune Inflammatory Diseases: From Small Molecule Compounds to Anti-TNF Biologics. *Front Pharmacol*. **2017**, *8*, 460.

[15] J. S. Smolen, D. Aletaha, A. Barton, G. R. Burmester, P. Emery, G. S. Firestein, A. Kavanaugh, I. B. McInnes, D. H. Solomon, V. Strand, K. Yamamoto. Rheumatoid arthritis. *Nat. Rev. Dis. Primers* **2018**, *4*, 18001.

[16] S. Bindu, S. Mazumder, U. Bandyopadhyay. Non-steroidal anti-inflammatory drugs (NSAIDs) and organ damage: A current perspective. *Biochem. Pharmacol*. **2020**, *180*, 114147.

[17] Q. Guo, Y. Wang, D. Xu, J. Nossent, N. J Pavlos, J. Xu. Rheumatoid arthritis: pathological mechanisms and modern pharmacologic therapies. *Bone Res*. **2018**, *6*, 15.

[18] S. J. Gaudino, P. Kumar. Cross-Talk Between Antigen Presenting Cells and T Cells Impacts Intestinal Homeostasis, Bacterial Infections, and Tumorigenesis. *Front Immunol*. **2019**, *10*, 360.

[19] J. Park, Y. Wu, Q. Li, J. Choi, H. Ju, Y. Cai, J. Lee, Y.-K. Oh. Nanomaterials for antigen-specific immune tolerance therapy. *Drug Deliv. Transl, Res*. **2022**.

[20] M. Ahmed, D. W. Pan, M. E. Davis. Lack of in Vivo Antibody Dependent Cellular Cytotoxicity with Antibody Containing Gold Nanoparticles. *Bioconjug. Chem*. **2015**, *26*, 812-6.

[21] W. D. Tolbert, R. Sherburn, N. Gohain, S. Ding, R. Flinko, C. Orlandi, Krishanu Ray, A.inzi, G. K. Lewis, M. Pazgier. Defining rules governing recognition and Fc-mediated effector functions to the HIV-1 co-receptor binding site. *BMC Biol*. **2020**, *18*, 91.

Chapter 2

Nanoparticle-mediated lipid metabolic reprogramming of T cells in tumor microenvironments for immunometabolic therapy

Chapter 2. Nanoparticle-mediated lipid metabolic reprogramming of T cells in tumor microenvironments for immunometabolic therapy

2.1. Introduction

Anticancer chemicals and biologic necrosis factors have been delivered to tumors using various nanoparticles [1-4]. To date, the most studied anticancer nanomedicines for delivery of anticancer agents are those containing tumor-targeting ligands. Despite progress in nano-enabled targeted delivery of anticancer therapeutics to tumor tissues, clinical translation of these nanomedicines remains limited. One reason for the limited clinical translation of ligand-modified nanomedicines is the heterogeneity of tumors. The responsiveness of tumor cells to anticancer drugs can differ depending on tumor type. Moreover, the delivery of anticancer drugs to nonresponsive tumor cells can exert variable effects depending on the physiological properties of the cells [5,6]. Even in drug-responsive tumor types, differing densities of target receptors on tumor cells can variably affect the extent of delivery of therapeutics to cancer cells [7]. Folate receptors and transferrin receptors have long been studied for targeted delivery of anticancer drugs to tumor cells. However, the density of these receptors on tumor cells varies such that delivery of nanoparticle anticancer drugs to tumor cells with a lower density of target receptors may be insufficient [8].

An emerging approach for circumventing this tumor cell heterogeneity focuses on leveraging tumor-adjacent immune cells in the tumor microenvironment [9, 10]. Compared with tumor cells, adjacent cells in the tumor microenvironments are reported to be less heterogeneous [11]. Reported targets in the microenvironment of various tumors include fibroblast activation protein, expressed on cancer-associated fibroblasts [12]; CD11c, expressed on dendritic cells [13]; and CD3, a biomarker of T cells whose expression on T cells is reported to be preserved in various tumors [14]. Exploiting this reduced heterogeneity of tumor-adjacent cells, the activation of cancer-associated fibroblasts was reported to enhance the delivery of doxorubicin in graphene-based nanosheets [15]. It has been reported that dendritic cells in the tumor microenvironment can be activated by immune adjuvant-loaded polydopamine nanoparticles [16] and other nanoparticles, such as biopolymeric nanoparticles [17]. A number of studies addressing modulation of the tumor microenvironment have reported enhanced infiltration of T cells. However, the recruited T cells have been reported to lose their activity in the hypoglycemic tumor microenvironment [18]. Thus, there exists an unmet need for a therapeutic strategy for activating effector functions of T cells in the tumor microenvironment.

The importance of manipulating metabolic imbalances in immune cells in anticancer immunotherapy has become increasingly apparent [19]. Effector cytotoxic T cells have been reported to lose their activity because of the metabolically stressful conditions of the tumor microenvironment [20].

Glucose is known to be deficient in the tumor microenvironment, and the cytotoxic activity of T cells is impaired by a lack of energy. Thus, metabolic reprogramming of immune cells in the tumor microenvironment to allow utilization of different energy substrates would be a viable strategy for improving immunotherapy.

In this study, the hypothesis that metabolic reprogramming of T cells was tested using a nanotechnology approach could activate T cells to fight against tumor cells (Figure 1). To this end, T cell-targeting nanoparticles were designed to encapsulate the lipid metabolism-activating drug molecule, fenofibrate, which is known to induce the expression of peroxisome proliferator-activated receptor (PPAR)-α and downstream fatty acid metabolism-related genes. In was previously reported that promoting fatty acid metabolism by orally administered PPAR-α agonist can relieve metabolic stress from hypoglycemic condition in tumor microenvironment and preserve effector function of T cells, thereby enhancing anti PD-1 immunotherapy [21]. For T cell-targeted delivery, fenofibrate was entrapped in amphiphilic poly (γ-glutamic acid)-based nanoparticles (F/ANs), and further modified the nanoparticle surface with an anti-CD3e f(ab′)2 fragment, yielding aCD3/F/ANs. Here, aCD3/F/ANs showed the ability to activate fatty acid metabolism, mitochondrial functions, and stimulate the anticancer activity of T cells in tumor microenvironments.
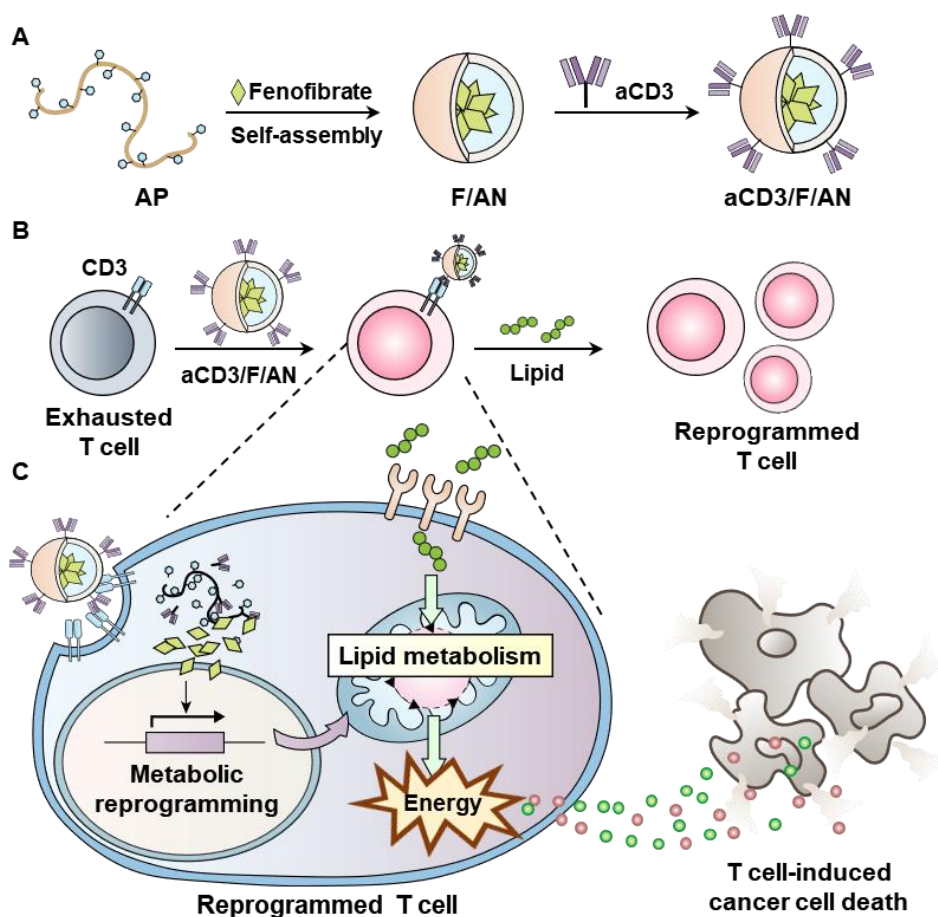
Figure 1. Metabolic reprogramming of T cells by aCD3/F/ANs. A) Schematic illustration of the aCD3/F/AN preparation process. B) Mechanism by which aCD3/F/ANs increase mitochondrial fatty acid metabolism in T cells. C) Proposed effect of fatty acid metabolism reprogramming on T cell-mediated killing of cancer cells.

2.2. Material and Method
2.2.1. Synthesis of amphiphilic poly (γ-glutamic acid)

Amphiphilic poly (γ-glutamic acid) (AP) was synthesized by grafting phenylalanine ethyl ester with poly (γ-glutamic acid) (γ-PGA) through a carbodiimide crosslinking reaction, as described previously [22]. Briefly, 5.94 μmol of γ-PGA (50 kDa; BioLeaders, Daejeon, Republic of Korea) was dissolved in 30 ml of 0.3 M NaHCO₃ solution followed by addition of 2.84 mmol of 1-(3-dimethylaminopropyl)-3-ethylcarbodiimide hydrochloride (EDC; Tokyo Chemical Industry Co., Ltd., Tokyo, Japan) with stirring on ice for 30 min. Next, 2.30 mmol of L-phenylalanine ethyl ester hydrochloride (Sigma-Aldrich, St. Louis, MO, USA) was added and the solution was stirred for an additional 24 h at 37 °C. For imaging and confocal microscopy, fluorescent dye-labeled AP (fAP) was synthesized by adding 3.2 μmol of fluoresceinyl glycine amide (5-(aminoacetamido)

fluorescein) (Thermo-Fisher Scientific, Waltham, MA, USA) to a solution containing 2 µmol of γ-PGA, 0.96 mmol of EDC and 0.77 mmol of L-phenylalanine ethyl ester hydrochloride and allowing the reaction to proceed for 24 h. The resulting AP and fAP were purified by dialyzing first in triple distilled water for 48 h and then in methanol for 48 h using a Spectra/Pore dialysis membrane (MWCO, 3 kDa; Spectrum Labs, Rancho Dominguez, CA, USA), after which they were lyophilized and stored at 4 °C until use. The synthesis of AP was confirmed by ^{1}H NMR spectroscopy.

2.2.2. Preparation of fenofibrate-loaded and anti-CD3 antibody-modified nanoparticles

Fenofibrate was encapsulated in AP-based nanoparticles (ANs) and fAP using a thin film hydration method. In brief, 0.55 µmol of fenofibrate (Sigma-Aldrich) in 1 ml methanol was added into 1 ml of 0.1 mM AP in methanol solution. After solvent removal using a rotary evaporator (CCA-1110; Tokyo Rikakikai, Tokyo, Japan), the resulting film was hydrated with 1 ml of phosphate-buffered saline (PBS; pH 7.4) and sonicated for 10 min. The resulting fenofibrate-loaded ANs (F/ANs or F/fANs) were purified from unencapsulated fenofibrate by centrifugation at 12,000 × g for 3 min. For modification with anti-CD3 antibody, F/ANs (3.5 mg) were first mixed with 6.4 µmole of EDC, then reacted on ice for 5 min and allowed to stand at room temperature (RT) for an additional 5 min. A solution of anti-mouse CD3e f(ab′)2 antibody (Bio X Cell, West Lebanon, NH, USA, catalog #BE0001-1FAB, lot #659618A1) was added to the EDC-activated F/AN suspension at a 1:50 molar ratio of antibody to AP and stirred at RT for 6 h. Free antibody was removed by dialysis (MWCO, 300 kDa; Spectrum Labs), and after quantifying the amount of antibody on the nanoparticle surface by BCA assay (Thermo-Fisher Scientific), anti-mouse CD3e f(ab′)2 antibody-conjugated F/ANs (aCD3/F/ANs) or anti-mouse CD3e f(ab′)2 antibody-conjugated F/fANs (aCD3/F/fANs) were concentrated from reactants using an Amicon filter (Merck, Kenilworth, NJ, USA). In some experiments, anti-mouse CD3e f(ab′)2 antibody was conjugated to plain ANs (aCD3/ANs) or to fANs (aCD3/fANs). Physical mixture of equivalent amount of anti-mouse CD3e f(ab′)2 antibody with F/ANs (aCD3+F/ANs) or with F/fANs (aCD3+F/fANs) were used as control groups.

2.2.3. Quantification of encapsulated fenofibrate

The amount of fenofibrate encapsulated in ANs was analyzed by high-performance liquid chromatography (HPLC) using a Hewlett Packard model 1100 system (Hewlett Packard, Palo Alto, CA, USA) equipped with a reverse-phase C18 HPLC column (Nucleosil 100-5 C18; Macherey-Nagel, Düren, Germany). Lyophilized nanoparticles were dissolved in 200 µl of MeOH and injected into the C18 column. The column (temperature, 40 °C) was eluted using a mobile phase consisting of acetonitrile:water (pH of water adjusted to 4 with acetic acid) (90:10, v/v) at a flow rate of 1 mL/min.

The peak of fenofibrate was monitored by measuring absorbance at 287 nm using at UV detector. Fenofibrate concentration was determined by reference to a standard curve prepared using a series of fenofibrate solutions in methanol.

2.2.4. Characterization and stability studies

Nanoparticles were characterized by size, surface charge, morphology, and elemental composition. The size distribution and zeta potential of nanoparticles were measured by dynamic light scattering (DLS) using an ELSZ-1000 instrument (Otsuka Electronics Co., Osaka, Japan). The morphology of nanoparticles was visualized by transmission electron microscopy (TEM) using a JEM1010 transmission electron microscope (JEOL, Tokyo, Japan). The presence of elemental oxygen, chlorine and sulfur in nanoparticles was determined by energy-dispersive X-ray spectroscopy (EDS-STEM) using a JEM-2100 F transmission electron microscope (JEOL). The stability of nanoparticles was monitored for up to 7 d. F/ANs and aCD3/F/ANs were stored in PBS at 4 °C. The sizes of particles were measured daily by DLS using an ELSZ-1000 instrument (Otsuka Electronics Co.).

2.2.5. In vitro study of pH-dependent release

The pH dependence of fenofibrate release from ANs was tested using a dialysis approach. Fenofibrate released from ANs was quantified by immersing a dialysis bag (MWCO, 3.5 kDa; Spectrum Labs) containing aCD3/F/ANs in 15 mL PBS containing 0.1% (w/v) Tween-80 (Sigma-Aldrich) at different pH values. At each time point, 1 mL of dialysis buffer was collected and the volume of dialysis was maintained by adding fresh buffer. Collected samples were lyophilized and dissolved in 200 μL methanol, and the amount of fenofibrate release was analyzed by HPLC.

2.2.6. Animals

Five-week-old C57BL/6 mice were purchased from Raon Bio and maintained under standard pathogen-free conditions at the Animal Center for Pharmaceutical Research, Seoul National University. All animal experiments were performed according to the Guidelines for the Care and Use of Laboratory Animals of the Institute of Laboratory Animal Resources, Seoul National University (approval number, SNU-190417-15(E)).

2.2.7. Evaluation of CD3 expression

The expression levels of CD3 were determined at various cells including murine lung fibroblast cell line MLg (Korean Cell Line Bank, Seoul, Republic of Korea), human lung fibroblast cell line MRC-5 (Korean Cell Line Bank), human embryonic kidney cell line 293T (ATCC, Manassas, VA, USA), murine bone marrow-derived macrophages (BMDM), murine bone marrow-derived dendritic cells (BMDC), and T cells. BMDM and BMDC

were differentiated from monocytes as previously described [16, 23]. T cells were isolated from spleens of C57BL/6 mice using nylon wool columns [24]. MLg, MRC-5, 293T, BMDM and BMDC, and T cells were stained with FITC-conjugated anti-mouse CD3 antibody (BioLegend, San Diego, CA, USA; catalog #100203, lot #B263028) for 1 h. The expression of CD3 was evaluated by flow cytometry.

2.2.8. In vitro study of nanoparticle uptake

In vitro cellular uptake of nanoparticles was evaluated using flow cytometry and fluorescence microscopy. For flow cytometry, MLg, MRC-5, 293T, BMDM, BMDC and T cells were seeded onto 24-well plates (SPL Life Sciences) at 1×10^6 cells/well, and treated with 2 mg/mL of fluorescein isothiocyanate (FITC)-labeled various nanoparticles for 4 h. Cells were harvested, washed with PBS, and analyzed by flow cytometry. For fluorescence microscopy, T cells were seeded onto 24-well plates (1×10^6 cells/well) and treated with 2 mg/mL FITC-labeled nanoparticles for 4 h. After washing and resuspending cells in 100 μL PBS, cell suspensions were plated onto poly-L-lysine coverslips (Corning, New York, NY, USA) and allowed to completely attach (30 min). Cells were then fixed with 4% formaldehyde in PBS for 10 min, washed with PBS, and stained with DAPI (4',6-diamidino-2-phenylindole, Sigma-Aldrich). The fluorescence of cells was observed using a confocal laser-scanning microscope (LSM 5 Exciter; Carl Zeiss, Inc., Jena, Germany).

2.2.9. In vitro cell viability study

In vitro viability of cells was measured after treatment of nanoparticles. After treatment with various nanoparticles, T cells were suspended in 100 μL RPMI medium containing 10% WST-1 reagent. After incubating for 2 h at 37 °C, absorbance of the medium at 430 nm was measured using a Multi-Reader (Molecular Devices, San Jose, CA, USA). The other adherent cells including MLg, MRC-5, 293T, BMDM and BMDC were incubated with culture medium containing 10% MTT reagent. After incubating for 2 h at 37 °C, absorbance of medium at 570 nm was detected using a Multi-Reader (Molecular Devices).

2.2.10. In vitro study of PPARα, CD36 and fatty acid oxidation-associated gene expression

Expression levels of PPARα, CD36 and fatty acid oxidation-associated genes in T cells following treatment with nanoparticles were measured by reverse transcription-polymerase chain reaction (RT-PCR), flow cytometry and western blot. The fatty acid oxidation-associated genes and gene products measured included carnitine palmitoyltransferase 1B (CPT1B), acyl-CoA dehydrogenase medium chain (MCAD) and acyl-CoA dehydrogenase long chain (LCAD) [21, 25]. Isolated mouse T cells were

seeded onto 24-well plates (1×10^6 cells/well) and treated with various nanoparticle preparations containing 20 μM fenofibrate for 24 h. For RT-PCR, total RNA was isolated from T cells using the TRIzol reagent (Invitrogen, Carlsbad, CA, USA). cDNA was synthesized from mRNA using an AccuPower RT PreMix (Bioneer, Daejeon, Republic of Korea). Quantitative real-time RT-PCR was performed using a LightCycler FastStart DNA Master SYBR Green I system (Roche, Basel, Switzerland). Primer sequences used in RT-PCR are listed in Table 1. For western blot, T cells were lysed with a commercial radioimmunoprecipitation assay lysis buffer (Rockland, Limerick, PA, USA) containing a cocktail of protease inhibitors (cOmplete™, Mini, EDTA-free Protease Inhibitor Cocktail, Sigma-Aldrich (Roche). The amounts of protein were quantified by BCA assay and boiled at 95 ºC 10 min. As primary antibodies, anti-mouse CPT1B (Proteintech, Rosemont, IL, USA; catalog #22170-1-AP, lot #00048665), anti-mouse LCAD (Proteintech, catalog #17526-1-AP, lot #00051417), anti-mouse MCAD (Proteintech, catalog #55210-1-AP, lot #09000327) and anti-mouse β-actin (Cell signaling, Denver, MA, USA; catalog #8457, lot #6) were used. Horseradish peroxidase-linked anti-rabbit IgG (Cell signaling, catalog #7074, lot #28) was used as secondary antibody. Amersham ECL Prime Western Blotting detection reagent (GE Healthcare, Chicago, IL, USA) was used for signal detection.

Expression levels of PPARα protein were assessed by flow cytometry. Briefly, T cells were seeded onto 24-well plates (1×10^6 cells/well) and treated with various nanoparticle preparations containing 20 μM fenofibrate for 48 h. Cells were harvested, washed with PBS, and stained with FITC-conjugated anti-mouse CD3 antibody (BioLegend) for 1 h. Cells were fixed and permeabilized using a transcription factor buffer set (BioLegend; catalog #424401) and incubated with Alexa Fluor 647-conjugated anti-mouse PPARα antibody (Santa Cruz Biotechnology, Santa Cruz, CA, USA; catalog #sc-398394, lot #H1017) for 1 h.

Protein expression levels of the fatty acid translocase, CD36, were analyzed by flow cytometry. Briefly, T cells seeded onto a 24-well plate (1×10^6 cells/well) were treated with various nanoparticle preparations containing 20 μM fenofibrate for 48 h and then stained with FITC-conjugated anti-mouse CD3 antibody and allophycocyanin (APC)-conjugated anti-mouse CD36 antibody (BioLegend; catalog #102611, lot #B270594) for 1 h.

2.2.11. Assessment of mitochondrial activation

Mitochondrial activation was evaluated based on morphology, membrane potential and oxygen consumption rate (OCR). T cells were seeded onto a 24-well plate (1×10^6 cells/well) and stimulated with anti-CD3/CD28 antibody-tethered Dynabeads (Thermo-Fisher Scientific) at a 1:1 ratio of T cells to beads in the presence of interleukin (IL)-2 (10 ng/mL) for 48 h.

After removal of beads, T cells were treated with various nanoparticle preparations containing 20 μM fenofibrate in the presence of IL-2 (10 ng/mL) for 48 h. Cells were then starved by incubating for 24 h in low-glucose medium (XF DMEM Base Medium) containing 0.5 mM XF glucose, 1 mM XF glutamine, 0.5 mM carnitine (Sigma-Aldrich), 1% fetal bovine serum (FBS) and 40 μM palmitate-bovine serum albumin (BSA; Seahorse Biosciences, Billerica, MA, USA). For TEM observation of mitochondrial morphology, T cells were fixed with Karnovsky's solution and pelleted, after which cell pellets were fixed with 1% osmium tetroxide for 1 h and stained with 0.5% uranyl acetate overnight. Cell pellets were dehydrated with ethanol and sequentially immersed in ethanol/Spurr's resin (1:1) solution and ethanol/Spurr's (1:2) solution for 1 h each [26]. Cells were then incubated with Spurr's resin again at 4 °C overnight, followed by incubation at 70 °C overnight. Thin sections (60 nm) were prepared and observed by TEM (Talos L120C; Thermo Fisher Scientific, Inc.).

Mitochondrial membrane potential was measured by flow cytometry and confocal microscopy. For flow cytometry, cells were incubated with 0.125 μM MitoTracker Orange CMTMRos (Life Technologies) for 30 min and analyzed by flow cytometry. For confocal microscopy, cells were seeded onto poly-L-lysine coverslips after staining with MitoTracker. Nuclei were counterstained with DAPI and fixed with 4% formaldehyde. The fluorescence of T cells was observed by confocal laser-scanning microscopy (TCS8; Leica Microsystems GmbH, Wetzlar, Germany).

OCR and extracellular acidification rate (ECAR) were measured with an XFp Extracellular Flux analyzer (Seahorse Biosciences) using an XFp Cell Mito Stress Test Kit (Seahorse Biosciences) and XFp Glycolysis Stress Kit (Seahorse Biosciences), according to the manufacturer's instructions. For OCR measurements, T cells were seeded onto a Cell-Tak (Seahorse Biosciences) pre-coated XFp culture microplate (4×10^5 cells/well). Immediately prior to OCR measurements, 100 μM of palmitate-BSA was added to the plate. During measurements, 2 μM oligomycin, 1.5 μM carbonyl cyanide-4 (trifluoromethoxy)phenylhydrazone and 1 μM rotenone and antimycin A mixture were added to each well. For ECAR measurements, T cells were seeded onto a Cell-Tak pre-coated XFp microplate (4×10^5 cells/well). During the measurement, 10 mM glucose, 1 μM oligomycin and 100 mM 2-deoxy-D-glucose were added to each well.

2.2.12. In vitro T cell proliferation test

The effect of nanoparticles on T cell proliferation was studied using cell apoptosis, cell proliferation, and live/dead cell assays. Mouse T cells were seeded onto a 24-well plate (1×10^6 cells/well) and activated by adding anti-CD3/CD28 Dynabeads at a T cell:Dynabeads ratio of 1:1 in the presence of IL-2 (10 ng/mL) for 48 h. After removing Dynabeads, T cells were treated with various nanoparticle preparations containing 20 μM fenofibrate for 48 h in the presence of IL-2 (10 ng/mL). The medium was then changed to

low-glucose medium supplemented with 40 µM palmitate-BSA and incubated for an additional 24 h.

Apoptosis of T cells was measured using an Annexin V Apoptosis Detection Kit FITC (Thermo-Fisher Scientific). Apoptotic cells were detected by staining cells with annexin V and propidium iodide (PI). Cell viability was measured using WST-1 reagent (Sigma-Aldrich). In brief, T cells were suspended in 100 µL RPMI medium containing 10% WST-1 reagent and then seeded onto a 96-well plate. After incubating for 2 h at 37 °C, absorbance of the medium at 430 nm was measured using a Multi-Reader (Molecular Devices). For live/dead assays, T cells were harvested and stained with 2 µM calcein AM and 4 µM PI for 15 min. Cell viability was assessed by examining under a fluorescence microscope (DM IL; Leica).

2.2.13. In vitro measurement of lipid uptake by T cells

Lipid uptake by T cells was measured by flow cytometry using fluorescently labeled lipids. T cells were seeded onto a 24-well plate $(1 \times 10^6$ cells/well) and stimulated with anti-CD3/CD28 antibody-tethered Dynabeads at a T cell to bead ratio of 1:1 in the presence of IL-2 (10 ng/mL) for 48 h. Dynabeads were then removed and T cells were further treated with various nanoparticle preparations containing 20 µM fenofibrate in the presence of IL-2 (10 ng/mL) for 48 h. The medium was then replaced with fresh RPMI-1640 medium, and T cells were treated with 1 µM BODIPY C_{16} (Thermo-Fisher Scientific), a fluorescent fatty acid, at 37 °C for an additional 2 h. T cells were harvested and washed with PBS, and lipid uptake was analyzed by flow cytometry.

2.2.14. In vitro measurement of T cell secretion of fatty acid metabolites

Secretion of fatty acid metabolites from T cells was evaluated by assaying β-hydroxybutyrate in culture medium. Briefly, isolated T cells were seeded in a 24-well plate $(1 \times 10^6$ cells/well) and activated with anti-CD3/CD28 antibody-tethered Dynabeads at a T cell to bead ratio of 1:1 in the presence of IL-2 (10 ng/mL) for 48 h. Dynabeads were removed and T cells were treated with nanoparticle preparations containing 20 µM fenofibrate. After incubation with nanoparticles for an additional 48 h, cells were washed with PBS and resuspended in low-glucose medium with 40 µM palmitate-BSA. After starvation for 24 h, β-hydroxybutyrate concentration in the culture medium was measured using a β-Hydroxybutyrate Assay Kit (Abcam, Cambridge, England).

2.2.15. In vitro assessment of the cancer cell-killing activity of nanoparticle-stimulated T cells

The ability of nanoparticle-treated T cells to kill B16F10 melanoma cells was measured by fluorescence dye staining and live, real-time video monitoring. T cells from splenocytes were exposed to tumor-associated

antigens and treated with various nanoparticle preparations. To better mimic the in vivo tumor microenvironment, splenocytes were isolated from spleens of adjuvant-treated B16F10 tumor-bearing mice. In brief, C57BL/6 mice were inoculated subcutaneously with B16F10 cells (5×10^5 cells). Seven days after tumor inoculation, doxorubicin (DOX; Sigma-Aldrich), used as an immunogenic cell death inducer [27], was injected intratumorally at a dose of 50 µg/mouse together with monophosphoryl lipid A (MPL; InvivoGen, San Diego, CA, USA), used as an adjuvant [28], at a dose of 20 µg/mouse [29]. After 2 d, mice were sacrificed and splenocytes were isolated from the spleen and antigenically stimulated with B16F10 lysates, prepared by repeatedly freezing and thawing (5 cycles) B16F10 cells (2×10^5 cells/mL). Splenocytes were incubated with the resulting tumor lysates for 48 h, after which collected T cells were treated with various nanoparticle preparations with or without 20 µM fenofibrate for 48 h, and then further treated with low-glucose medium containing 40 µM palmitate-BSA for 24 h.

The cancer cell-killing activity of T cells was evaluated by first seeding B16F10 cells, pre-stained with CellTracker Green CMFDA Dye (Thermo-Fisher Scientific), onto a 24-well plate (1×10^4 cells/well) and co-culturing them with B16F10 tumor lysate-stimulated T cells (1×10^6 cells/well). After 24 h, cancer cells were stained with PI, and the population of dead (CMFDA$^+$/PI$^+$) cancer cells was analyzed by flow cytometry. In some experiments, the anticancer effects of T cells were evaluated by staining T cells with FITC-conjugated anti-mouse CD3 antibody or APC-conjugated anti-mouse CD3 antibody (BioLegend; catalog #100235, clone 17A2, lot #B256435). Then cells were fixed and permeabilized using a transcription factor buffer set (BioLegend) and incubated with Alexa Fluor 647-conjugated anti-mouse granzyme B antibody (BioLegend; catalog #515406, clone GB11, lot #B233111) or PE-conjugated anti-mouse IFN-γ antibody (BioLegend; catalog #505808, clone XMG1.2, lot #B265789) for 1hr and the percentage of CD3$^+$Granzyme B$^+$ or CD3$^+$IFN-γ$^+$cells analyzed by flow cytometry. For real-time monitoring of stimulated T cell-mediated cancer cell lysis, T cells pre-stained with CellTracker Green CMFDA dye were seeded onto a 24-well plate and cocultured with B16F10 cells stained with CellTracker Red CMTPX dye (Thermo-Fisher Scientific) at a T cell:cancer cell ratio of 100:1. Cancer cell lysis was recorded in real time over 45 h using an Operetta High-Content Imaging System (PerkinElmer, Waltham, MA, USA).

2.2.16. In vitro study of FoxP3 expression

The expression levels of FoxP3 in T cells after treatment with various nanoparticles were evaluated by flow cytometry. T cells were seeded onto 24-well plates (1×10^6 cells/well) and treated with various nanoparticles containing 20 µM fenofibrate for 48 h. Cells were harvested, washed with

PBS, and stained with FITC-conjugated anti-mouse CD3 antibody, PE/Cy5-conjugated anti-mouse CD25 antibody (Biolegend; catalog #102010, lot #B277468) and PE-conjugated anti-mouse CD4 antibody (Biolegend; catalog #116006, lot #B255181) for 1 h. Cells were fixed and permeabilized using a transcription factor buffer (BioLegend) and incubated with APC-conjugated anti-mouse FoxP3 antibody (Invitrogen; catalog #17-5773-82, lot #1984797) for 1 h.

2.2.17. In vivo T cell targeting of nanoparticles

In vivo T cell targeting of nanoparticles was evaluated using molecular imaging and flow cytometry. Six-week-old mice were subcutaneously inoculated in the right flank with 5×10^5 B16F10 cells. After 7 days, mice were injected intratumorally with various FITC-labeled nanoparticle preparations. For molecular imaging, the fluorescence intensity of tumor tissue was recorded at various time points using an IVIS Spectrum in Vivo Imaging System (PerkinElmer). For flow cytometry, tumors were extracted at 24 h immediately after injection of FITC-labeled nanoparticles. T cells in extracted tumors were analyzed by incubation with APC-conjugated anti-mouse CD3 antibody and the percentage of $CD3^+FITC^+$ cells was determined by flow cytometry.

The distribution of nanoparticles to T cells was visualized by first extracting the tumor and fixing it by incubating with 4% formaldehyde for 4 h at RT. The tissue was then embedded in OCT cryostat sectioning medium, frozen at -80 °C, and sectioned at 10 μm using a Leica CM 3050 S microtome (Leica). The tumor sections were washed three times with PBS and blocked with 1% BSA in PBS for 30 min. After blocking, the sections were incubated with APC-conjugated anti-CD3 antibody (BioLegend; catalog #100235, lot #B290370) for 12 h at 4 °C. After staining with DAPI, tissue fluorescence was assessed under a confocal laser-scanning microscope (LSM 5 Exciter; Carl Zeiss).

2.2.18. In vivo PPARα expression measurement

T cell lipid metabolism in vivo was evaluated by measuring PPARα expression. B16F10 cells (5×10^5 cells) were subcutaneously inoculated into the right flank of 5-wk-old C57BL/6 mice. After 7 days, DOX (50 μg/mouse) and MPL (20 μg/mouse) were injected intratumorally. On days 10 and 12 after B16F10 cell inoculation, various nanoparticle preparations (18 μg fenofibrate/mouse) were administered intratumorally. On day 14, mice were sacrificed and extracted tumors were stained with FITC-conjugated anti-mouse CD3 antibody and Alexa Fluor 647-conjugated anti-mouse PPARα antibody (Santa Cruz Biotechnology; catalog #sc-398394, lot #H1017) for 1 h, followed by flow cytometry. For immunofluorescence staining, tumors were extracted and fixed with 4% formaldehyde for 4 h at RT, after which the tissue was embedded in OCT and cryosectioned at a

thickness of 10 μm with a Leica CM 3050 S microtome (Leica). After permeabilizing tissue with 0.3% Triton X-100 (Sigma-Aldrich) in PBS for 10 min and blocking with 0.025% Triton X-100 and 1% BSA in PBS for 1 h, the sections were incubated with FITC-conjugated anti-mouse CD3 antibody and Alexa Fluor 647-conjugated anti-mouse PPARα antibody (Santa Cruz Biotechnology). Tissues were then counterstained with DAPI and observed under a confocal laser-scanning microscope (LSM 5 Exciter; Carl Zeiss).

2.2.19. In vivo lipid uptake and metabolite imaging in T cells

Lipid uptake and metabolism in T cells was assessed by flow cytometry and matrix assisted laser desorption ionization (MALDI) imaging mass spectrometry, respectively. Briefly, mice were injected intratumorally with 25 μg/kg BODIPY C_{16} on the day after the last injection of nanoparticles. After 4 h, tumors were extracted and T cells were stained with APC-conjugated anti-mouse CD3 antibody for 1 h and the percentage of $CD3^+BODIPY^+$ T cells was analyzed by flow cytometry. For lipid metabolite analysis, F/ANs and aCD3/F/ANs were administered intratumorally on days 10 and 12. On day 14, tumors were extracted and embedded in 2% carboxymethyl cellulose (Sigma-Aldrich) and cryosectioned at 10 μm with a Leica CM 3050 S microtome (Leica). Frozen tissue sections were mounted onto indium-tin-oxide–coated glass slides (Bruker, Billerica, MA, USA) and then were sprayed with 10 mg/mL solution of a α-cyano-4-hydroxycinnamic acid (Bruker) in 70% acetonitrile with 0.1% trifluoroacetic acid. The samples were scanned over the relevant molecular weights, and the distribution of representative metabolites was determined using a rapifleX system (Bruker).

2.2.20. In vivo assessment of fatty acid oxidation-associated gene expression

In vivo expression levels of fatty acid oxidation-associated genes in CD3-positive T cells were measured RT-PCR and western blot. Briefly, tumors were extracted and digested by 1 mg/mL collagenase (Sigma-Aldrich). Single cells were stained with APC conjugated anti-mouse CD3 antibody and CD3-positive cells were collected using BD FACSAria™ III sorter (BD Biosciences, San Jose, CA, USA). For RT-PCR, total RNA was isolated from CD3-expressing T cells using the TRIzol reagent (Thermo-Fisher Scientific). cDNA was synthesized from mRNA using an AccuPower RT PreMix. Quantitative real-time RT-PCR was performed using a LightCycler FastStart DNA Master SYBR Green I system. For western blot, CD3-expressing T cells were lysated with RIPA buffer containing protease inhibitor. The amounts of protein were quantified by BCA assay. Primary antibodies for detecting following proteins were uses: anti-mouse CPT1B (Proteintech), anti-mouse LCAD (Proteintech), anti-mouse MCAD (Proteintech) and anti-mouse β-actin (Cell signaling). HRP-linked anti-

rabbit IgG (Cell signaling) was used as secondary antibody. Amersham ECL Prime Western Blotting detection reagent was used for signal detection.

2.2.21. In vivo antitumor efficacy

The in vivo antitumor activity of various nanoparticle preparations was evaluated by monitoring B16F10 tumor growth. B16F10 cells (5×10^5 cells) were subcutaneously inoculated into the right flank of 5-wk-old C57BL/6 mice. After 7 days, DOX (50 μg/mouse) and MPL (20 μg/mouse) were injected intratumorally, and on days 10 and 12, various nanoparticle preparations containing fenofibrate (18 μg/mouse) were administered intratumorally. Tumor size was measured in two dimensions every 2 days using a slide caliper, and tumor volume was calculated as $a \times b \times b \times 0.5$, where a and b are the lengths of the largest and smallest dimensions [16].

2.2.22. Detection of tumor-infiltrating lymphocytes and cytokines

Tumor infiltrating lymphocytes (TILs) and cytokines in tumor tissues were measured by flow cytometry and immunofluorescence staining. For flow cytometry, extracted tumors were digested by incubating with 1 mg/mL collagenase (Sigma-Aldrich) in RPMI-1640 medium and the resulting cell suspensions were stained with a mixture of FITC-conjugated anti-mouse CD3 antibody and APC-conjugated anti-mouse CD8a antibody (BioLegend; catalog #100712, clone 53-6.7, lot #B266721) for 1 h. TIL function was assessed by staining cell suspensions with FITC-conjugated anti-mouse CD3 antibody, Alexa Fluor 647-conjugated anti-human/mouse granzyme B antibody (BioLegend; catalog #515406, clone GB11, lot #B233111), and PE-conjugated anti-mouse IFN-γ antibody (BioLegend; catalog #505808, clone XMG1.2, lot #B265789) for 1 h.

For immunofluorescence staining, tumors were first extracted and fixed with 4% formaldehyde for 4 h at RT. The tissue was then embedded in OCT and cryosectioned at a thickness of 10 μm using a Leica CM 3050 S microtome (Leica). After tissue permeabilization, sections were incubated with PerCP/cyanine 5.5-conjugated anti-CD8 antibody (BioLegend; catalog #100734; lot #B277115), PE-conjugated anti-IFN-γ antibody, and Alexa Fluor 647-conjugated anti-human/mouse granzyme B antibody for 12 h at 4°C. The tissue was then washed three times with PBS, followed by staining with DAPI. Tissue fluorescence was observed using a confocal laser-scanning microscope (LSM 5 Exciter; Carl Zeiss).

2.2.23. In vivo toxicity study

Five-week-old C57BL/6 mice were subcutaneously injected twice with various nanoparticles. Two days after first injections, whole blood and serum samples were collected for analysis of hematological parameters regarding to white blood cell (WBC), red blood cell (RBC), hemoglobin (Hb), hematocrit (HCT), mean corpuscular volume (MCV), mean corpuscular hemoglobin (MCH), mean corpuscular hemoglobin

concentration (MCHC), neutrophil, lymphocyte, monocyte, eosinophil, alanine aminotransferase (ALT), aspartate transaminase (AST), blood urea nitrogen (BUN) and creatinine. Organs (liver, lung, heart, spleen, kidney) were collected for hematoxylin and eosin staining.

2.2.24. Statistics

A one-way analysis of variance (ANOVA) with the Student−Newman−Keuls post-hoc test was used for statistical analyses. Experimental data were analyzed with SigmaStat software (version 12.0, Systat Software). A *P*-value less than 0.05 was considered statistically significant (***p<0.001, **p<0.01, and *p<0.05).

2.3. Results
2.3.1. Characterization of aCD3/F/ANs

aCD3/F/ANs were characterized based on the physicochemical features of morphology, size, and surface charge. The structures of the various nanoparticle preparations are illustrated in Figure 2A. Hydrophobic fenofibrate was encapsulated in self-assembled AP nanoparticles, and the surfaces of F/ANs were chemically modified with an anti-CD3 antibody, resulting in aCD3/F/ANs. TEM revealed that aCD3/F/AN particles were spherical in shape (Figure 2B), and dynamic light scattering data showed that the sizes of aCD3/F/ANs did not significantly differ compared with those of F/ANs (Figure 2C). The surface zeta potentials of all nanoparticles were negative regardless of antibody modification (Figure 2D). EDS-TEM showed the presence of elemental sulfur in aCD3/F/ANs, reflecting the presence of the anti-CD3 antibody (Figure 2E). The amount of fenofibrate per nanoparticle was not significantly different between F/ANs and aCD3/F/ANs (Figure 2F). F/ANs and aCD3/F/ANs retained their stability in PBS for at least 7 days (Figure 2G). The in vitro release of fenofibrate from aCD3/F/ANs was pH-dependent. At pH 7.4 and 6.8, less than 20% of fenofibrate was released from nanoparticles over 8 h. However, at pH 5.0, the release of fenofibrate from aCD3/F/ANs was greater than 60% at 8 h (Figure 2H).
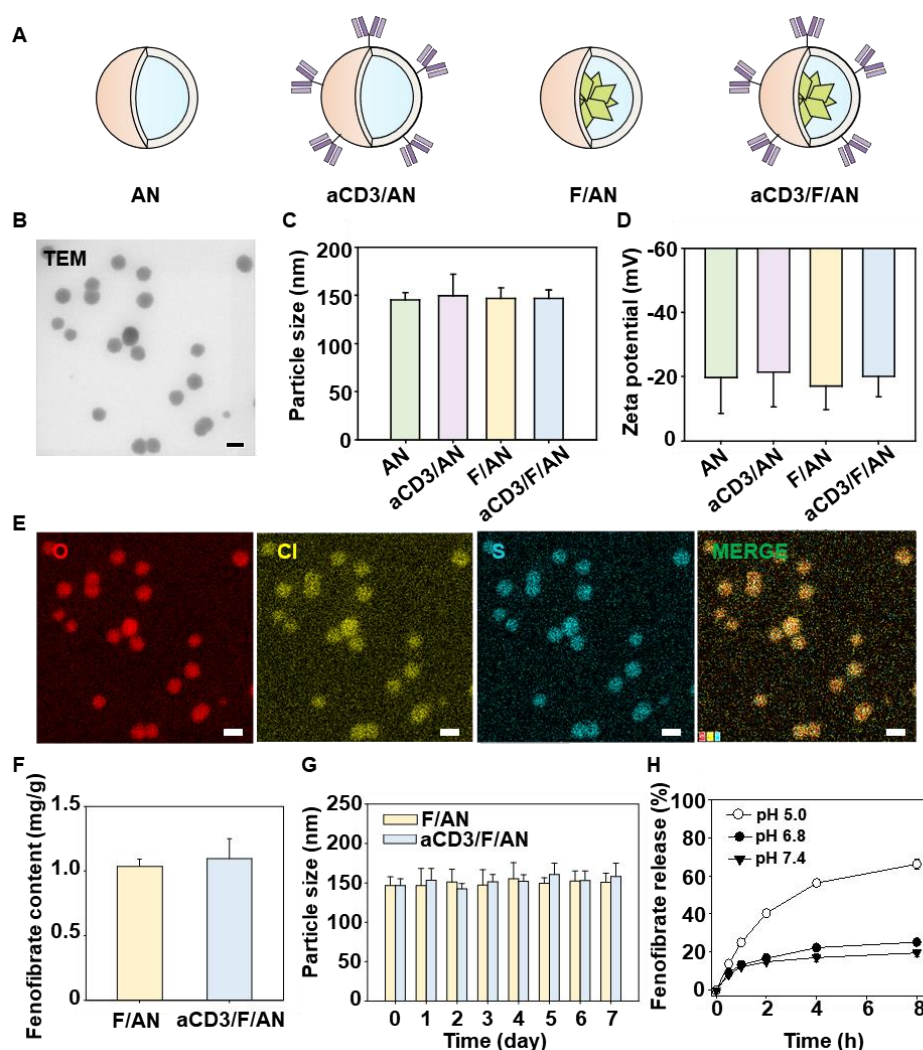
Figure 2. Characterization of nanoparticles. A) Schematic illustration of ANs, aCD3/ANs, F/ANs and aCD3/F/ANs. B) Morphology of aCD3/F/ANs, observed by TEM. Scale bar: 200 nm. C) Mean particle size of different nanoparticles, determined using DLS. D) Zeta potential of nanoparticles, measured by laser Doppler microelectrophoresis. E) Characterization of aCD3/F/ANs with respect to the elements oxygen, chloride and sulfur, conducted by STEM-EDS. Scale bar: 200 nm. F) Amount of fenofibrate encapsulated in nanoparticles, quantified by HPLC. G) Particle sizes of F/ANs and aCD3/F/ANs in PBS, monitored for 7 days. H) Release of fenofibrate from aCD3/F/ANs, quantified by HPLC under different pH conditions (***$p<0.001$).

2.3.2. Uptake of aCD3/F/ANs by T cells

The uptake of aCD3/F/ANs by T cells was monitored by confocal microscopy (Figure 3A) and flow cytometry (Figure 3B, C) using fluorescent dye-labeled nanoparticles. Confocal fluorescence microscopy

revealed negligible uptake of F/fANs by T cells. Similarly, there was no notable uptake of a physical mixture of anti-CD3 antibody and fANs. In contrast, treatment with aCD3/F/fANs resulted in higher uptake of nanoparticles by T cells. Consistent with confocal microscopy images, flow cytometry showed that the fluorescence-positive T cell population was highest after treatment with aCD3/F/fANs (Figure 3B), which resulted in a 3.8-fold higher fluorescence-positive T cell population compared with that observed in other treatment groups (Figure 3C).
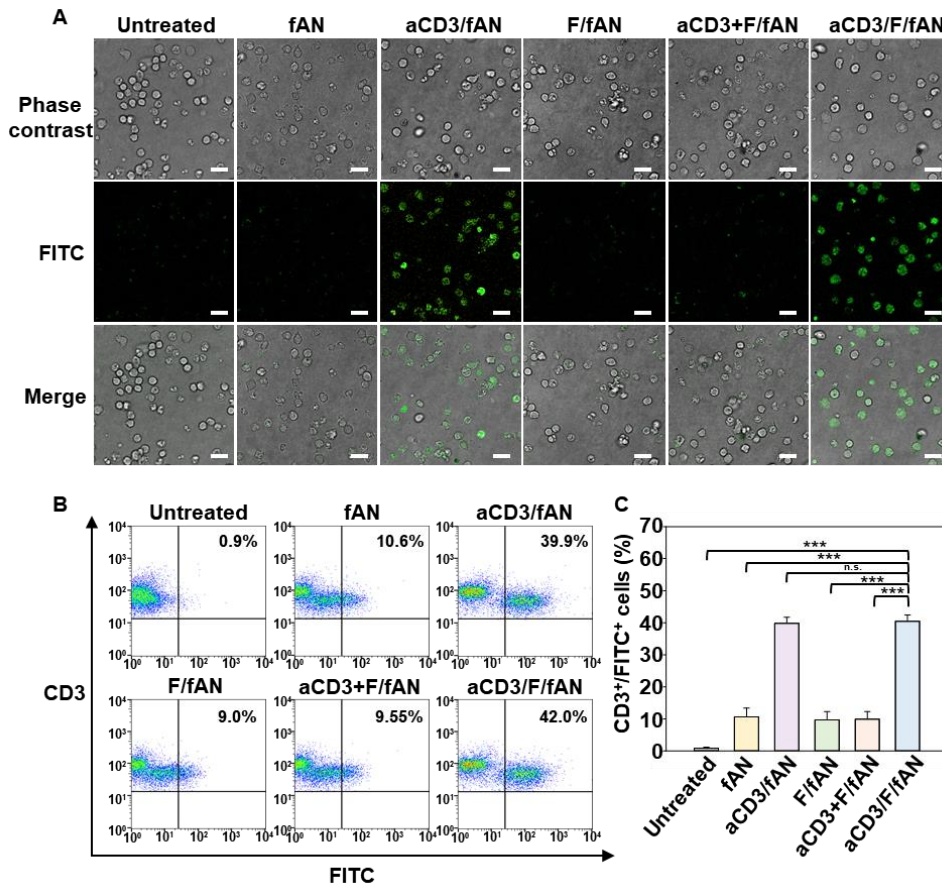
Figure 3. Uptake of nanoparticles by T cells. Mouse spleen-derived T cells were incubated with various fenofibrate-containing nanoparticle preparations. After 24 h, cellular uptake of nanoparticles was visualized by confocal microscopy (A) and quantified by flow cytometry (B, C) (***$p<0.001$, n.s., not significant). Scale bar: 10 μm.

2.3.3. Effect of aCD3/F/ANs on the expression of fatty acid metabolism-related genes and lipid uptake in T cells

Treatment of T cells with aCD3/F/ANs affected fatty acid oxidation-related gene expression levels and lipid uptake. The cellular mechanism underlying PPARα-mediated lipid metabolism enhancement is shown in Figure 4. To evaluate metabolic reprogramming quantitatively, the

expression levels of PPARα in T cells were measured by flow cytometry. It was revealed that expression levels of PPARα were highest in T cells treated with aCD3/F/ANs (Figure 5A, 5C). The PPARα-positive T cell population increased by more than 7.2-fold upon treatment with aCD3/F/ANs compared with the untreated group. In addition, the expression level of a fatty acid translocase CD36, which exists on cell membrane, was also evaluated by flow cytometry. The expression of CD36 was 2.2-fold higher in the aCD3/F/AN group compared with the F/AN group (Figure 5B, 5D). Western blot data showed that aCD3/F/ANs significantly increased the protein expression levels of CPT1B, LCAD, and MCAD compared to untreated and other groups (Figure 5E). Consistently, mRNA level of CPT1B, LCAD, and MCAD was increased by 4.4-fold, 2.5-fold, and 2.8-fold, respectively, compared with untreated cells (Figure 5H). Since one consequence of the observed changes in gene expression is an increased rate of lipid uptake, lipid uptake by T cells was measured using fluorescent dye-labeled lipid, BODIPY C_{16}. Compared with untreated cells, T cells treated with ANs, aCD3/ANs, F/AN, or with a mixture of anti-CD3 antibody and F/ANs (aCD3 + F/ANs) showed no significant change in lipid uptake by T cells (Figure 5F). In contrast, treatment of T cells with aCD3/F/ANs increased lipid uptake 3.1-fold compared with untreated cells (Figure 5G).
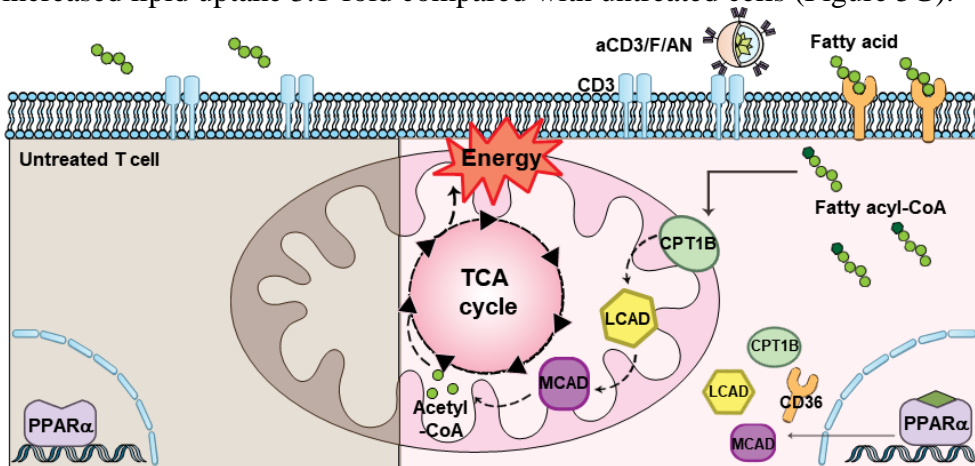
Figure 4. The cellular mechanism underlying aCD3/F/AN-induced enhancement of lipid metabolism is illustrated. The left half of the schematic cell depicts the untreated condition, and the right half shows treatment with aCD3/F/ANs. aCD3/F/AN treatment is proposed to activate PPARα in T cells, leading to over-expression of fatty acid metabolism-associated proteins, including CD36 (fatty acid translocase), CPT1B, LCAD, and MCAD. The increased fatty acid metabolism in mitochondria generates higher energy via the TCA cycle.
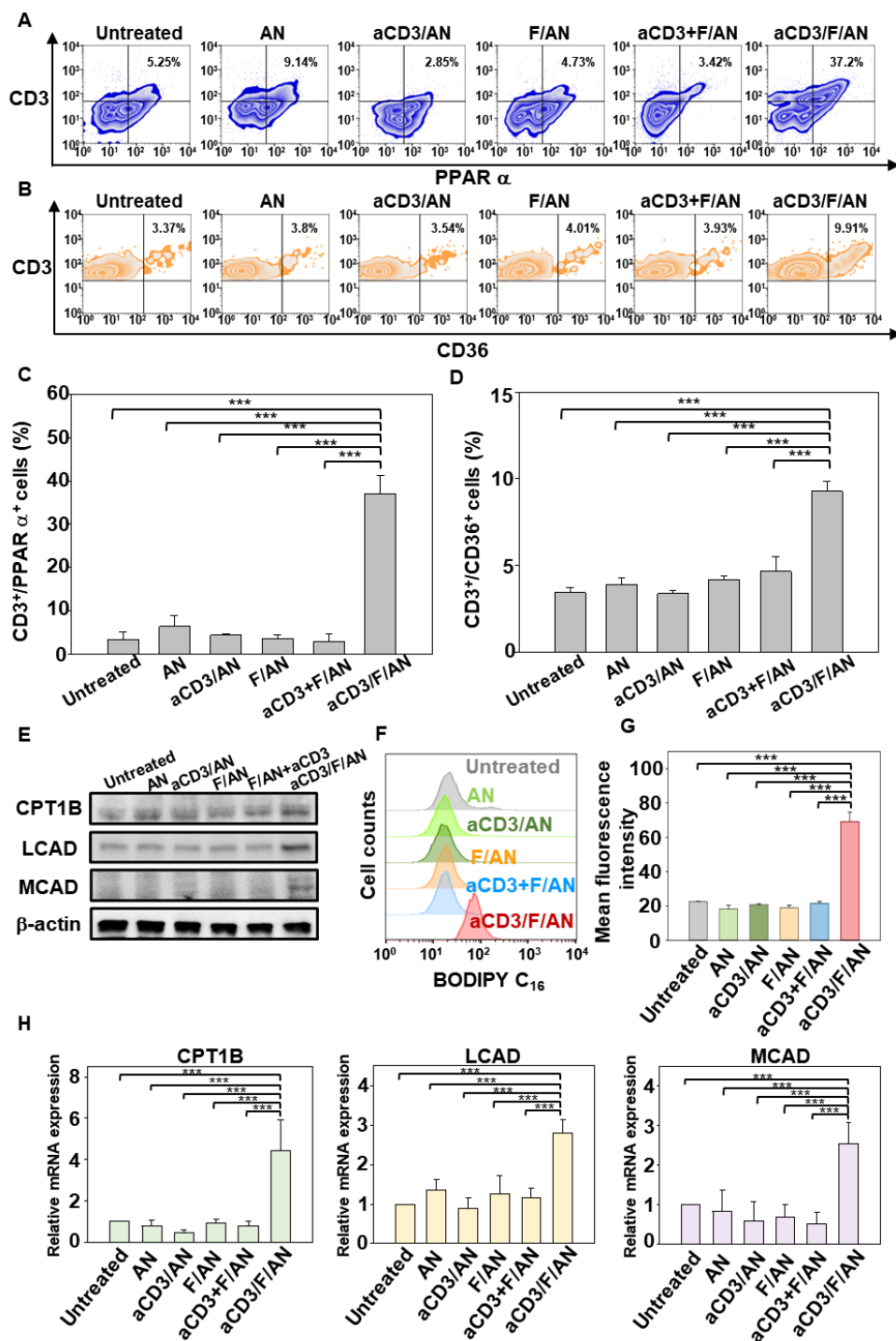
Figure 5. Fatty acid metabolism-associated gene expression and lipid uptake in T cells. A, C) The corresponding levels of PPARα protein in T cells (PPARα⁺/CD3⁺), measured by flow cytometry. B, D) The levels of CD36 protein in T cells (CD36⁺/CD3⁺), measured by flow cytometry. E) The protein levels of CPT1B, LCAD and MCAD in T cells were measured

by western blot. F, G) T cells treated with different nanoparticle preparations were incubated with fluorescent lipid BODIPY C_{16}, and the association of fluorescent lipid with T cells was determined by flow cytometry (F) and expressed as mean fluorescence intensity (G) (***$p<0.001$). H) mRNA expression levels of the fatty acid metabolism-associated genes, CPT1B, LCAD and MCAD, determined by RT-PCR (***$p<0.001$).

2.3.4. T cell mitochondrial activation by aCD3/F/ANs

Mitochondrial functions in T cells, including fatty acid metabolism, were modulated by treatment with aCD3/F/ANs. To mimic the glucose-deficient tumor microenvironment, T cells were incubated in low-glucose medium. In low-glucose environment containing palmitate as a lipid source, untreated T showed poorly-defined mitochondrial cristae with shrunken morphologies compared to the mitochondrial of T cells in high-glucose condition (Figure 6A). In contrast, T cells treated with aCD3/F/ANs showed mitochondrial structures with clear cristae, similar to those observed in high glucose environment. In addition to altering the morphology of mitochondria, aCD3/F/ANs increased mitochondrial membrane potential, with fluorescent dye staining revealing the highest mitochondrial membrane potential in T cells treated with aCD3/F/ANs (Figure 6B). Treatment with aCD3/F/ANs in palmitate-supplemented low-glucose medium expanded the population of T cells with increased mitochondrial membrane potential by more than 6.3-fold compared with other treatment groups (Figure 6C).

aCD3/F/AN-mediated delivery of fenofibrate to T cells enhanced lipid metabolism and mitochondrial activity. However, the ECAR value, an indicator of glycolysis, showed little difference among groups, suggesting similar levels of glycolysis in all groups (Figure 6D). In contrast to ECAR, basal OCR, an indicator of mitochondrial respiration, was significantly higher in the aCD3/F/AN-treatment group compared with other groups (Figure 6E, F). In addition, spare respiratory capacity (SRC), which is related to the extra ATP capacity produced by mitochondrial metabolism during a sudden increase in energy demand (calculated by subtracting minimal respiration from maximal respiration), was highest in the aCD3/F/AN-treatment group, reaching a level 8-fold higher than that in the F/AN group (Figure 6G). Moreover, the aCD3/F/AN group exhibited the highest ratio of OCR to ECAR, with a value 2.2-fold higher than that of the F/AN-treated group (Figure 6H). Consistent with the observed enhancement in lipid metabolism, aCD3/F/AN treatment significantly increased the production of β-hydroxybutyrate, a major lipid metabolite (Figure 6I), increasing it by 2.2-fold upon palmitate supplementation compared with F/ANs.
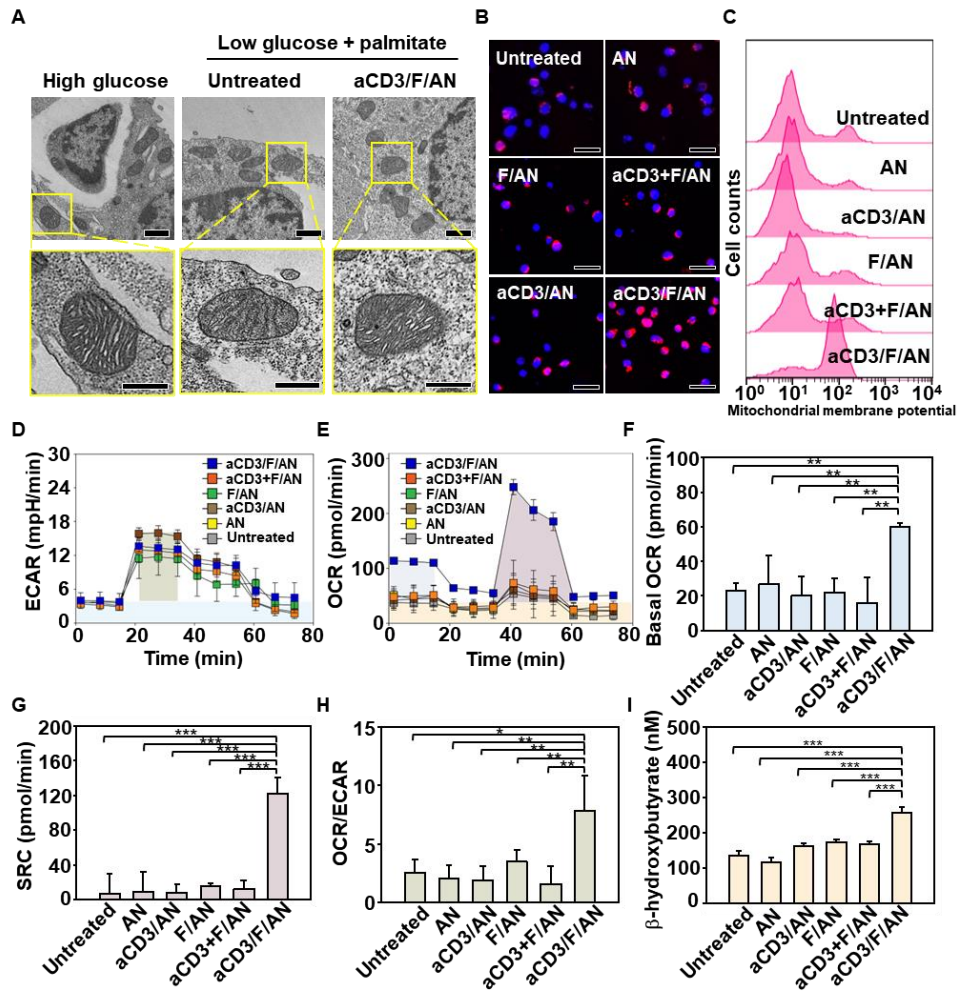
Figure 6. Mitochondrial morphology, membrane potential, and fatty acid metabolism in T cells. T cells were treated with aCD3/F/ANs in low-glucose medium supplemented with palmitate as a lipid source. A) TEM of mitochondria of T cells in high-glucose medium or low-glucose medium with or without aCD3/F/AN treatment. Scale bar: 1 μm (upper panels) and 500 nm (lower panels). B) Mitochondrial membrane potential, assessed using MitoTracker Orange CMTMRos and visualized by confocal fluorescence microscopy. C) Populations of T cells with increased mitochondrial membrane potentials, quantified by flow cytometry. D, E) ECAR (D) and OCR (E), measured using a Seahorse XFp analyzer. F-H) Basal OCR (F), SRC (G) and OCR/ECAR H values, obtained based on ECAR and OCR values (*$p<0.05$, **$p<0.01$). I) β-Hydroxybutyrate secretion levels (***$p<0.001$).

2.3.5. In vitro proliferation of metabolically reprogrammed T cells

Treatment with aCD3/F/ANs affected the survival and proliferation of T cells. In these experiments, T cells were treated with various nanoparticle

formulations under glucose-deficient conditions. In some experiments, low glucose medium was supplemented with palmitate as a lipid source. Fluorescent dye-based live/dead assays revealed that, in such a glucose-deficient, but palmitate-replete, environment, the aCD3/F/AN-treatment group showed the highest fraction of live T cells (Figure 7B) and a significantly higher annexin V⁻/PI⁻ cell population compared with other treatment groups (Figure 7C, D). In addition, upon palmitate supplementation, the proliferation of aCD3/F/AN-treated T cells was 5.4-fold higher than that in the untreated group (Figure 7E).
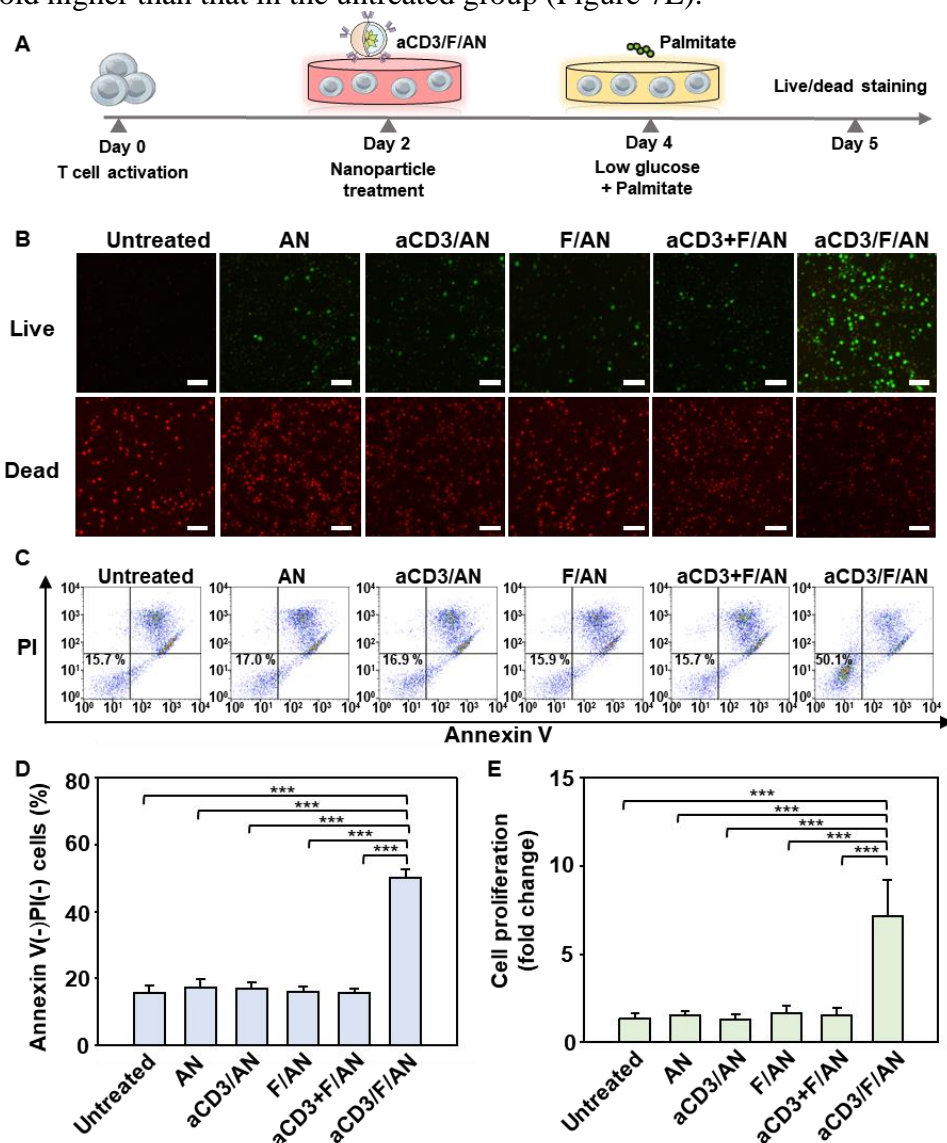
Figure 7. Enhanced T cell survival and proliferation induced by metabolic reprogramming. T cells were activated and treated with various nanoparticle preparations and incubated under glucose-limiting conditions, with or without a lipid source. A) Illustration of the experimental scheme. B) Live

and dead T cells, visualized by fluorescent dye staining. Scale bar: 10 µm. C, D) T cells were stained with annexin V and PI, and the annexin V⁻/PI⁻ population was quantified for each group (***p<0.001). E) Proliferation of T cells, measured using WST-1 assays (***p<0.001).

2.3.6. In vitro cancer cell-killing activity of aCD3/F/AN-treated T cells

The treatment with aCD3/F/ANs enhanced the cancer cell-killing activity of T cells. Upon co-incubation of T cells with B16F10 melanoma cells, the levels of granzyme B and IFN-γ in aCD3/F/AN-treated T cells were 2.3- and 3.0-fold higher compared with those in the F/AN-treated group, respectively (Figure 8B-8E). The cancer cell-killing activity of T cells treated with ANs, F/ANs, aCD3/AN, or aCD3 + F/AN, were not different from those of untreated T cells (Figure 8F). However, the population of dead cancer cells following incubation with aCD3/F/AN-treated T cells was 15.6-fold higher than that following incubation with T cells treated with aCD3 + F/ANs. Real time video recordings further showed that untreated T cells did not attack B16F10 cells, whereas aCD3/F/AN-treated T cells vigorously attacked B16F10 cells. The images of untreated T cells and aCD3/F/AN-treated T cells captured at various time points are shown in Figure 8G.
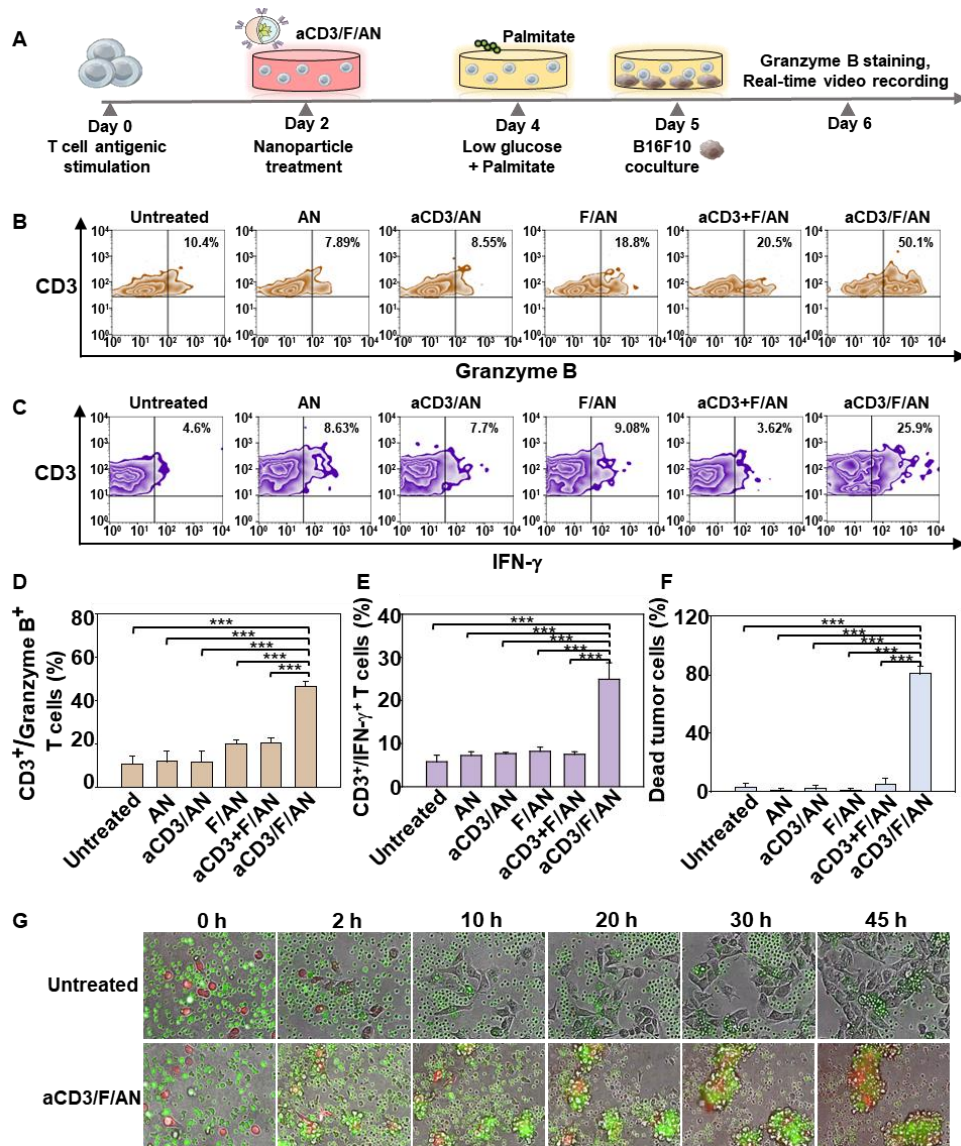
Figure 8. In vitro anticancer activity of aCD3/F/AN-treated T cells. T cells were treated with various nanoparticle preparations and co-incubated with B16F10 cells under glucose-limiting conditions in the presence of palmitate as a lipid source. A) Illustration of the experimental scheme. B, C) Flow cytometry data of T cells positive with granzyme B (B) and IFN-γ (C). D, E) The populations of T cells positive with granzyme B (D) and IFN-γ (E) were quantified. (***$p<0.001$). F) Dead cancer cell population, quantified by flow cytometry (***$p<0.001$). G) Lysis of cancer cells by T cells, recorded in real time. Cancer cells were labeled with red fluorescent dye, whereas T cells were labeled with green fluorescent dye.

2.3.7. In vivo distribution of aCD3/F/ANs to T cells in tumor tissues

The in vivo distribution of nanoparticles to T cells in tumor tissues was visualized by determining colocalization with T cells in fluorescence images.

3 4

aCD3/F/fANs showed the highest retention in tumor tissues compared with F/fANs and the aCD3 + F/AN group (Figure 9A). An intensity analysis showed that the distribution of nanoparticles to tumor tissues over 72 h post-dose was highest in the group treated with aCD3/F/fANs (Figure 9B). Uptake of nanoparticles by T cells in tumor tissues was tested by assessing colocalization of nanoparticles and the $FITC^+CD3^+$ T cell population. The colocalization of nanoparticles to $CD3^+$ T cells was highest in the aCD3/F/fAN-treatment group, which exhibited 7.6-fold greater colocalization than the F/fAN group at 24 h (Figure 9C, D). Tumor tissue staining showed higher colocalization of aCD3/F/fANs with $CD3^+$ T cells in tumor tissues (Figure 9E).
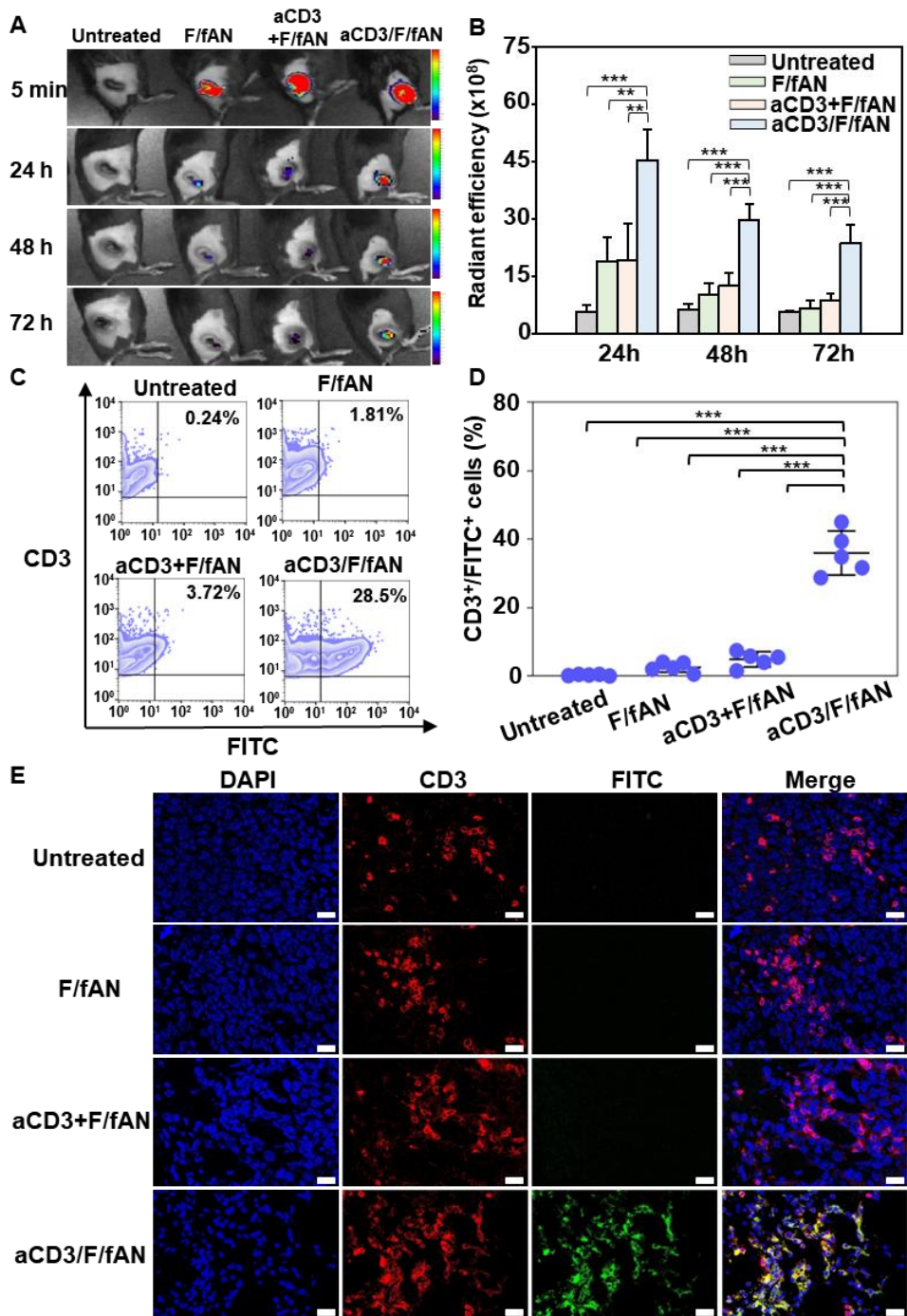
Figure 9. In vivo T cell-targeting ability of aCD3/F/ANs. T cell targeting ability was evaluated by intratumorally injecting mice (n=3) with various nanoparticle preparations containing fenofibrate. A) In vivo fluorescence at tumor sites, visualized at different time points. B) Quantification of fluorescence in tumor sites at different time points (**$p<0.01$, ***$p<0.001$). C) Uptake of nanoparticles in tumor-resident T cells, analyzed by flow cytometry. D) $CD3^+FITC^+$ T cell population, quantified for each treatment

group (***$p<0.001$). E) Colocalization of nanoparticles (green) with CD3$^+$ T cells (red), visualized by confocal microscopy. Scale bars: 20 μm.

2.3.8. Reprogramming of in vivo fatty acid metabolism in aCD3/F/AN-treated T cells

The intratumoral administration of aCD3/F/ANs modulated in vivo PPARα expression, lipid uptake, and metabolism by T cells. The in vivo experimental scheme is illustrated in Figure 10A. Flow cytometry showed that PPARα-positive (Figure 10B) and BODIPY C$_{16}$-positive (Figure 10C). T cell populations were increased to a greater extent in the aCD3/F/AN-treatment group. Expression of PPARα was increased 4.1-fold and 2.6-fold in this group compared with F/AN- and aCD3+F/AN-treatment groups, respectively (Figure 10D). Uptake of BODIPY C$_{16}$ lipid was almost 2-fold higher in the aCD3/F/AN-treatment group than in other groups (Figure 10E). Mice treated with aCD3/F/AN showed significantly increased protein expression and mRNA levels of CPT1B, LCAD, and MCAD compared with untreated group (Figure 10F, G). Immunostaining revealed distinct PPARα expression in CD3$^+$ T cells in tumor tissues, as demonstrated by colocalization of CD3 and PPARα staining (Figure 10H, I). MALDI imaging revealed enhanced levels of the fatty acid oxidation metabolites, acetoacetate, β-hydroxybutyrate and palmitoylcarnitine, in T cells treated with aCD3/F/ANs (Figure 10J).
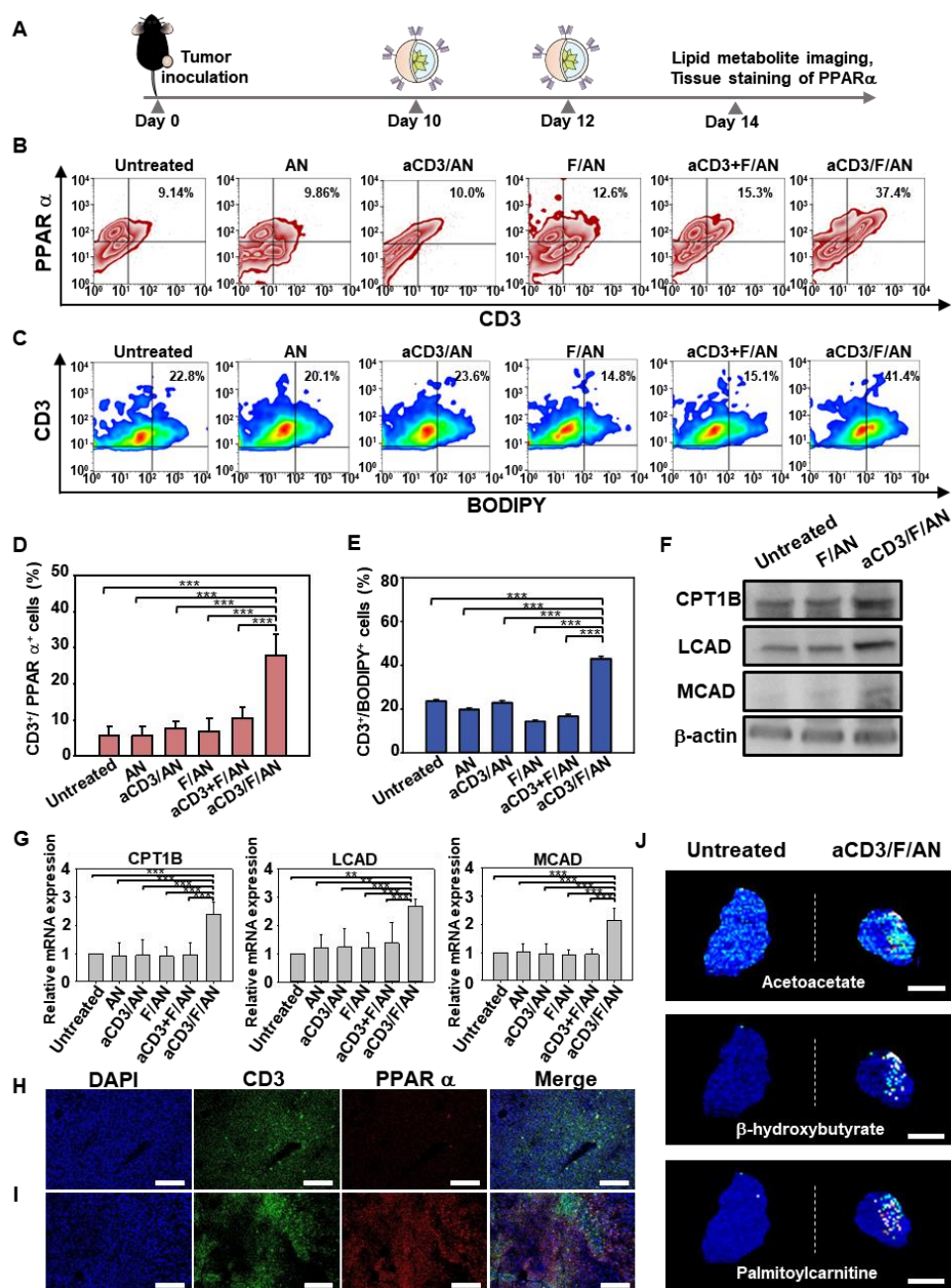
Figure 10. In vivo PPARα expression and lipid uptake by T cells in tumor tissues. A) B16F10 tumor-bearing mice were intratumorally injected with various nanoparticle preparations on days 10 and 12 after tumor inoculation. On day 13, BODIPY C_{16} was intratumorally injected, and on day 14, tumor tissues were extracted and analyzed. B-E) PPARα expression level in T cells (B, D) and BODIPY C_{16}-positive CD3 T cells (C, E), analyzed by flow cytometry (***$p<0.001$). F) Protein expression levels of CPT1B, LCAD and MCAD in tumor infiltrating T cells were determined by western blot. G) mRNA expression levels of the fatty acid metabolism-associated genes

CPT1B, LCAD and MCAD in tumor infiltrating T cells were determined by RT-PCR (***p<0.001). H, I) Confocal microscopic images of untreated (H) and aCD3/F/AN-treated tumor tissue (I) stained with anti-CD3 (green) and anti-PPARα (red) antibody. Scale bars: 100 μm. J) Tumor tissue distribution of acetoacetate (m/z=103.09), β-hydroxybutyrate (m/z=105.10) and palmitoylcarnitine (m/z=400.60), as visualized by MALDI imaging. Scale bar: 5 μm.

2.3.9. In vivo antitumor efficacy of metabolically reprogrammed T cells

   To assess the effects of aCD3/F/ANs on tumor growth and the survival of mice, B16F10 tumor-bearing mice were intratumorally injected with various nanoparticle preparations twice, once on day 10 after tumor inoculation and again on day 12 (Figure 11A). aCD3/F/AN treatment exerted significantly higher tumor growth-inhibitory effects than treatment with other nanoparticle preparations (Figure 11B, C). Notably, the survival rate of mice treated with aCD3/F/ANs was 100% up to day 60. In contrast, no mice survived beyond 44 days after tumor inoculation in any other treatment group (Figure 11D).
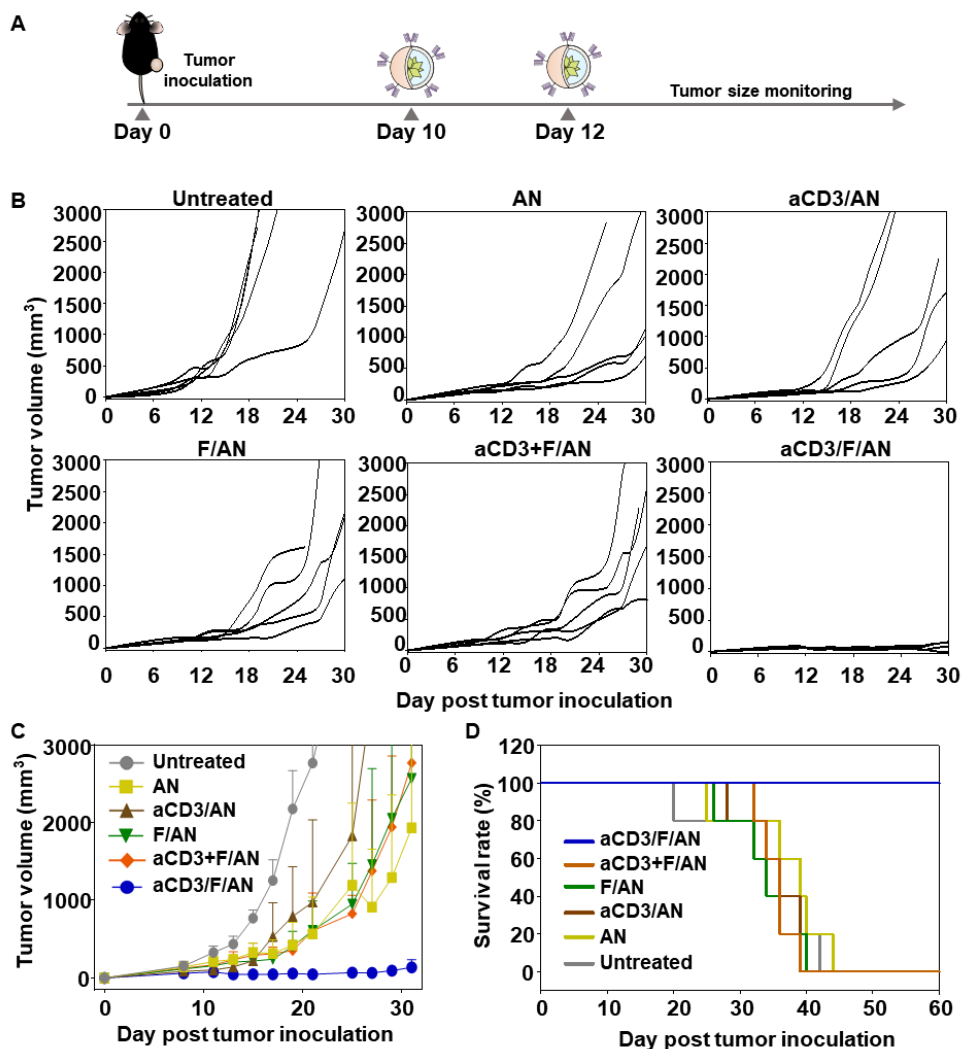
Figure 11. Antitumor effects of aCD3/F/ANs in vivo. A) B16F10 tumor-bearing mice were intratumorally injected with various nanoparticle preparations on days 10 and 12 after tumor inoculation. B, C) Antitumor efficacy, determined by measuring tumor volume. D) Survival rate in each mouse group, monitored for 60 days after tumor inoculation.

To test whether the observed antitumor efficacy was attributable to the enhanced function of metabolically reprogrammed T cells, tumor-infiltrating CD8^{+} T cells were quantified (Figure 12B). The CD8^{+} T cell population in tumor tissues was significantly increased in mice treated with aCD3/F/ANs, which exhibited a CD8^{+} T cell population in tumor tissues 14.8-times higher than that in F/AN-treated mice (Figure 12B, E). In vivo treatment with aCD3/F/ANs affected expression levels of IFN-γ and granzyme B in T cells. Specifically, IFN-γ–expressing T cells accounted for 20.5% ± 4.1% of tumor T cells in the aCD3/F/AN-treated group—a more than 5-fold increase compared with F/AN- and aCD3+F/AN-treatment groups (Figure 12C, 12F).

Similar to the IFN-γ expression pattern, the highest percentage of granzyme B–expressing T cells was observed for the group treated with aCD3/F/ANs, which showed more than a 3.9-fold increase in levels compared with other treatment groups (Figure 12D, 12G). An immunohistochemical analysis of tumor tissues showed no notable infiltration of CD8^{+} T cells in tumor tissues in the untreated mice (Figure 12H). However, considerable infiltration of CD8^{+} T cells in tumor tissues and secretion of IFN-γ and granzyme B were observed in tumors treated with aCD3/F/ANs (Figure 12I).
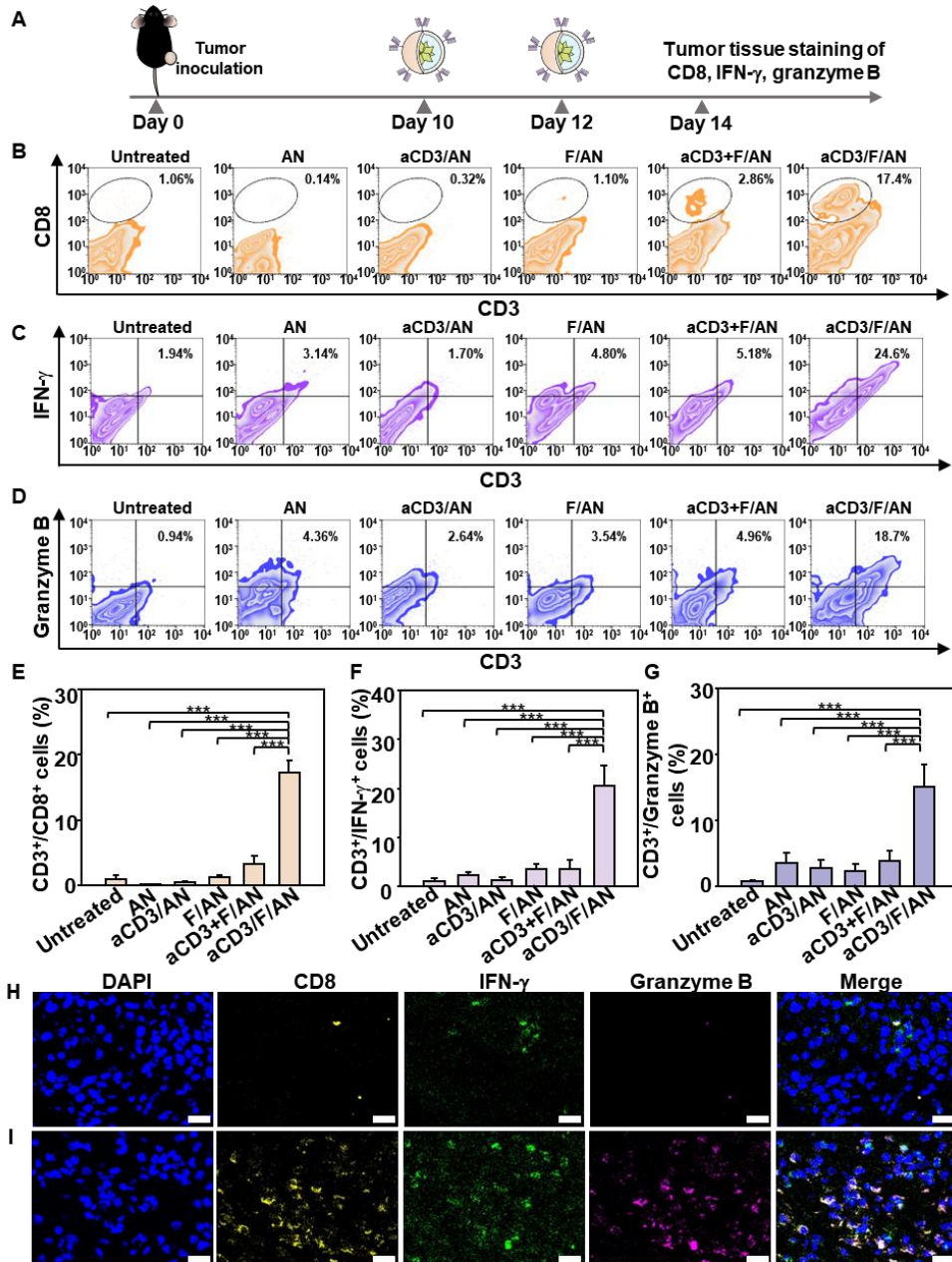
Figure 12. In vivo cytokine production by T cells in tumor tissues. A) B16F10 tumor-bearing mice were injected with nanoparticle preparations on

days 10 and 12 after tumor inoculation. On day 14, tumor tissues were extracted for analysis. B-D) Infiltrating $CD8^+$ T cells, IFN-γ–expressing T cells and granzyme B–expressing T cells among tumor tissue $CD3^+$ T cells, determined by flow cytometry (***$p < 0.001$). Populations of $CD3^+/CD8^+$ cells (E) $CD3^+/$ IFN-γ$^+$ cells (F), and $CD3^+/$granzyme$^+$ cells (G) are shown. H, I) In untreated (H), and aCD3/F/AN-treated mice (I), tumor tissues were extracted, and immunostained with anti-CD8 (yellow), anti-IFN-γ (green) and anti-granzyme B (light purple) antibodies, and counterstained with DAPI. Scale bar: 20 μm.

2.4. Discussion

This study demonstrated that enhanced delivery of fenofibrate to T cells modulated the fatty acid metabolism of T cells and stimulated their cancer cell-killing activity. T cell-directed delivery of fenofibrate was achieved by modification of the surfaces of fenofibrate-loaded nanoparticles with an anti-CD3 antibody. Uptake of aCD3/F/ANs by T cells increased mitochondrial function and the expression of fatty acid metabolism-related genes, including PPARα. T cells metabolically reprogramed by aCD3/F/ANs efficiently killed B16F10 melanoma cells in vitro, and an in vivo study showed that aCD3/F/AN treatment prevented the growth of tumors and increased the production of various cytokines.

In this study, fenofibrate was entrapped in ANs, and modified the surfaces of F/ANs with anti-CD3e f(ab')2 antibody fragments. The nanoparticle is based on the amphiphilic derivative of poly (γ-glutamic acid) which is natural biopolymer produced from Bacillus species [30]. Due to the biocompatibility and biodegradability, poly (γ-glutamic acid)-based biomaterials have been studied for delivery systems of various active substances. Poly (γ-glutamic acid) and gold nanocluster hybrid nanoparticles were reported for receptor-mediated cancer cell delivery and photothermal therapy [31]. Poly (γ-glutamic acid) coating of doxorubicin-loaded mesoporous silica nanoparticle was shown to increase the delivery to cancer cell and enhance the anticancer effect of doxorubicin [32]. Amphiphilic phenylalanine derivative of poly (γ-glutamic acid) was found to self-assemble polymeric micelles and entrap hydrophobic anticancer drugs in the hydrophobic phenylalanine core parts [22]. Moreover, the carboxylic groups at the surfaces of amphiphilic poly (γ-glutamic acid)-based nanoparticles enables the surface modification with other functional molecules such as targeting ligand chemicals and antibodies [33].

Here, fenofibrate was encapsulated inside of the AN matrix, which is thought to provide a hydrophobic core by virtue of the phenylalanine moieties of AP. The release of fenofibrate from aCD3/F/ANs at lower pH values might be attributable to protonation of carboxyl groups in AP. The CD3 receptor, which has been used as a marker of T cells [34], was chosen as a target because it is overexpressed on T cells and has been reported to induce receptor-mediated endocytosis upon binding of nanoparticles [33].

Indeed, the results showed the enhanced uptake of aCD3/F/ANs by T cells compared with plain F/ANs both in vitro (Figure 3) and in vivo in B16F10 tumor tissues (Figure 9). The comparable T cell uptake of aCD3/ANs (Figure 3) supports the major role of CD3 antibody fragments in T cell delivery. The CD3 antibody mediated delivery enable aCD3/F/ANs to show high selectivity to T cells without side effect to other cells.

CD3 receptor-mediated enhanced delivery of fenofibrate to T cells was shown to induce the expression of fatty acid uptake- and metabolism-related genes (Figure 5). The results showed that uptake of fluorescent lipid by T cells was increased only in aCD3/F/AN-treated T cells, and not T cell treated with other nanoparticle preparations (Figure 5F, 5G). The higher uptake of fluorescent lipids by aCD3/F/AN-treated T cells may be attributable to upregulation of fatty acid transport, consistent with a previous report that PPARα agonists induce up-regulation of the fatty acid transporter, CD36 [35]. Indeed, the results demonstrated that expression of CD36 was highest in T cells treated with aCD3/F/ANs (Figure 5B, 5D). CD36, known as fatty acid translocase, functions in mediating the entry of extracellular fatty acids into the cytosol of cells [36].

Fatty acids entering T cells via CD36 can be transported to mitochondria, where they feed into the TCA cycle. The results showed that treatment with aCD3/F/ANs increased the expression of CPT1B, LCAD, and MCAD (Figure 5E, 5H). CPT1B is known to increase the transport of fatty acids from the cytosol to mitochondria [37], whereas LCAD and MCAD are involved in the β-oxidation of fatty acids [38, 39]. The increased expression of fatty acid oxidation-related genes is attributable to the ability of the pharmacological agent fenofibrate to activate PPARα [40]. PPARα, the molecular target of fenofibrate, is a key transcriptional regulator of fatty acid oxidation-related genes. In association with enhanced expression of PPARα, the results showed the increased expression of the downstream fatty acid oxidation-related genes CPT1B, LCAD and MCAD. Consistent with this, it has been reported that expression of CPT1B, LCAD and MCAD is induced by activation of the transcription factor, PPARα [25].

These observations support the interpretation that uptake of aCD3/F/ANs by T cells activates fatty acid metabolism, but not glycolysis (Figure 6). The significantly higher OCR and ECAR ratio in aCD3/F/AN-treated T cells further support the conclusion that fenofibrate affected fatty acid metabolism. T cells were metabolically reprogrammed to take up and use fatty acids as an energy source. In the presence of a fatty acid energy source, the reprogrammed T cells maintained a higher metabolic state and enhanced mitochondrial function, as evidenced by the levels of lipid metabolites in aCD3/F/AN-treated T cells. Because these data showed that treatment with aCD3/ANs alone did not affect fatty acid metabolism, it is unlikely that fatty acid metabolism is affected by nanoparticles per se; instead enhanced fatty acid metabolism is attributable to activation of PPARα by fenofibrate.

Consistent with this, it has been reported that fenofibrate activates PPARα in various cell types, including endothelial cells [41], cardiomyocytes [42], and adipocytes [43].

The enhanced mitochondrial functions of aCD3/F/AN-treated T cells may be attributable to the prolonged survival, proliferation, and effector functions of T cells. T cells are known to undergo metabolic stress and exhibit mitochondrial dysfunction in glucose-deficient tumor microenvironments [44]. The TEM imaging revealed a shrunken mitochondrial morphology and decreased mitochondrial membrane potentials in glucose-deprived T cells (Figure 6A). Mitochondrial membrane potential is known to play a crucial role in ATP production and maintenance of cellular functions [45]. Treatment with aCD3/F/ANs restored clear cristae structures and membrane potentials of mitochondria. Notably, treatment with aCD3/F/ANs enhanced the cancer cell-killing effector function of T cells, likely owing to the reprogramming of T cells to use fatty acids as an alternative energy source.

Fatty acid metabolism via the TCA cycle, which can provide greater energy to T cells, may lead to the production of various cytokines, as underscored by several reports on the relationship between robust mitochondrial function and energy production in T cells on the one hand and cytokine secretion on the other. Consistent with this, the results showed that metabolic reprogramming of T cells by aCD3/F/ANs resulted in increased secretion of the cytokine, granzyme B (Figure 8). It was previously reported that fenofibrate induces mitochondrial fatty acid oxidation-mediated augmentation of the effector function of T cells by enhancing granzyme B and IFN-γ secretion [21]. Other studies have also reported that mitochondrial metabolism is essential for the ability of T cells to adapt by rapidly modifying their energy requirements. It has been reported that memory CD8$^+$ T cells maintain a higher mitochondrial metabolic rate through fatty acid oxidation and actively produce the cytokines, IFN-γ and IL-2 [46]; their mitochondrial function and secretion of IL-2 and TNF-α are also enhanced by acute infection [47]. These observations are in agreement with previous findings that mitochondrial function plays a crucial role in the production of cancer-killing cytokines by T cells.

The metabolic reprogramming of tumor-infiltrating T cells, as revealed by their elevated expression of PPARα in aCD3/F/AN-treated tumor tissues (Figure 10), contributes to the anticancer efficacy of aCD3/F/ANs. An additional contributing factor is the enhanced in vivo delivery of aCD3/F/ANs to T cells in tumor tissues, which exceeded that of all other nanoparticle preparations (Figure 9). In this study, to enhance infiltration of T cells into tumor tissues, mice were pretreated with DOX, which is reported to act as an immunogenic cell inducer [27], and MPL, used as an immunoadjuvant [28]. The enhanced infiltration and activation of T cells by aCD3/F/AN-induced metabolic reprogramming, in turn, enhanced the killing of tumor cells. This is supported by the production of the cytokines,

IFN-γ and granzyme B (Figure 12), the latter of which has been shown to be a marker of activated cytotoxic T cells [50].

In this study, the selective activation of PPARα by delivering fenofibrate only to T cells was achieved using an aCD3 antibody fragment. The selective delivery of fenofibrate can increase the amount of fenofibrate available to T cells and reduce the nonspecific distribution of fenofibrate to other tissues of the body. The importance of selective T cell targeting is supported by the demonstration that the physical combination of aCD3+F/AN produced no meaningful alterations in metabolism in virtually all experimental settings. Importantly, the lack of significant anticancer effect of aCD3+F/AN and the observation that aCD3/F/AN treatment completely abrogated tumor growth in B16F10 tumor-bearing mice support the importance of T cell targeted delivery of nanoparticles. However, aCD3/F/AN was injected intratumorally, which limits the application of the T cell lipid metabolism reprogramming strategy to invisible cancers and cancer metastasis. Therefore, in order to expand the application of this strategy in clinical settings, it is crucial to conduct further research on modifying nanoparticles to enhance the lipid metabolism of tumor-infiltrating T cells.

Although PD-1 checkpoint inhibitors have shown effectiveness in cancer treatment, not all patients respond to this therapy. One reason for this is that tumor-infiltrating $CD8^+$ T cells experience metabolic stress in the hypoglycemic tumor microenvironment. The efficacy of PD-1 blockade therapy is associated with the functions of tumor-reactive $CD8^+$ T cells. Therefore, enhancing fatty acid metabolism to maintain the anticancer functions of tumor-reactive $CD8^+$ T cells may facilitate PD-1 blockade therapy. Further studies are required to evaluate the therapeutic efficacy of aCD3/F/AN in combination with PD-1 blockade therapy and investigate whether regulating lipid metabolism of tumor-infiltrating T cells can improve the therapeutic outcomes of PD-1 blockade therapy.

Although this research targeted tumor-infiltrating T cells by aCD3/F/AN, the concept of lipid metabolic reprogramming can be broadly applied to adoptive T cell transfer. Currently, the anticancer effects of chimeric antigen receptor-engineered T cells against solid tumors are limited, partly because of their diminished viability in the hypoglycemic tumor microenvironment [51]. For adoptive T cell transfer, ex vivo pretreatment of T cells with aCD3/F/ANs might be used to fortify the survival and effector functions of these cells in the tumor microenvironment.

2.5. Conclusion

In conclusion, this research has provided evidence that metabolic reprogramming of T cells can be used as a new mode of anticancer immunometabolic therapy. The enhanced T cell delivery achieved using CD3/F/ANs was shown to activate fatty acid oxidation metabolic pathways and restore mitochondrial functions of T cells in a glucose-deficient

environment. Treatment with aCD3/F/ANs also increased effector functions of T cells against tumor cells. T cells were metabolic reprogrammed in the current study, but the concept of metabolic reprogramming as a strategy for activating anticancer effector functions can be broadly applied to the design of other immunometabolic therapies against solid tumors.

2.6. Reference

[1] Y. Li, J. Lin, P. Wang, Q. Luo, F. Zhu, Y. Zhang, Z. Hou, X. Liu, J. Liu. Tumor microen-vironment cascade-responsive nanodrug with self-targetingactivation and ROS regeneration for synergistic oxidation-chemotherapy. *Nanomicro. Lett*. **2020**, *12*, 182.

[2] D. J. Irvine, E. L. Dane. Enhancing cancer immunotherapy with nanomedicine. *Nat. Rev. Immunol*. **2020**, *20*, 321-334.

[3] J. Nam, S. Son, K. Park, W. Zou, L. D. Shea, J. J. Moon. Cancer nanomedicine for combination cancer immunotherapy. *Nat. Rev. Mater*. **2019**, *4*, 398-414.

[4] R. S. Riley, C. H. June, R. Langer, M.l J. Mitchell. Delivery technologies for cancer immunotherapy. *Nat. Rev. Drug Discov*. **2019**, *18*, 175-196.

[5] T. J. Anchordoquy, Y. Barenholz, D. Boraschi, M. Chorny, P. Decuzzi, M. A. Dobrovolskaia, Z. S. Farhangrazi, D. Farrell, A. Gabizon, H. Ghandehari, B. Godin, N. M. L. Beck, J. Ljubimova, S. M. Moghimi, L. Pagliaro, J. H. Park, D. Peer, E. Ruoslahti, N.J. Serkova, D. Simberg. Mechanisms and barriers in cancer nanomedicine: addressing challenges, looking for solutions. *ACS Nano* **2017**, *11*, 12-18.

[6] D. Rosenblum, N. Joshi, W. Tao, J. M. Karp, D. Peer. Progress and challenges towards targeted delivery of cancer therapeutics. *Nat. Commun*. **2018**, *9*, 1410.

[7] C.E. Meacham, S.J. Morrison. Tumour heterogeneity and cancer cell plasticity. *Nature* **2013**, *501*, 328-37.

[8] M. Fern´andez, F. Javaid, V. Chudasama. Advances in targeting the folate receptor in the treatment/imaging of cancers. *Chem. Sci*. **2017**, *9*, 790-810.

[9] M. Li, M. Li, Y. Yang, Y. Liu, H. Xie, Q. Yu, L. Tian, X Tang, K. Ren, J. Li, Z. Zhang, Q. He. Remodeling tumor immune microenvironment via targeted blockade of PI3K-γ and CSF-1/CSF-1R pathways in tumor associated macrophages for pancreatic cancer therapy. *J. Control. Release*. **2020**, *321*, 23-35.

[10] N. Zhang, S. Liu, S. Shi, Y. Chen, F. Xu, X. Wei, Y. Xu. Solubilization and delivery of Ursolic-acid for modulating tumor microenvironment and regulatory T cell activities in cancer immunotherapy. *J. Control. Release*. **2020**, *320*, 168-178.

[11] A. Trinh, K. Polyak. Tumor neoantigens: when too much of a good thing is bad. *Cancer Cell* **2019**, *36*, 466-467.

[12] W. N. Brennen, J. T. Isaacs, S. R. Denmeade. Rationale behind targeting fibroblast activation protein–expressing carcinoma-associated fibroblasts as a novel chemotherapeutic strategy. *Mol. Cancer Ther*. **2012**, *11*, 257-66.

[13] S. K. Wculek, F. J. Cueto, A. M. Mujal, I. Melero, M. F. Krummel, D. Sancho. Dendritic cells in cancer immunology and immunotherapy. *Nat. Rev. Immunol*. **2020**, *20*, 7-24.

[14] T. D. Wu, S. Madireddi, P. E. de Almeida, R. Banchereau, Y. J. J. Chen, A. S. Chitre, E. Y. Chiang, H. Iftikhar, W. E. O'Gorman, A. A. Yeung, C. Takahashi, L. D. Goldstein, C. Poon, S. Keerthivasan, D. E. de Almeida Nagata, X. Du, H. Lee, K.L. Banta, S. Mariathasan, M. D. Thakur, M. A. Huseni, M. Ballinger, I. Estay, P. Caplazi, Z. Modrusan, L. Delamarre, I. Mellman, R. Bourgon, J. L. Grogan. Peripheral T cell expansion predicts tumour infiltration and clinical response. *Nature* **2020**, *579*, 274-278.

[15] M. Kim, Y. Shon, J. Kim, Y. Oh. Selective activation of anticancer chemotherapy by cancer-associated fibroblasts in the tumor microenvironment. *J. Natl. Cancer Inst*. **2016**, *109*, 1-10.

[16] Q. Le, J. Suh, J. Choi, G. Park, J. Lee, G. Shim, Y. Oh. In situ nanoadjuvant-assembled tumor vaccine for preventing long-term recurrence. *ACS Nano* **2019**, *13*, 7442-7462.

[17] F. Zhang, N. N. Parayath, C. I. Ene, S. B. Stephan1, A. L. Koehne, M. E. Coon, E. C. Holland, M. T. Stephan. Genetic programming of macrophages to perform anti-tumor functions using targeted mRNA nanocarriers. *Nat. Commun*. **2019**, *10*, 3974.

[18] M. Binnewies, E. W. Roberts, K. Kersten, V. Chan, D. F. Fearon, M. Merad, L. M. Coussens, D. I. Gabrilovich, S. Rosenberg, C. C. Hedrick, R. H. Vonderheide, M. J. Pittet, R. K. Jain, W. Zou, T. K. Howcroft, E. C. Woodhouse, R. A. Weinberg, M. F. Krummel. Understanding the tumor immune microenvironment (TIME) for effective therapy. *Nat. Med*. **2018**, *24*, 541-550.

[19] D. S. Thommen, T. N. Schumacher. T cell dysfunction in cancer. *Cancer Cell* **2018**, *33*, 547-562.

[20] H. Li, K. Bullock, C. Gurjao, D. Braun, S. A. Shukla, D. Bossé, A. K. A. Lalani, S. Gopal, C. Jin, C. Horak, M. W. Rotolo, S. Signoretti, D. F. McDermott, G. J. Freeman, E. M. V. Allen, S. L. Schreiber, F. S. Hodi, W. R. Sellers, L. A. Garraway, C. B. Clish, T. K. Choueiri, M. Giannakis. Metabolomic adaptations and correlates of survival to immune checkpoint blockade. *Nat. Commun*. **2019**, *10*, 4346.

[21] Y. Zhang, R. Kurupati, L. Liu, X. Zhou, G. Zhang, A. Hudaihed, F. Filisio, W. G. Davis, X. Xu, G. C. Karakousis, L. M. Schuchter, W. Xu, R. Amaravadi, M. Xiao, N. Sadek, C. Krepler, M. Herlyn, G. J. Freeman, J. D. Rabinowitz, H. C. J. Ertl. Enhancing CD8+ T cell fatty acid catabolism within a metabolically challenging tumor

microenvironment increases the efficacy of melanoma immunotherapy. *Cancer Cell* **2017**, *32*, 377-391.

[22] D. Kim, Q. Le, Y. Kim, Y. Oh. Safety and photochemotherapeutic application of poly(γ-glutamicacid)-based biopolymeric nanoparticle. *Acta Pharm. Sin. B*. **2019**, *9*, 565-574.

[23] C. B. Rodell, S. P. Arlauckas, M. F. Cuccarese, C. S. Garris, R. Li, M. S. Ahmed, R.H. Kohler, M.J. Pittet, R. Weissleder, TLR7/8-agonist-loaded nanoparticles promote the polarization of tumour-associated macrophages to enhance cancer immunotherapy. *Nat. Biomed. Eng*. **2018**, *2*, 578-588.

[24] J. Song, S. S. Ardakani, T. So, M. Croft. The kinases aurora B and mTOR regulate the G1–S cell cycle progression of T lymphocytes. *Nat. Immunol*. **2007**, *8*, 64-74.

[25] P. S. Chowdhury, K. Chamoto, A. Kumar, T. Honjo. PPAR-induced fatty acid oxidation in T cells increases the number of tumor-reactive CD8$^+$ T Cells and facilitates anti–PD-1 therapy. *Cancer Immunol. Res*. **2018**, *6*, 1375-1387.

[26] S. A. Livesey, J. G. Linner. Cryofixation taking on a new look. *Nature* **1987**, *327*, 255-256.

[27] Y. Ma, S. Adjemian, S. R. Mattarollo, T. Yamazaki, L. Aymeric, H. Yang, J. Catani, D. Hannani, H. Duret, K. Steegh, I. Martins, F. Schlemmer, M. Michaud, O. Kepp, A. Q. Sukkurwala, S. L. Menger, E. Vacchelli, N. Droin, L. Galluzzi, R. Krzysiek, S. Gordon, P. R. Taylor, P. V. Endert, E. Solary, M. J. Smyth, L. Zitvogel, G. Kroemer. Anticancer chemotherapy-induced intratumoral recruitment and differentiation of antigen-presenting cells. *Immunity* **2013**, *38*, 729-41.

[28] S. R. Bonam, C. D. Partidos, S. K. M. Halmuthur, S. Muller. An overview of novel adjuvants designed for improving vaccine efficacy. *Trends Pharmacol. Sci*. **2017**, *38*, 771-793.

[29] K. Pouliot, R. B. Corbett, R. M. Roix, S. M. Paquette, K. West, S. Wang, S. Lu, E. Lien. Contribution of TLR4 and MyD88 for adjuvant monophosphoryl lipid A (MPLA) activity in a DNA prime–protein boost HIV-1 vaccine. *Vaccine* **2014**, *32*, 5049-56.

[30] T. A. Ajayeoba, S. Dula, O. A. Ijabadeniyi, Properties of Poly-γ-Glutamic Acid Producing- Bacillus Species Isolated from Ogi Liquor and Lemon- Ogi Liquor. *Front Microbiol*. **2019**, *10*, 771.

[31] S. Ko, J. Park, Y. Lee, D. Lee, R. B. Macgregor Jr., Y. Oh, Biochemical reprogramming of tumors for active modulation of receptor-mediated nanomaterial delivery. *Biomaterials* **2020**, *262*, 120343.

[32] X. Du, L. Xiong, S. Dai, S. Qiao, γ-PGA-Coated Mesoporous Silica Nanoparticles with Covalently Attached Prodrugs for Enhanced Cellular Uptake and Intracellular GSH-Responsive Release. *Adv. Healthc. Mater*. **2015**, *4*, 771-81.

[33] T. T. Smith, S. B. Stephan, H. F. Moffett1, L. E. McKnight, W. Ji, D. Reiman, E. Bonagofski, M. E. Wohlfahrt, S. P. S. Pillai, M. T. Stephan. In situ programming of leukaemia-specific T cells using synthetic DNA nanocarriers. *Nat. Nanotechnol*. **2017**, *12*, 813-820.

[34] D. Dong, L. Zheng, J. Lin, B. Zhang, Y. Zhu, N. Li, S. Xie, Y. Wang, N. Gao, Z. Huang. Structural basis of assembly of the human T cell receptor–CD3 complex. *Nature* **2019**, *573*, 546-552.

[35] M. Pawlak, P. Lefebvre, B. Staels. Molecular mechanism of PPARα action and its impact on lipid metabolism, inflammation and fibrosis in non-alcoholic fatty liver disease. *J. Hepatol*. **2015**, *62*, 720-33.

[36] G. Pascual, A. Avgustinova, S. Mejetta, M. Martín, A. Castellanos, C.S.O. Attolini, A. Berenguer, N. Prats, A. Toll, J. A. Hueto, C. Bescós, L. D. Croce, S. A. Benitah. Targeting metastasis-initiating cells through the fatty acid receptor CD36. *Nature* **2017**, *541*, 41-45.

[37] A. l'Hortet, K. Takeishi, J.Lepe, K. Morita, A. Achreja, B. Popovic, Y. Wang, K. Handa, A. Mittal, N. Meurs, Z. Zhu, F. Weinberg, M. Salomon, I. J. Fox, C. Deng, D. Nagrath, A. Gutierrez1. Generation of human fatty livers using custom-engineered induced pluripotent stem cells with modifiable SIRT1 metabolism. *Cell Metab*. **2019**, *30*, 385-401.

[38] T. Wang, Y. Cao, Q. Zheng, J. Tu, W. Zhou, J. He, J. Zhong, Y. Chen, J. Wang, R. Cai, Y. Zuo, B. Wei, Q. Fan, J. Yang, Y. Wu, J. Yi, D. Li, M. Liu, C. Wang, A. Zhou, Y. Li, X. Wu, W. Yang, Y.E. Chin, G. Chen, J. Cheng. SENP1-Sirt3 signaling controls mitochondrial protein acetylation and metabolism. *Mol. Cell* **2019**, *75*, 823-834.

[39] Z. Niu, Q. Shi, W. Zhang, Y. Shu, N. Yang, B. Chen, Q. Wang, X. Zhao, J. Chen, N. Cheng, X. Feng, Z. Hua, J. Ji, P. Shen. Caspase-1 cleaves PPARγ for potentiating the pro-tumor action of TAMs. *Nat. Commun*. **2017**, *8*, 766.

[40] H. Lee, X. Gao, M. I. Barrasa, H. Li, R. R. Elmes, L. L. Peters, H. F. Lodish. PPAR-α and glucocorticoid receptor synergize to promote erythroid progenitor self-renewal. *Nature* **2015**, *22*, 474-477.

[41] N. Xu, Q. Wang, S. Jiang, Q. Wang, W. Hu, S. Zhou, L. Zhao, L. Xie, J. Chen, A. Wellstein, E. Lai. Fenofibrate improves vascular endothelial function and contractility in diabetic mice. *Redox Biol*. **2019**, *20*, 87-97.

[42] M. Nakamura, T. Liu, S. Husain, P. Zhai, J. S. Warren, C. Hsu, T. Matsuda, C. J. Phiel, J. E. Cox, B. Tian, H. Li, J. Sadoshima. Glycogen synthase kinase-3a promotes fatty acid uptake and lipotoxic cardiomyopathy. *Cell Metab*. **2019**, *29*, 1119-1134.

[43] Y. Shen, Y. Su, F. J. Silva, A. H. Weller, J. S. Colo´n, P. M. Titchenell, D. J. Steger, P. Seale, R. E. Soccio. Shared PPARα target genes regulate brown adipocyte thermogenic function. *Cell Rep*. **2020**, *30*, 3079-3091.

[44] P. J. Siska, K. E. Beckermann, F. M. Mason, G. Andrejeva, A. R. Greenplate, A. B. Sendor, Y. J. Chiang, A. L. Corona, L. F. Gemta, B.G. Vincent, R. C. Wang, B. Kim, J. Hong, C. Chen, T. N. Bullock, J. M. Irish, W. K. Rathmell, J. C. Rathmell. Mitochondrial dysregulation and glycolytic insufficiency functionally impair CD8 T cells infiltrating human renal cell carcinoma. *JCI Insight*. **2017**, *2*, 93411.

[45] H. G Sprenger, T. Langer. The Good and the bad of mitochondrial breakups. *Trends Cell Biol*. **2019**, *29*, 888-900.

[46] G. J. van der Windt, D. O'Sullivan, B. Everts, S. C.-C. Huang, M. D. Buck, J. D. Curtis, C. Chang, A. M. Smith, T. Aia, B. Faubert, R. G. Jones, E. J. Pearce, E. L. Pearce. CD8 memory T cells have a bioenergetic advantage that underlies their rapid recall ability. *Proc. Natl. Acad. Sci. USA*. **2013**, *110*, 14336-41.

[47] M. L. Balmer, E. H. Ma, G. R. Bantug, J. Gra¨hlert, S. Pfister, T. Glatter, A. Jauch, S. Dimeloe, E. Slack, P. Dehio, M. A. Krzyzaniak, C. G. King, A. V. Burgener, M. Fischer, L. Develioglu, R. Belle, M. Recher, W. V. Bonilla, A. J. Macpherson, S. Hapfelmeier, R. G. Jones, C. Hess. Memory CD8+ T Cells require increased concentrations of acetate induced by stress for optimal function. *Immunity* **2016**, *44*, 1312-24.

[48] A. Angelin, L. Gil-de-Go´ mez, S. Dahiya, J. Jiao, L. Guo, M. H. Levine, Z. Wang, W. J. Quinn III, P. K. Kopinski, L. Wang, T. Akimova, Y. Liu, T. R. Bhatti, R. Han, B. L. Laskin, J. A. Baur, I. A. Blair, D. C. Wallace, W. W. Hancock, U. H. Beier. Foxp3 reprograms T cell metabolism to function in low-glucose, high-lactate environments. *Cell Metab*. **2017**, *25*, 1282-1293.

[49] V. A. Gerriets, R. J. Kishton, M.O. Johnson, S. Cohen, P.J. Siska, A.G. Nichols, M.O. Warmoes, A. A. Cubas, N. J. MacIver, J. W. Locasale, L. A. Turka, A. D. Wells, J. C. Rathmell. Foxp3 and Toll-like receptor signaling balance T_{reg} cell anabolic metabolism for suppression. *Nat. Immunol*. **2016**, *17*, 1459-1466.

[50] S. J. Patel, N. E. Sanjana, R. J. Kishton, A. Eidizadeh, S. K. Vodnala, M. Cam, J. J. Gartne, L. Jia, S. M. Steinberg, T. N. Yamamoto, A. S. Merchant, G. U. Mehta, A. Chichura, O. Shalem, E. Tran, R. Eil, M. Sukumar, E. P. Guijarro, C. Day, P. Robbins, S. Feldman, G. Merlino, F. Zhang, N. P. Restifo. Identification of essential genes for cancer immunotherapy. *Nature* **2017**, *548*, 537-542.

[51] S. Rafiq, C. S. Hackett, R. J. Brentjens. Engineering strategies to overcome the current roadblocks in CAR T cell therapy. *Nat. Rev. Clin. Oncol*. **2020**, *17*, 147-167.

Chapter 3

Lipid nanoparticle-mediated lymphatic delivery of immunostimulatory nucleic acids

Chapter 3. Lipid nanoparticle-mediated lymphatic delivery of immunostimulatory nucleic acids

3.1. Introduction

A vaccine adjuvant, which is an immunostimulatory component of a vaccine formulation, is often very important for the successful vaccination of an antigen [1–3]. Most recently developed vaccines do not apply the entire pathogen but rather use certain components (e.g., major proteins) as antigens [4]. However, a subunit vaccine alone often fails to induce a strong immune response [5]. Aluminum-containing adjuvants have the longest history of use [6,7], but they have a limited ability to induce cellular immunity and thus are not suitable for intracellular antigen applications [8]. In addition, aluminum adjuvants can have some side effects, raising safety issues [6,9]. Since preventive vaccines are used in people of various ages, safety is a top priority in vaccine development.

Adjuvants composed of nucleic acids have great advantages in terms of biocompatibility and safety [8]. The Toll-like receptor 9-agonizing nucleic acid, CpG 1018, is included as an adjuvant in the hepatitis B vaccine, HEPLISAV-B®, which was recently approved by the U.S. FDA [10]. Although this supported the efficacy of nucleic acid adjuvants, the pharmaceutical application of nucleic acids has faced some limitations. For example, many nucleic acid adjuvants target intracellular molecules in immune-stimulating pathways and thus must be introduced into dendritic cells (DC) [8]. In addition, nucleic acids have weak stability due to the action of in vivo nucleases [11]. To compensate for these limitations, nucleic acid adjuvants may need to be applied using an appropriately designed delivery system.

Lipid nanoparticles (LNP), which represent such a drug delivery system, have recently attracted attention as an antigen delivery strategy [1,12,13]. LNP hold great promise in customized medicine because their manufacturing process is relatively simple and desirable properties (charge, size, surface modification, etc.) can be easily imparted by altering the composition of lipids [14,15]. It may also be possible to impart a synergistic effect by simultaneously loading an antigen and adjuvant to the LNP. In the BioNTech/Pfizer and Moderna mRNA vaccines recently approved for the prevention of coronavirus infectious disease-19 (COVID-19), LNP comprises a major component and are thought to play roles both in mRNA delivery and as an adjuvant [1].

Here, an LNP was developed to target DC for lymphatic delivery of nucleic acid adjuvants. Polyinosinic : polycytidylic acid (poly I:C, PIC) was selected as a model nucleic acid adjuvant. The LNP was designed to carry a cationic charge to enable the delivery of the negatively charged nucleic acid adjuvant, and mannose-modified lipid was inserted to induce DC-specific delivery. The effects of PIC-complexed mannose LNP (PIC/M-NP) on DC-

specific cellular uptake and DC maturation were evaluated in vitro and in vivo (Figure 1).
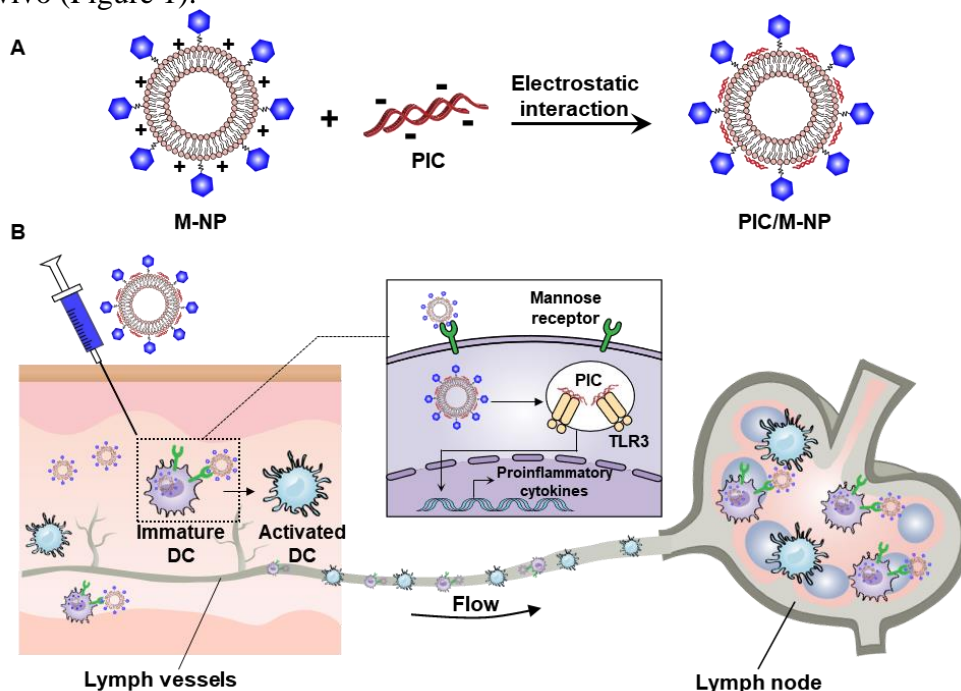
Figure 1. Dendritic cell (DC)-mediated lymph node targeting by polyinosinic:polycytidylic acid (PIC)/mannose-modified cationic lipid nanoparticle (M-NP). A) PIC was complexed with M-NP via electrostatic interaction to form PIC/M-NP. B) Mechanisms of DC activation and lymph node targeting by PIC/M-NP.

3.2. Material and Method
3.2.1. Preparation of PIC-Loaded M-NP

M-NP were prepared using a thin-film hydration method [16]. Briefly, 0.292 μmol of 1,2-diphytanoyl-sn-glycero-3-phosphoethanolamine (DPhPE, Avanti Polar Lipids, Alabaster, AL, USA), 0.464 μmol of 3β-[*N*-(*N'*,*N'*-dimethylaminoethane)-carbamoyl]cholesterol (DC-Chol, Avanti Polar Lipids), 1.24 μmol of 1,2-dioleoyl-sn-glycero-3-ethylphosphocholine (EDOPC, Avanti Polar Lipids), and various moles of 1,2-dipalmitoyl-sn-glycero-3-phospho((ethyl-1',2',3'-triazole)triethyleneglycolmannose) (PA-PEG3-man-nose, PEG m.w., 148.1, Avanti Polar Lipids) were dissolved in chloroform. For flow cytometry and fluorescence microscopy, 0.03 μmol fluorescent dye cyanine 5-labeled 1,2-dioleoyl-sn-glycero-3-phosphoethanolamine-*N* (Cy5-PE, Avanti Polar Lipids) was added to the lipid mixture. The chloroform was removed, and the remaining liquid was dehydrated to a thin lipid film using a vacuum rotary evaporator. The lipid film was rehydrated with 1 mL of 20 mM 4-(2-hydroxyethyl)-1-piperazineethanesulfonic acid buffer (HEPES, pH 7.0), followed by sonication for 30 min and centrifugation at $13,500 \times g$ for 3 min. The

supernatant was collected as M-NP. Various PA-PEG-mannose (0.04, 0.1, 0.2, or 0.4 μmol) were used to make M-NPs containing 2, 5, 10, 20 mol% mannose and described as M-NP 2, 5, 10, and 20, respectively. For the preparation of poly I:C-loaded M-NP (PIC/M-NP), 5 μg of poly I:C (average size of 0.6 kb, InvivoGen, San Diego, CA, USA) in HEPES buffer was added into 20 μL of M-NP, vortex mixing was used to form PIC/M-NP complexes via electrostatic interaction, and incubation was performed for 10 min at room temperature.

3.2.2. Characterization and Complexation Study of Nanoparticles

Nanoparticles were characterized by morphology, size, and net surface charge. The morphology of nanoparticles was measured by transmission electron microscopy (TEM) using a JEM-2100 F (JEOL, Tokyo, Japan). The size distribution and zeta potential were evaluated using an ELSZ-1000 instrument (Otsuka Electronics Co., Osaka, Japan), based on the dynamic light scattering method and laser Doppler microelectrophoresis, respectively. For size measurement, various M-NP and PIC/M-NP samples stored at 4 °C were diluted 20 mM HEPES buffer. The particle size was obtained by cumulant intensity distribution, and size was measured 3 times for each group. The particle size was measured over 1 week. The complexation of PIC and M-NP was analyzed by gel retardation assay [8]. PIC/M-NP were prepared by mixing PIC with M-NP at various weight ratios, followed by 1% agarose gel electrophoresis and analysis using a Gel Doc XR+ Imaging System (Bio-Rad, Hercules, CA, USA).

3.2.3. Animals

Five-week-old Balb/c mice were purchased from Raon Bio Korea (Yongin, Korea) and maintained under standard pathogen-free conditions. All animal experiments were performed under the Guidelines for the Care and Use of Laboratory Animals of the Institute of Laboratory Animal Resources, Seoul National University (approval number, SNU-190417-15(E)).

3.2.4. Isolation of Bone Marrow-Derived Dendritic Cells (BMDC)

BMDC were isolated as previously described [17]. Briefly, femurs and tibias were extracted from 5-week-old Balb/c mice and sterilized by immersion in 70% ethanol for 5 min. The bones were washed thrice with phosphate-buffered saline (PBS; pH 7.4), bone marrow was flushed with complete RPMI medium (Welgene, Gyeongsan, Korea), and red blood cells were lysed. The collected monocytes were resuspended in Iscove's modified Dulbecco's medium (Welgene) supplemented with 10% fetal bovine serum (GenDEPOT, Barker, TX, USA), 100 mg/mL streptomycin, 100 units/mL penicillin (Gibco, Carlsbad, CA, USA), 20 ng/mL recombinant mouse granulocyte-macrophage colony-stimulation factor (GenScript, Piscataway, NJ, USA), 20 ng/mL recombinant mouse interlukin-4 (GenScript) and 50

μm β-mercaptoethanol (Sigma-Aldrich). Fresh medium was added on day 3 and BMDC were ready to use on day 7.

3.2.5. In Vitro Cytotoxicity Assay

The cell viability of nanoparticle-treated BMDC was evaluated by MTT (3-(4,5-dimethylthizol-2-yl)-2,5-diphenyltetrazolium bromide) assay (Sigma-Aldrich) and live cell staining [18]. BMDC were seeded to 24-well plates (1×10^5 cells/well) and incubated for 24 h. BMDC was treated with various nanoparticle formulations at a PIC dose of 5 μg for 4 h. The medium was changed with fresh RPMI medium, and cells were incubated for 24 or 48 h and then treated with MTT (250 μg/mL) for 1 h at 37 °C. The formazan crystals in the cells were solubilized with dimethyl sulfoxide (Sigma-Aldrich), and the absorbance of the colored solution was measured using a Multi-Reader (Molecular Devices, San Jose, CA, USA) at 570 nm. The cell viability of BMDC was calculated by normalizing the absorbance of the untreated BMDC group to 100%. For live cell staining, BMDC were stained with 2 μM calcein AM (Molecular Probes, Eugene, OR, USA) for 15 min, and live BMDC was observed by a fluorescence microscope (DM IL; Leica, Buffalo Grove, IL, USA).

3.2.6. In Vitro Study of DC Targeting

The DC-targeted delivery efficiency of nanoparticles was evaluated by flow cytometry and fluorescence microscopy. For flow cytometry, BMDC were seeded in 24-well plates (1×10^5 cells/well), incubated for 24 h, and treated with Cy5-labeled nanoparticles at a PIC dose of 5 μg for 4 h. The cells were harvested, washed thrice with PBS, and analyzed by flow cytometry (FACSCalibur; BD Bioscience, San Jose, CA, USA). For fluorescence microscopy, BMDC were treated with Cy5-labeled nanoparticles for 4 h, washed with PBS, and fixed with 4% formaldehyde in PBS for 10 min. The cells were then washed with PBS, stained with FITC-anti-mouse CD11c antibody (BioLegend, San Diego, CA, USA) for 1 h, and then stained with 4′,6-diamidino-2-phenylindole (DAPI, Sigma-Aldrich, St. Louis, MO, USA) for 10 min. DC-targeting images were visualized using a confocal laser-scanning microscope (LSM 5 Exciter; Carl Zeiss, Inc., Jena, Germany).

3.2.7. In Vitro Study of DC Maturation

DC maturation was evaluated by analyzing the expression level of CD86 on the cell surface [19]. BMDC were seeded in 24-well plates (1×10^5 cells/well), incubated for 24 h, and treated with various nanoparticle formulations at a PIC dose of 5 μg for 24 h. The cells were harvested and stained with FITC-anti-mouse CD11c and APC-anti-mouse CD86 (BioLegend) antibodies for 1 h. For CD11c analysis, the excitation and emission wavelengths used for flow cytometry of FITC were 495 and 519 nm, respectively. For CD86 analysis, the excitation and emission

wavelengths used for flow cytometry of APC were 650 and 660 nm, respectively. The expression of CD86 was analyzed using a BD FACSCalibur flow cytometer (BD Bioscience). The expression of surface markers on DC was determined by gating the CD11c$^+$ population.

3.2.8. In Vivo Lymph Node Targeting of Nanoparticles

The in vivo lymph node targeting ability of nanoparticles was evaluated by flow cytometry and molecular imaging. Five-week-old Balb/c mice were injected subcutaneously with PIC/Cy5-labeled M-NP at a PIC dose of 0.25 mg/kg. For lymph node imaging, mice were sacrificed after 24 h and inguinal lymph nodes were extracted. The fluorescence of lymph nodes was monitored using an IVIS Spectrum In Vivo Imaging System (PerkinElmer, Waltham, MA, USA). For flow cytometry, single cells were prepared by grinding lymph nodes through 70 µM cell strainers (SPL Life Science, Pocheon, Korea) and stained with FITC-anti-mouse CD11c for 1 h. The population of DC that took up nanoparticles (CD11c$^+$Cy5$^+$) in the lymph nodes was measured by flow cytometry.

3.2.9. DC Maturation Study in Lymph Node

DC maturation in lymph nodes was analyzed by measuring the expression level of CD86 on DC isolated from Balb/c mice. Five-week-old Balb/c mice were injected subcutaneously in the back with various PIC-loaded nanoparticle formulations at a PIC dose of 0.25 mg/kg (5 µg PIC/mouse). After 48 h, mice were sacrificed and inguinal lymph nodes were isolated. Single-cell suspensions were stained with FITC-anti-mouse CD11c and APC-anti-mouse CD86 for 1 h. The population of activated DC (CD11c$^+$CD86$^+$) was analyzed by flow cytometry.

3.2.10. In Vivo Toxicity Study

Five-week-old Balb/c were injected subcutaneously in the back with various PIC-loaded nanoparticle formulations. Seven days after injection, whole blood and serum were collected for analysis of biochemical markers of organ functions. As a biomarker of liver function, alanine aminotransferase (ALT) level in the blood was measured. As a biomarker of kidney function, blood urea nitrogen (BUN) level in the blood was measured.

3.2.11. Statistics

Data were shown as mean ± standard error of the mean (SEM). The sample size (*n*) for each statistical analysis was indicated in the figure legends. A one-way analysis of variance (ANOVA) with the Student−Newman−Keuls post-hoc test was used to analyze statistical differences. The SigmaStat software (version 12.0; Systat Software, Richmond, CA, USA) was used for all statistical analysis. Significant differences are indicated as ***p<0.001*,* **p<0.01*,* and *p<0.05.

3.3. Results
3.3.1. Characterization of PIC/M-NP

The physicochemical features of poly IC/M-NP were characterized with respect to morphology, size, zeta potential, and poly IC loading capacity. TEM image revealed homogenous and round morphology of PIC/M-NP 10 (Figure 2A). In size, the M-NP measured around 150 nm in diameter regardless of the mannose-PEG lipid content (Figure 2B). No significant size change was observed after lipoplex formation with PIC. The particle size of PIC/M-NP 10 was 157.7 ± 14.4 nm. Due to the cationic lipid component, the M-NP showed a strong cationic surface charge higher than 60 mV (Figure 2C). When the cationic M-NP complexed with negatively charged poly I:C, the zeta potential decreased significantly; the zeta potential of PIC/M-NP 10 was 18.1 ± 4.2 mV. The loading capacity of poly I:C on M-NP was confirmed by gel retardation. When poly IC was complexed with M-NP at various w/w ratios, complete loading was observed at a w/w ratio of 10 (Figure 2D).
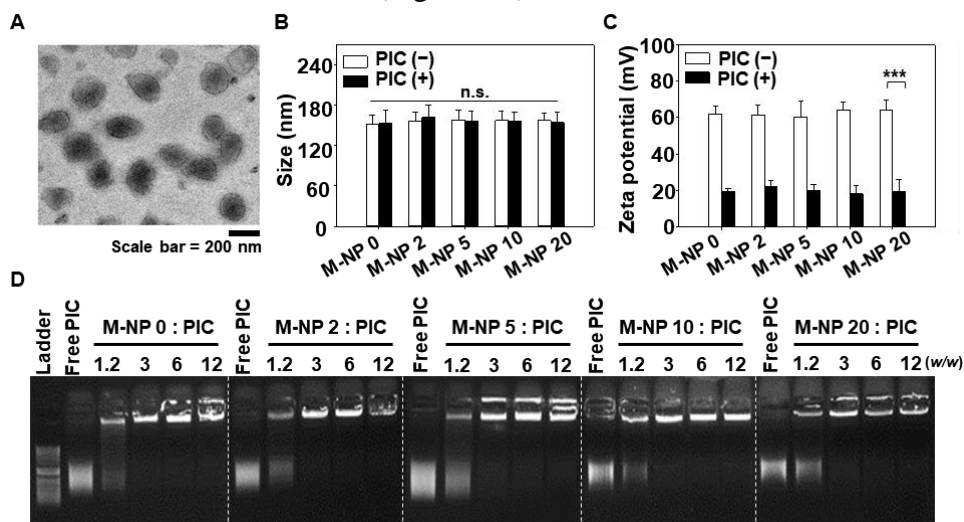
Figure 2. Characterization of PIC/M-NP. A) Morphology of polyIC/M-NP 10 was observed by TEM. B) Mean particle sizes of nanoparticles in a naked form or PIC-complexed form were measured by dynamic light scattering ($n = 3$, one-way ANOVA and Student-Newman-Keuls test). C) Zeta potential was measured by laser Doppler microelectrophoresis ($n = 3$, one-way ANOVA and Student-Newman-Keuls test). D) Complexation between poly IC and M-NP was determined by gel retardation. (***$p<0.001$, n.s.: not significantly different).

3.3.2. Cytotoxicity of PIC/M-NP

The poly IC/M-NP did not induce significant toxicity to BMDC. When various mannose-PEG lipid contents of PIC/M-NP were applied and cells were incubated for 24 and 48 h, no notable change was observed in live cell density (Figure 3A). Consistently, the cell viability calculated by MTT assay did not significantly differ between BMDC treated with or without PIC/M-

NP for 24 or 48 h (Figure 3B).
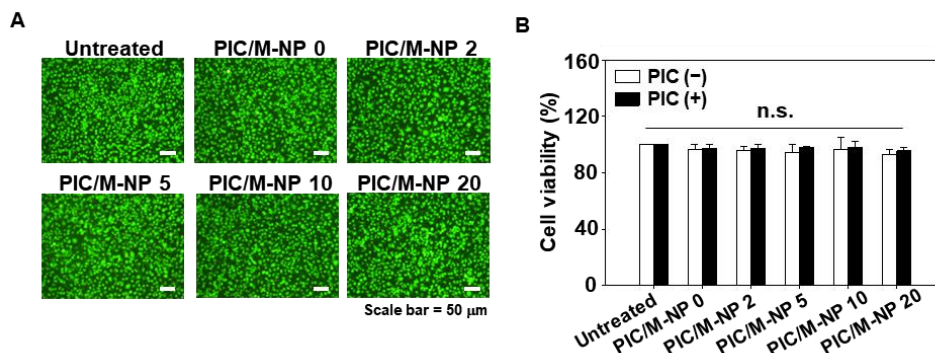
Figure 3. PIC/M-NP cytotoxicity on bone marrow-derived dendritic cells (BMDC). BMDC were treated with nanoparticles in a naked form or PIC-complexed form. After 24 h and 48 h, the viability of BMDC was visualized by live cell staining (A) and quantified by MTT assay (B) ($n = 5$, one-way ANOVA and Student-Newman-Keuls test). Scale bar: 50 μm. (n.s.: not significantly different).

3.3.3. Cellular Uptake of PIC/M-NP

The finely controlled nanoformulation significantly improved the cellular uptake of PIC/M-NP in BMDC. As the content of mannose-PEG-lipid increased, thus did the cellular uptake of PIC/M-NP (Figure 4A). In particular, the use of 10% mannose-PEG-lipid significantly enhanced the cellular uptake, with this group showing 1.90-fold and 1.20-fold higher mean fluorescence intensity compared to those of the PIC/M-NP 0- and PIC/M-NP 5-treated groups. However, when the content of mannose-PEG-lipid was further increased to 20%, the cellular uptake was 9.35-fold lower than that obtained with PIC/M-NP 10. Consistently, confocal microscopic images revealed distinct endosomal localization of M-NP fluorescence in BMDC treated with PIC/M-NP 10, whereas this was not seen for the untreated group or those treated with PIC/M-NP of other ratios (Figure 4B).
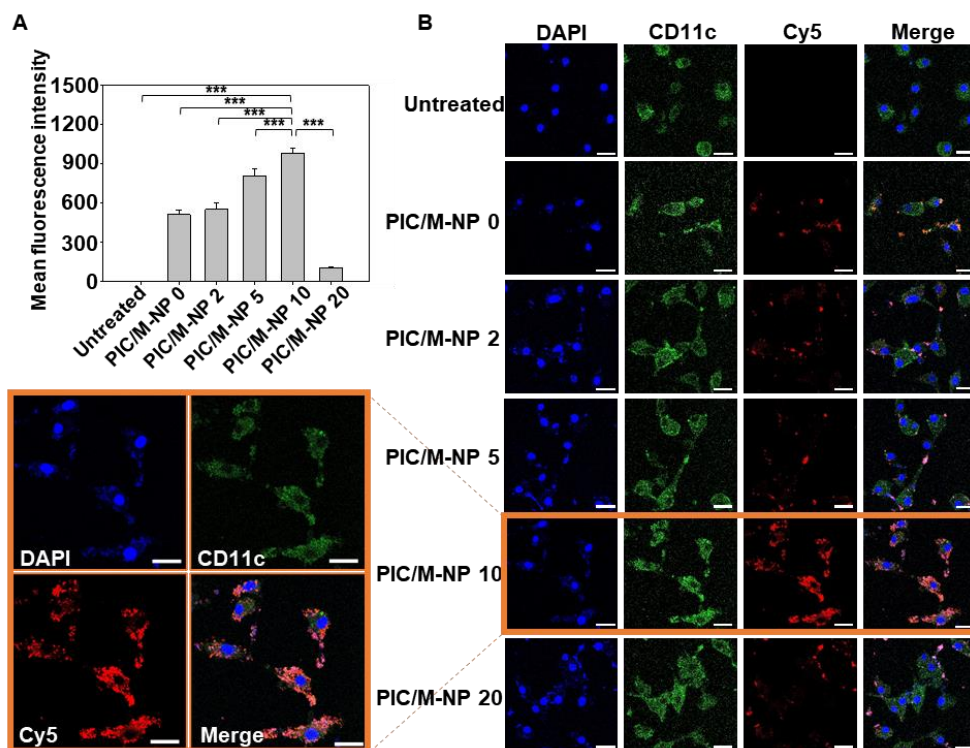
Figure 4. Intracellular uptake of PIC/M-NP by BMDC. BMDC were treated with PIC/M-NP with mannose densities (0 to 10%) for 4 h. A) Intracellular uptake of PIC/M-NP was measured by flow cytometry (A). ($n = 5$, one-way ANOVA and Student-Newman-Keuls test). B) Intracellular locations were visualized by confocal microscopy. Scale bar: 20 μm. (***$p < 0.001$).

3.3.4. In Vitro BMDC Maturation Effect of PIC/M-NP

Poly IC-loaded M-NP 10 remarkably enhanced BMDC maturation. When BMDC were treated with M-NP lacking PIC, there was no significant expression of the DC maturation marker, CD86 (Figure 5A). Similarly, free PIC treatment did not show significant increase in the maturation of BMDC. However, PIC/M-NP 10-treated BMDC showed a CD86-positive DC population of $40.7 \pm 1.2\%$; this was significantly higher than the $13.9 \pm 1.9\%$ seen in the untreated group, indicating that PIC/M-NP 10 significantly promoted DC maturation (Figure 5B). BMDC treated with PIC/M-NP 0, which lacked the mannose-PEG-lipid, had a $26.1 \pm 1.9\%$ CD86-positive DC population, indicating that this formulation triggered DC maturation but did so less efficiently than PIC/M-NP 10.
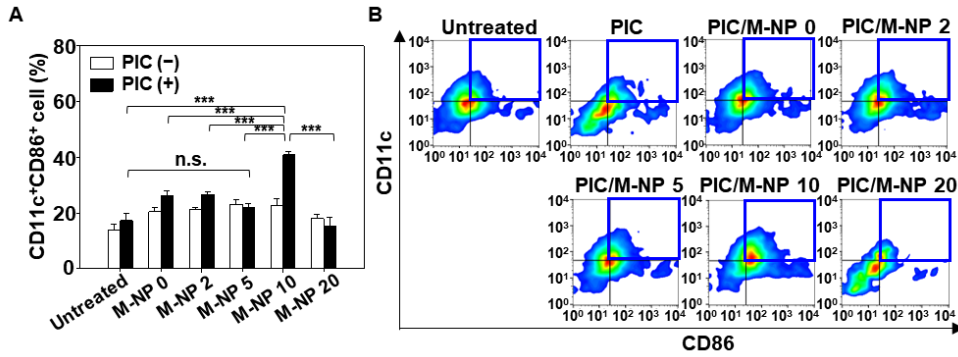
Figure 5. In vitro activation of BMDC by PIC/M-NP. BMDC was treated with various PIC-loaded nanoparticles. After 48 h, the expression of CD86 on BMDC was quantified by flow cytometry. A) Populations of $CD11c^+CD86^+$ cells are shown for each group ($n = 5$, one-way ANOVA and Student-Newman-Keuls test). B) A representative cell density plot is shown for each group. (***$p<0.001$). Blue boxes indicate the gated areas for $CD11c^+CD86^+$ cells.

3.3.5. In Vivo Lymph Node Targeting of PIC/M-NP

Administered PIC/M-NP exhibited greater accumulation in lymph nodes compared to the untreated group. One day after subcutaneous injection of the nanoparticle to the backs of mice, whole-body imaging revealed that mice treated with PIC/M-NP 0, poly IC/M-NP 5, or PIC/M-NP 20 showed low-intensity fluorescence signals in their inguinal lymph nodes (Figure 6A). On the other hand, higher fluorescence signal fluorescence was detected in the lymph nodes of mice treated with PIC/M-NP 10. Ex vivo images of extracted inguinal lymph nodes also showed increased PIC/M-NP 10-derived fluorescence localized in the lymph nodes (Figure 6B). The radiant efficiency calculated for the lymph nodes of the PIC/M-NP 10-treated group was 2.40-fold and 2.03-fold higher than those of the PIC/M-NP 0- and PIC/M-NP 5-treated groups, respectively (Figure 6C). Cellular uptake of PIC/M-NP was observed in the DC population of lymph nodes. The PIC/M-NP 10-treated group showed the highest DC population compared to other groups (Figure 6D), and its fluorescence positive DC population was 5.7 ± 1.0%, which was 25.7-fold higher than that seen in the PIC/M-NP 0-treated group (Figure 6E).
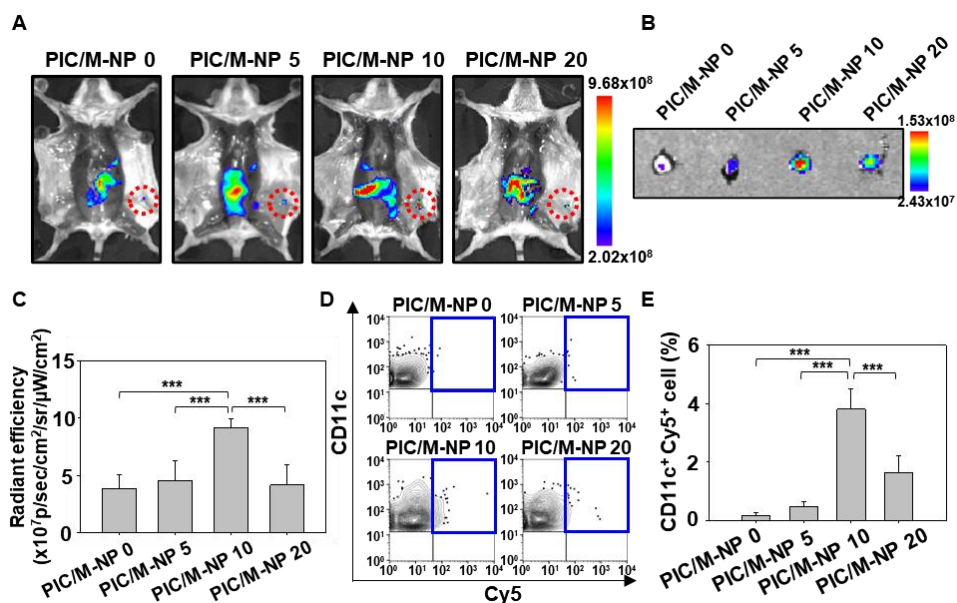
Figure 6. In vivo lymph node-targeting ability of PIC/M-NP. Mice were injected subcutaneously with Cy5-labeled nanoparticles. After 24 h, fluorescence at inguinal lymph node sites (A) and ex vivo images of inguinal lymph nodes (B) were visualized. C) Radiant efficiency of inguinal lymph nodes was quantified for each group ($n = 5$, one-way ANOVA and Student-Newman-Keuls test). D) The uptake of nanoparticles in lymph node-resident DC was measured by flow cytometry. Populations of CD11c$^+$Cy5$^+$ cells (E) are shown ($n = 5$, one-way ANOVA and Student-Newman-Keuls test, ***$p<0.001$).

3.3.6. In Vivo DC Maturation Effect

Consistent with the enhanced cellular uptake of PIC/M-NP 10 into DC of the lymph nodes, injection of PIC/M-NP 10 into mice induced significant DC maturation, as determined by the expression of CD86. Two days after subcutaneous injection of PIC/M-NP, the CD86-positive DC population in the inguinal lymph node was analyzed. CD86-positive populations of mice were 26.7 ± 3.4% for PIC/M-NP 0-treated group, and 21.7 ± 2.6% for M-NP 10-treated group (Figure 7A). There were no significant differences in CD86-positive populations of mice between untreated (Figure 7B) and M-NP 10-treated groups. In contrast, PIC/M-NP 10 treatment efficiently induced DC maturation, yielding a positive population of 42.8 ± 3.5%, which was 1.58-fold and 1.60-fold higher than those seen in the untreated and poly IC/M-NP 0-treated groups, respectively.
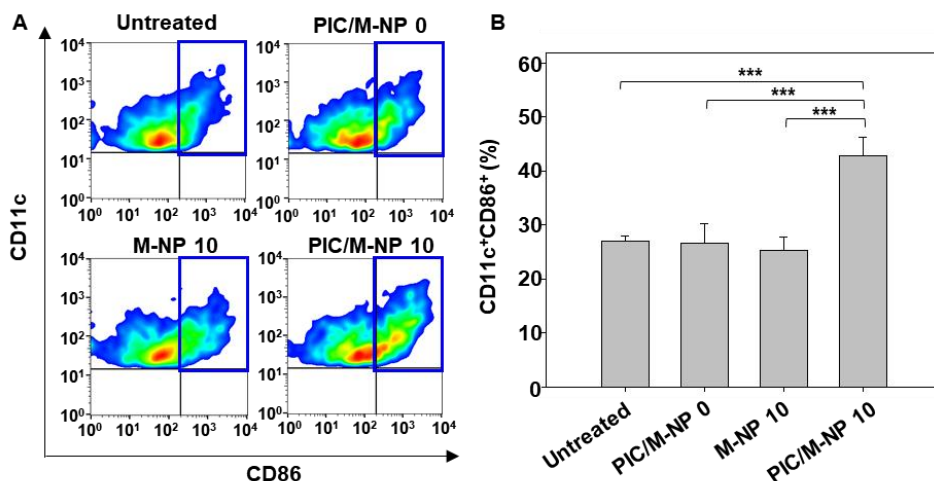
Figure 7. In vivo DC maturation in inguinal lymph nodes. Mice were injected subcutaneously with nanoparticles in a naked form or PIC-complexed form at a poly IC dose of 0.25 mg/kg. A) After 48 h, inguinal lymph nodes were isolated, and the expression level of CD86 was measured by flow cytometry. The blue box indicates the gated area for CD11c⁺CD86⁺ cells. B) Population of CD11c⁺CD86⁺ cells was quantified for each group (n = 5, one-way ANOVA and Student-Newman-Keuls test, ***$p<0.001$).

3.4. Discussion

In this study, PIC-loaded mannose conjugated nanoparticles, called PIC/M-NP, were developed to efficiently target lymph nodes and induce immune system activation. PIC/M-NP 10, which contains an optimized 10% molar ratio of mannose-PEG-lipid in the nanoparticle, demonstrated the most efficient lymph node targeting and cellular uptake into DC, which in turn led to DC maturation by PIC.

M-NP 10 served as a suitable delivery system for introducing PIC to DC. As a synthetic analog of double-stranded RNA, poly IC is a potent immune adjuvant that can activate the innate immune system [20]. Since its receptor, Toll-like receptor 3, is mainly localized to the endosomal compartment, the PIC needs to enter the cellular endosomal pathway to be recognized [21]. However, the high molecular weight and highly negative charge of PIC hinder its penetration of the plasma membrane. Previously, PIC has been delivered using various cationic materials such as polysaccharide [22], polymer [23], and lipid [24] nanoparticles. In these studies, cationic net charges per se have not shown to induce the non-specific uptake of PIC to the lymph nodes, indicating the need for specific ligands in the design of delivery systems. In this study, the modification with mannose moieties suggested the potential of improved targeting to the lymph nodes.

In this regard, targeting mannose receptors with M-NP 10 can be an efficient strategy for delivering PIC to DC. The mannose receptor, also called CD206, is known to be overexpressed on immature DC and induce

endocytosis [25]. As the major role of mannose receptors in DC is to induce internalization of pathogens by recognizing their glycans or mannosylated antigens, targeting of mannose receptors is an efficient way to deliver therapeutic agents to immune cells. [26,27]. M-NP 10 is less than 200 nm in size and thus should be suitable for receptor-mediated endocytosis (Figure 2A) [28]. The ability to load poly IC on the surface of M-NP 10 through charge-charge interaction further supports the promise of M-NP 10 as a potent delivery system for activating the immune system (Figure 2C).

It has been reported that excessive PEGylated lipids in liposomes can provide steric hindrance and reduce the efficiency of surface targeting moieties to bind to the target cells [29]. Such phenomenon was termed as 'PEG dilemma'. To avoid the PEG dilemma, the optimization of pegylated lipid density in lipid nanoparticles would be essential. In this study, triethyleneglycol mannose derivative of lipid was used. In a previous study, di-, tetra, or hexaethylenglycol have been used to formulate mannosylated lipid nanoparticles. In the study, tetraethyleneglycol was observed to provide higher uptake by Raw 264.7 cells than diethyleneglycol or hexaethyleneglycol-based nanoparticles [30]. This study suggests the importance of PEG molecular weights in the design of nanoparticles.

The significant accumulation of signal in inguinal lymph nodes of mice subcutaneously injected with PIC/M-NP 10 indicates that the PIC/M-NP 10-internalizing DC migrated to the lymph node, where a systemic adaptive immune response can be initiated (Figure 6). Cationic nanoparticles have been reported to be taken up by macrophages in the lung, liver, and spleen [31]. A previous study reported that subcutaneous injection of nanoparticles could reduce the distribution to the liver or spleen and increase lymph node delivery compared to intravenous injection [32]. Although the results showed that the fluorescence signals in the liver and spleen after subcutaneous injection of PIC/M-NP, biochemical markers related to liver and spleen functions remain in normal ranges (Figure 8). The uptake of PIC to DC supported their maturation and efficient migration and achieved cell-mediated lymph node targeting. As a result, significantly more activated DC were found in the lymph nodes of PIC/M-NP 10-treated mice compared to control mice and those treated with the other formulations.

The capability of PIC/M-NP 10 to efficiently target and move antigen-presenting cells to the lymph node suggest that this formulation could be a promising vaccine delivery system. As DC critically links the innate and adaptive immune systems and the lymph node is an immune-specialized organ where T and B lymphocytes are concentrated, PIC/M-NP 10 has the potential to induce profound adaptive immune responses against infectious disease or cancers.

3.5. Conclusion

In conclusion, this research shows that the developed PIC-loaded mannose conjugated nanoparticles, called PIC/M-NP, could efficiently target

lymph nodes and induce immune system activation. PIC/M-NP 10, which contains an optimized 10% molar ratio of mannose-PEG-lipid in the nanoparticle, demonstrated the most efficient lymph node targeting and cellular uptake into DC, which in turn led to DC maturation by PIC. The capability of PIC/M-NP 10 to efficiently target and move antigen-presenting cells to the lymph node suggest that this formulation could be a promising vaccine delivery system. As DC critically links the innate and adaptive immune systems and the lymph node is an immune-specialized organ where T and B lymphocytes are concentrated, PIC/M-NP 10 has the potential to induce profound adaptive immune responses against infectious disease or cancers.

3.6. Reference

[1]   Y. H. Chung, V. Beiss, S. N. Fiering, N. F. Steinmetz. Covid-19 vaccine frontrunners and their nanotechnology design. *ACS Nano* **2020**, *14*, 12522–12537.

[2]   G. Anderluzzi, S. T. Schmidt, R. Cunliffe, S. Woods, C. W. Roberts, D. Veggi,. Ferlenghi, D. T. O'Hagan, B. C. Baudner, Y. Perrie. Rational design of adjuvants for subunit vaccines: The format of cationic adjuvants affects the induction of antigen-specific antibody responses. *J. Control. Release* **2020**, *330*, 933-944.

[3]   R. Bastola, S. Lee. Physicochemical properties of particulate vaccine adjuvants: Their pivotal role in modulating immune responses. *J. Pharm. Investig.* **2019**, *49*, 279–285.

[4]   Q. V. Le, J. Choi, Y. K. Oh. Nano delivery systems and cancer immunotherapy. *J. Pharm. Investig.* **2018**, *48*, 527–539.

[5]   D. S. S. M. Uppu, M. E. Turvey, A. R. M. Sharif, K. Bidet, Y. He, V. Ho, A. D. Tambe, J. Lescar, E. Y. Tan, K. Fink, J. Chen, P. T. Hammond. Temporal release of a three-component protein subunit vaccine from polymer multilayers. *J. Control. Release* **2020**, *317*, 130–141.

[6]   N. Principi, S. Esposito. Aluminum in vaccines: Does it create a safety problem? *Vaccine* **2018**, *36*, 5825–5831.

[7]   Y. Hou, Y. Wang, Y. Tang, Z. Zhou, L. Tan, T. Gong, L. Zhang, X. Sun. Co-delivery of antigen and dual adjuvants by aluminum hydroxide nanoparticles for enhanced immune responses. *J. Control. Release* **2020**, *326*, 120–130.

[8]   J. J. Choi, Q. V. Le, D. Kim, Y. B. Kim, G. Shim, Y. K. Oh. High molecular weight chitosan-complexed RNA nanoadjuvant for effective cancer immunotherapy. *Pharmaceutics* **2019**, *11*, 680.

[9]   J. D. Masson, G. Crépeaux, F. J. Authier, C. Exley, R. K. Gherardi. Critical analysis of reference studies on the toxicokinetics of aluminum-based adjuvants. *J. Inorg. Biochem.* **2018**, *181*, 87–95.

[10] J. D. Campbell. Development of the CpG Adjuvant 1018: A Case Study. *Methods Mol. Biol.* **2017**, *1494*, 15–27.

[11] X. Tan, F. Jia, P. Wang, K. Zhang. Nucleic acid-based drug delivery strategies. *J. Control. Release* **2020**, *323*, 240–252.

[12] S. Kimura, I. A. Khalil, Y. H. A. Elewa, H. Harashima. Novel lipid combination for delivery of plasmid DNA to immune cells in the spleen. *J. Control. Release* **2021**, *330*, 753–764.

[13] E. Samaridou, J. Heyes, P. Lutwyche. Lipid nanoparticles for nucleic acid delivery: Current perspectives. *Adv. Drug Deliv. Rev.* **2020**, *154–155*, 37–63.

[14] M. K. Lee. Clinical usefulness of liposomal formulations in cancer therapy: Lessons from the experiences of doxorubicin. *J. Pharm. Investig.* **2019**, *49*, 203–214.

[15] C. B. Roces, G. Lou, N. Jain, S. Abraham, A. Thomas, G. W. Halbert, Y. Perrie. Manufacturing considerations for the development of lipid nanoparticles using microfluidics. *Pharmaceutics* **2020**, *12*, 1095.

[16] G. Shim, D. Kim, S. Lee, R. S. Chang, J. Byun, Y. K. Oh. Staphylococcus aureus-mimetic control of antibody orientation on nanoparticles. *Nanomedicine* **2019**, *16*, 267–277.

[17] Y. Wu, Q. Li, G. Shim, Y. K. Oh. Melanin-loaded CpG DNA hydrogel for modulation of tumor immune microenvironment. *J. Control. Release* **2021**, *330*, 540–553.

[18] Q. V. Le, J. Suh, J. J. Choi, G. T. Park, J. W. Lee, G. Shim, Y. K. Oh. In situ nanoadjuvant-assembled tumor vaccine for preventing long-term recurrence. *ACS Nano* **2019**, *13*, 7442–7462.

[19] D. Kim, J. Byun, J. Park, Y. Lee, G. Shim, Y. K. Oh. Biomimetic polymeric nanoparticle-based photodynamic immunotherapy and protection against tumor rechallenge. *Biomater. Sci.* **2020**, *8*, 1106–1116.

[20] M. Matsumoto, M. Tatematsu, F. Nishikawa, M. Azuma, N. Ishii, A. Morii-Sakai, H. Shime, T. Seya. Defined TLR3-specific adjuvant that induces NK and CTL activation without significant cytokine production in vivo. *Nat. Commun.* **2015**, *6*, 6280.

[21] B. L. Lee, G. M. Barton. Trafficking of endosomal Toll-like receptors. *Trends Cell Biol.* **2014**, *24*, 360–369.

[22] V. Patil, S. Renu, N. Feliciano-Ruiz, Y. Han, Y.; A. Ramesh, J. Schrock, S. Dhakal, H. HogenEsch, G. J. Enukaradhya. Intranasal delivery of inactivated influenza virus and poly(I:C) adsorbed corn-based nanoparticle vaccine elicited robust antigen-specific cell-mediated immune responses in maternal antibody positive nursery pigs. *Front. Immunol.* **2020**, *11*, 596964.

[23] S. F. Lin, P. L. Jiang, J. S. Tsai, Y. Y. Huang, S. Y. Lin, J. H. Lin, D. Z. Liu. Surface assembly of poly(I:C) on polyethyleneimine-modified gelatin nanoparticles as immunostimulatory carriers for mucosal antigen delivery. *J. Biomed. Mater. Res. B Appl. Biomater.* **2019**, *107*, 1228–1237.

[24] G. Du, M. Leone, S. Romeijn, G. Kersten, W. Jiskoot, J. A. Bouwstra. Immunogenicity of diphtheria toxoid and poly(I:C) loaded cationic liposomes after hollow microneedle-mediated intradermal injection in mice. *Int. J. Pharm.* **2018**, *547*, 250–257.

[25] V. Schuette, M. Embgenbroich, T. Ulas, M. Welz, J. Schulte-Schrepping, A. M. Draffehn, T. Quast, K. Koch, M. Nehring, J. König. Mannose receptor induces T-cell tolerance via inhibition of CD45 and up-regulation of CTLA-4. *Proc. Natl. Acad. Sci. USA* **2016**, *113*, 10649–10654.

[26] M. Pei, R. Xu, C. Zhang, X. Wang, C. Li, Y. Hu. Mannose-functionalized antigen nanoparticles for targeted dendritic cells, accelerated endosomal escape and enhanced MHC-I antigen presentation. *Colloids Surf. B Biointerfaces* **2021**, *197*, 111378.

[27] S. K. Gulla, B. R. Rao, G. Moku, S. Jinka, N. V. Nimmu, S. Khalid, C. R. Patra, A. Chaudhuri. In vivo targeting of DNA vaccines to dendritic cells using functionalized gold nanoparticles. *Biomater. Sci.* **2019**, *7*, 773–788.

[28] P. Foroozandeh, A. A. Aziz. Insight into cellular uptake and intracellular trafficking of nanoparticles. *Nanoscale Res. Lett.* **2018**, *13*, 339.

[29] H. Hatakeyama, H. Akita, H. Harashima. A multifunctional envelope type nano device (MEND) for gene delivery to tumours based on the EPR effect: A strategy for overcoming the PEG dilemma. *Adv. Drug Deliv. Rev.* **2011**, *63*, 152–160.

[30] H.-S.Jeong, K. S. Na, H, Hwang, P.-S. Oh, D. H. Kim, S. T. Lim, M. H. Sohn, H. J. Jeong. Effect of space length of mannose ligand on uptake of mannosylated liposome in RAW 264.7 cells: In vitro and in vivo studies. *J. Biomed. Mater. Res. A* **2014**, *102*, 4545–4553.

[31] E. Blanco, H. Shen, M. Ferrari. Principles of nanoparticle design for overcoming biological barriers to drug delivery. *Nat. Biotechnol.* **2015**, *33*, 941–951.

[32] Y. Dölen, M. Valente, O. Tagit, E. Jäger, E. A. W. Van Dinther, N. K. van Riessen, M. Hruby, U. Gileadi, V. Cerundolo, C. G. Figdor. Nanovaccine administration route is critical to obtain pertinent iNKT cell help for robust anti-tumor T and B Cell responses. *Oncoimmunology* **2020**, *9*, 1738813.

Chapter 4

Tannic acid-based nanomaterials for tolerogenic immunotherapy of rheumatoid arthritis

Chapter 4. Tannic acid-based nanomaterials for tolerogenic immunotherapy of rheumatoid arthritis

4.1. Introduction

Rheumatoid arthritis (RA), a chronic inflammatory disease characterized by swollen and stiff joints, arises more predominantly in females and the elderly [1, 2]. The current principal therapies for RA include the application of non-steroidal anti-inflammatory drugs (NSAIDs) and disease-modifying anti-rheumatic drugs (DMARDs) [3]. NSAIDs can alleviate inflammation in RA and DMARDs can achieve disease remission and delay joint deformity by interfering with the progression of inflammation. However, some patients fail to respond and there are risks for adverse effects. The traditional NSAIDs, such as diclofenac, naproxen, and ibuprofen, can trigger gastrointestinal events and cardiovascular problems [4]. Long-term use of nonbiological DMARDs, such as methotrexate and leflunomide, can lead to liver and lung problems [2]. Additionally, these approaches seek to induce remission and delay joint damage rather than working to modulate autoimmunity and maintain immune system homeostasis.

Efforts to induce antigen-specific tolerance and thereby dampen autoimmunity have recently emerged as an approach for treating autoimmune disease without inducing systemic immune suppression. Antigen-presenting cells (APC), especially dendritic cells (DC), play a critical role in initiating and regulating immune tolerance [5]. Compared with immunosuppressive therapies, tolerogenic immunotherapy via tolerogenic DC induction modulates the immune system to reduce autoreactive T cells and develop regulatory T cell (Treg) populations. Recently, tolerogenic immunotherapy has been investigated for treating autoimmune diseases such as type 1 diabetes and multiple sclerosis by inducing antigen-specific tolerances in which insulin peptides and myelin oligodendrocyte glycoprotein peptides, respectively, act as self-antigens [6]. To achieve successful antigen-specific tolerization for RA treatment, researchers need to investigate self-antigens of RA.

In the clinic, autoantibodies toward immunoglobulin G (IgG) and citrullinated proteins are used as markers of RA [7]. IgG is not specific for RA patients, as it occurs in many inflammatory conditions. In contrast, citrullinated proteins are increased with relative specificity in RA patients, while negligible levels are seen in other inflammatory disorders [8]. Environmental stimuli or genetic risk factors can trigger citrullination as a post-translational modification of various proteins, such as collagen, filaggrin, fibrinogen, and vimentin. These citrullinated proteins are abundant in RA patients, and anti-citrullinated protein antibodies are detected in the sera of almost 80% RA patients, indicating that citrullinated proteins act as critical self-antigens in the progression of RA [9, 10]. A multiepitope peptide including the sequences of various citrullinated autoantigens reportedly induced immune tolerance and ameliorated inflammatory

symptoms in the adjuvant arthritis rat and CIA mouse models [11, 12, 13]. Thus, citrullinated proteins appear to have potential as autoantigens for inducing antigen-specific immune tolerance in RA.

For the induction of immune tolerance to treat autoimmune diseases, an emerging approach focuses on using nanoparticles to simultaneously co-deliver specific amounts of self-antigens and tolerogenic drugs to DC. However, most of the nanoparticles designed to date lacked DC-specific targeting ligands and failed to amplify antigen-specific immune tolerance or show therapeutic efficacy. Abatacept, also known as CTLA4-Ig, is a fusion protein comprising the extracellular domain of cytotoxic T lymphocyte associated protein 4 (CTLA4) and the Fc region of IgG1 [8, 14]. This fusion protein has been used to treat autoimmune diseases like RA by binding to the co-stimulatory molecules, CD80 and CD86, on the surface of DC; this blocks the interaction of CD80/CD86 with CD28 on effector T cells to prevent their activation [15, 16]. Hence, abatacept offers the possibility of simultaneously blocking T cell activation and targeting DC.

To generate antigen-specific immune tolerance via a DC-specific targeting approach for RA treatment, an abatacept-conjugated nanovaccine composed of a core tannic acid nanoparticle (TN), citrullinated peptide (CitP), and dexamethasone (Dexa) was designed (Figure 1). Tannic acid, with its phenol-rich structure, is capable of binding to various polymers, such as collagen [17]. As a result, it is reasonable to create a nanocore through hydrogen bonding with alcohol residue-containing polymers such as PVA. Moreover, tannic acid is a well-known antioxidant agent and Dexa is a potent tolerogenic agent that can induce tolerogenic DC. For DC-targeted delivery, TN was coated with a Dexa-loaded lipid layer (to create DTN) and the surface was engineered with abatacept and the self-antigen, CitP, to yield AbaCitDTN. Here, the tolerogenic nanovaccine, AbaCitDTN, offers the possibility of maximizing DC targeting, reprogramming autoimmunity to antigen-specific immune tolerance, and maintaining immune system homeostasis for the treatment of RA.
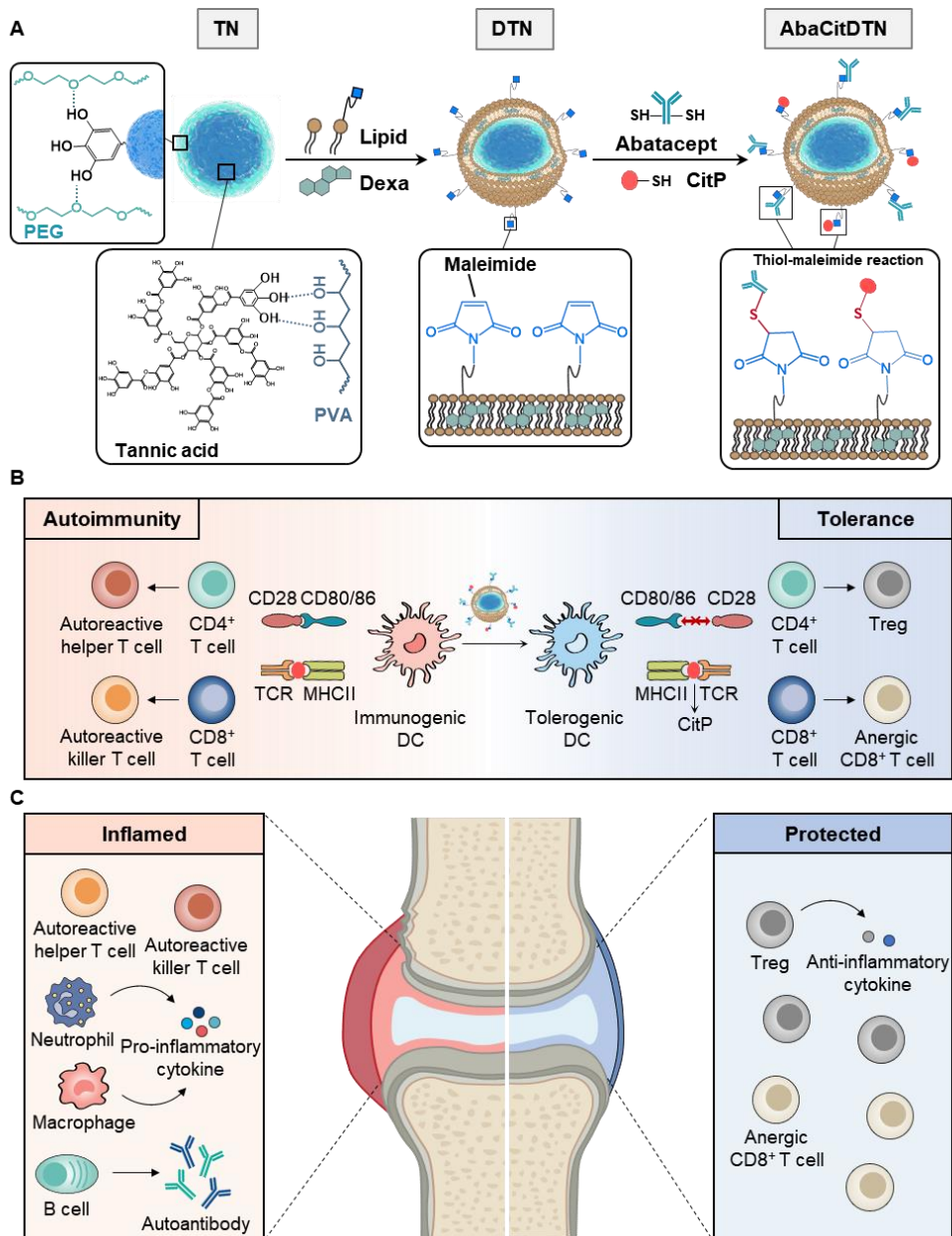
Figure 1. Tolerogenic reprogramming of DC by AbaCitDTN. A) Synthesis procedure of AbaCitDTN. B) Proposed mechanism through which AbaCitDTN induces immune tolerance against CitP in the lymphoid organs. C) Proposed effect of tolerogenic DC induction in ameliorating RA symptoms.

4.2. Material and Method
4.2.1. Preparation of nanoparticles

As core nanoparticles, tannic acid-based nanoparticles were constructed. In brief, 1 mg/mL polyvinyl alcohol (PVA) was mixed with an equal volume of 1 mg/mL tannic acid solution. This mixture was added to a

solution of polyethylene glycol (PEG) (molecular weight 8000; Sigma-Aldrich, St. Louis, MO, USA) at a weight ratio of 1:24. After incubation at room temperature for 10 min, the resulting tannic acid-based core nanoparticles (TN) were purified by three rounds of centrifugation with triple distilled water (TDW) at 1100 x g for 15 min.

Lipid-coated TN (LTN) were prepared using a thin-film hydration method, as previously reported [18]. Briefly, 1,2-dipalmitoyl-sn-glycero-3-phosphocholine (16:0 PC), 1,2-dipalmitoyl-sn-glycero-3-phospho-(1'-rac-glycerol) (sodium salt) (16:0 PG), and 1,2-distearoyl-sn-glycero-3-phosphoethanolamine-N-[maleimide (polyethylene glycol)-2000] (ammonium salt) (DSPE-PEG2000 Maleimide) were dissolved in chloroform at a ratio of 7:2.8:0.2 (m/m). In some experiments, cyanine 5-conjugated 1,2-dioleoyl-sn-glycero-3-phosphoethanolamine (18:1 Cy5 PE, Avanti Polar Lipids, Alabaster, AL, USA) was added at total lipid contents of 0.066 % and 0.66 % for cellular and animal imaging, respectively. To load Dexa to the nanoparticles, Dexa was added into the lipid mixture at a ratio of 0.3:10 (m/m). After the solvent was removed by rotary evaporation, the lipid film was sonicated with 1 mg of TN in 1 mL of TDW. The resulting Dexa-loaded lipid-coated tannic acid core nanoparticles (DTN) were passed through a 0.4-µm membrane filter using an extruder. For some experiments, lipid nanoparticles (LN) and Dexa-loaded lipid nanoparticles without a tannic acid core (DLN) were prepared by hydrating the lipid film with TDW.

For modification of DTN with CitP (CitDTN), cysteine-modified citrullinated peptide (CitP-Cys, VCitLCitSSVESTCitGRSCitPAPPPACitGLTC; Peptron, Daejeon, Republic of Korea) was added into DTN at a TN:CitP-Cys weight ratio of 1:0.2 and reacted at 4 °C overnight [11]. For surface modification of CitDTN with abatacept (AbaCitDTN), abatacept was thiolated with Traut's reagent and conjugated using the maleimide–thiol reaction. Briefly, abatacept was dissolved in phosphate-buffered saline (PBS) (pH 8.0) and reacted with Traut's reagent for 1 h at room temperature. Unreacted Traut's reagent was removed from the thiolated abatacept using a 50 kDa Amicon Ultra filter (Merck Millipore, Burlington, MA, USA). For some experiments, OVA was modified with thiol groups using Traut's reagent, followed by removal of unreacted Traut's reagent with a 3 kDa Amicon Ultra filter. Thiolated abatacept and CitP-Cys were then added to DTN at a weight ratio of 1:1:0.2 and reacted overnight at 4 °C. For other experiments, thiolated abatacept and thiolated OVA were reacted with DTN at a weight ratio of 1:1:0.2. The resulting AbaCitDTN or AbaOVADTN was purified by centrifugation at 27,000 x g for 15 min, and the pellet was reconstituted in 5% glucose for further experiments. For some experiments, DLN was modified with CitP and abatacept to yield AbaCitDLN.

4.2.2. Characterization of nanoparticles

Nanoparticles were characterized by morphology, size, surface charge, elemental analysis, and diverse spectrochemical analysis. The morphology was observed using a Tecnai F20 transmission electron microscope (TEM) (FEI, Hillsboro, Oregon, USA). The presence of elemental carbon, oxygen, and phosphate in nanoparticles was evaluated by field-emission scanning electron microscopy (FE-SEM) (AURIGA; Carl Zeiss, Oberkochen, Germany). Nanoparticle size and surface charge were measured by dynamic light scattering (DLS) using an ELSZ-1000 instrument (Otsuka Electronics Co., Osaka, Japan). The Raman spectra of nanoparticles were analyzed using a Raman microscope (LabRAM HR Evolution, HORIBA, Kyoto, Japan) at a laser wavelength of 532 nm.

Optical imaging and Raman mapping were performed using a LabRAM HR Evolution, with a 500-3500 cm^{-1} range within a 20 x 20 μm^2 area using a 2 x 2 μm^2 point size. Lyophilized powder was prepared for Raman analysis. The Fourier transformation infrared (FT-IR) spectrum of the nanoparticles was analyzed using an attenuated total reflection method and an FT-IR spectrometer (FT/IR-4700, JASCO, Tokyo, Japan) with lyophilized powder; the measurement resolution was 4 cm^{-1}. X-ray photoelectron spectroscopy (XPS) spectra were obtained for elemental analysis (Axis-HSi; Kratos Analytical Ltd., Manchester, UK) and data were analyzed with the CasaXPS software (Casa Software Ltd., Teignmouth, UK). For measurement of XPS spectra, samples were lyophilized and stabilized in a vacuum chamber under an ultra-high vacuum (10^{-9} mbar) for 24 h. The crystallinity of samples was confirmed by X-ray diffraction (XRD) using an X-ray diffractometer (D8 Advance 2020, Bruker, Billerica, MA, USA); the samples were prepared with lyophilized powder.

4.2.3. Quantification of components in nanoparticles

The amount of tannic acid in nanoparticles was evaluated using the 2,2-diphenyl-1-picrylhydrazyl (DPPH) assay as previously reported [19]. In brief, DPPH was prepared in ethanol (0.2 mM) and mixed with 1 mg/mL nanoparticles at a ratio of 5:1 (v/v), and the mixture was vortexed and incubated in the dark for 1 h. The absorbance of samples was measured at 517 nm using a Microplate Reader (Molecular Devices, San Jose, CA, USA). The tannic acid concentration was measured based on a standard curve prepared by reacting different concentrations of tannic acid with DPPH.

The amounts of Dexa and CitP in AbaCitDTN were evaluated by high-performance liquid chromatography (HPLC). For Dexa quantification, lyophilized nanoparticles were dissolved in methanol and sonicated for 30 min to extract Dexa. The solution was centrifuged at 27,000 x g for 20 min and supernatants were collected and injected into a C18 column (Nucleosil 100-5 C18; Macherey-Nagel, Düren, Germany). The column was eluted using a mobile phase consisting of TDW and acetonitrile at a ratio of 70:30

(v/v). The flow rate was set at 1 mL/min and the Dexa peak was detected at 254 nm.

For CitP quantification, nanoparticles were centrifuged at 27,000 x g for 20 min and free peptides in the supernatant were collected and injected into a C18 HPLC column. The column was eluted with a mobile phase consisting of 0.1% trifluoroacetic acid in TDW (solvent A) and 0.1% trifluoroacetic acid in acetonitrile (solvent B). The flow rate was fixed at 1 mL/min and the following gradient was used: 3%-20% B over 2 min, 20%-50% B over 10 min, 50%-70% B over 1 min, and 70%-3% B over 4 min. The column temperature was set to room temperature and the peptide peak was detected at 220 nm. The amount of abatacept in nanoparticles was quantified using a bicinchoninic acid (BCA) assay kit (Thermo Fisher Scientific, Waltham, MA, USA) following the manufacturer's instructions.

4.2.4. Measurement of abatacept conjugated onto AbaCitDTN

The presence of conjugated abatacept on AbaCitDTN was tested by sodium dodecyl sulfate-polyacrylamide gel electrophoresis (SDS-PAGE) and flow cytometry. For SDS-PAGE analysis, abatacept and various formulations were treated with SDS containing 2-mercaptoethanol (4 x; GenDEPOT, Katy, TX, USA) for 10 min at 100 °C. SDS-PAGE was run at 100 V for 90 min, and the gel was stained with Coomassie Brilliant Blue (Bio-Rad, Hercules, CA, USA).

For flow cytometry, Cy5-labeled DTN, CitDTN, AbaDTN, and AbaCitDTN were stained with phycoerythrin (PE)-conjugated anti-human CTLA4 antibody (BioLegend, San Diego, CA, USA) for 1 h and centrifuged at 27,000 x g for 20 min [20]. Nanoparticles were resuspended in 5% glucose in TDW, and the fluorescence signals of nanoparticles and abatacept were detected using a CytoFLEX LX Flow Cytometer (Beckman Coulter, Brea, CA, USA).

4.2.5. Evaluation of radical-scavenging effect

The radical-scavenging abilities of tannic acid-based nanoparticles were evaluated using both colorimetric and fluorescence methods. The O_2^- scavenging activity was assessed using the nitro blue tetrazolium (NBT) assay [21] A solution of 75 μM NBT chloride (Cayman chemical, Ann Arbor, MI, USA), 20 μM riboflavin (Sigma-Aldrich), and 12.5 mM methionine (Sigma-Aldrich) in PBS (pH 7.4) was prepared and mixed with varying concentrations of nanoparticles. Following 15 min of ultraviolet irradiation, the absorbance spectrum was measured using a Microplate Reader (Molecular Devices). The OH· scavenging activity was evaluated by measuring the fluorescence of 2-hydroxyterephthalic acid [22]. A solution of 0.5 mM terephthalic acid (Sigma-Aldrich) and 2 mM H_2O_2 in PBS (pH 7.4) was mixed with varying concentrations of nanoparticles. After incubation in the dark for 12 h, the fluorescence emission spectrum was obtained using a 315 nm excitation wavelength. The DPPH assay was

performed by mixing a solution of 0.2 mM DPPH in ethanol with varying concentrations of nanoparticles, and the UV-visible absorbance at 517 nm was monitored using a Microplate Reader (Molecular Devices).

4.2.6. In vitro study of nanoparticle uptake by DC

The in vitro binding of and endocytosis of nanoparticles into bone marrow-derived DC (BMDC) were studied using confocal microscopy and flow cytometry. BMDC were isolated as previous reported [23] For fluorescent imaging, BMDC (1 x 10^6 cells/well) were seeded onto a confocal dish and treated with 1 mg/mL Cy5-labeled nanoparticles for 1 h. The cells were washed with PBS, stained with LysoTracker Green DND-26 (Thermo Fisher Scientific) and Hoechst 33342 (Sigma-Aldrich), and fixed with 4% formaldehyde in PBS for 10 min. The cellular co-localization of nanoparticles and LysoTracker was observed at different time points under confocal laser scanning microscopy (Leica Microsystems, Wetzlar, Germany). For flow cytometry, BMDC (1 x 10^6 cells/well) were seeded onto 24-well plates and treated with 1 mg/mL Cy5-labeled nanoparticles for 1 h. Cells were harvested and washed with PBS, and the fluorescence intensity was quantified by flow cytometry. For the CD80/CD86-blocking study, BMDC were pre-treated with anti-mouse CD80 antibody (aCD80, 20 μg/1 x 10^6 cells; BioLegend) or anti-mouse CD86 antibody (aCD86, 20 μg/1 x 10^6 cells; BioLegend) for 1 h. The cells were then washed with PBS, treated with Cy5-labeled nanoparticles for 1 h, and analyzed by flow cytometry.

4.2.7. In vitro tannic acid core-mediated modulation of inflammatory signaling

The in vitro modulation of inflammatory signaling in BMDC was evaluated using western blotting and reverse transcription polymerase chain reaction (RT-PCR). For western blotting, BMDC were incubated with various nanoparticles at a dose equivalent to 10 μM Dexa for 1 h. The medium was refreshed, and the cells were incubated with 1 μg/mL of LPS for another 1 h. The cells were washed with PBS, and the nuclear protein was extracted using the NE-PER Nuclear and Cytoplasmic Extraction Kit (Thermo Fisher Scientific).

The protein concentration was quantified using a BCA assay kit. Equal amounts of nuclear protein were loaded onto SDS-PAGE (10%), transferred to polyvinylidene fluoride membranes, and blocked with 3% bovine serum albumin in Tris-buffered saline with 0.1% of Tween-20 for 1 h. The membranes were probed with anti-NF-κB p65 antibody (Abcam, Cambridge, UK) or anti-Histone H3 antibody (Abcam) at 4 °C overnight, followed by incubation with horseradish peroxidase (HRP)-linked anti-rabbit IgG (Cell signaling, Denver, MA, USA) for 1 h. The signals were detected using an Amersham ECL Prime Western Blotting detection reagent kit (GE Healthcare, Chicago, IL, USA). The intensity of NF-κB p65 and Histone H3

was quantified using ImageJ software (National Institutes of Health, Bethesda, MD, USA).

For RT-PCR, BMDC were incubated with various nanoparticles for 1 h, followed by incubation with 1 μg/mL of LPS in fresh medium for another 6 h. Total RNA was extracted from BMDC using the TRIzol reagent (Invitrogen, Carlsbad, CA, USA), and cDNA synthesis was conducted using the AccuPower RT PreMix (Bioneer, Daejeon, Republic of Korea). Real-time quantitative PCR was performed using the TOPreal™ SYBR Green qPCR High-ROX PreMIX (enzynomics, Daejeon, Republic of Korea). The primer sequences used in this study are listed in Table 1.

Table 1. Primer sequences for quantitative real time-PCR

Gene	Primer sequence (5' - 3')	
	Forward sequence	Reverse sequence
GAPDH	CATGGCCTCCAAGGAGTAAGA	GAGGGAGATGCTCAGTGTTGG
HIF1α	AATACATTTTCTCTGCCAGTTTTCTG	TTGCTGCATCTCTAGACTTTTCTTTT
iNOS	CACCTTGGAGTTCACCCAGT	ACCACTACTCGTACTTGGGATGC
COX-2	CACTACATCCTGACCCACTT	ATGCTCCTGCTTGAGTATGT

4.2.8. In vitro study of tolerogenic DC induction

In vitro tolerogenic DC induction was evaluated using flow cytometry and confocal microscopy. As markers of tolerogenic DC, the surface expression levels of CD86, CD80, and CD40, and the intracellular expression levels of tumor necrosis factor alpha (TNF-α) and transforming growth factor beta (TGF-β) were measured.

For flow cytometry, BMDC were incubated with various nanoparticles at a dose equivalent to 10 μM Dexa for 1 h. The medium was refreshed and the cells were incubated for another 48 h. To evaluate the expression levels of CD86, CD80, and CD40, BMDC were activated with 1 μg/mL of LPS (Sigma-Aldrich) for 24 h. To evaluate the surface expression levels of TNF-α and TGF-β, BMDC were activated with 1 μg/mL of LPS and 5 μg/mL of brefeldin A (Invitrogen, Waltham, MA, USA) for 6 h. Surface-expressed CD86, CD80, and CD40 were evaluated using Fluorescein (FITC)-conjugated anti-mouse CD11c antibody, allophycocyanin (APC)-conjugated anti-mouse CD86, CD80 and CD40 antibodies, and PerCP/Cy5.5-conjugated anti-mouse major histocompatibility complex (MHC) II antibody. The intracellular expression levels of TNF-α and TGF-β were evaluated using APC-conjugated anti-mouse TNF-α and TGF-β antibodies with intracellular staining buffer (BioLegend), respectively.

For confocal imaging, BMDC were seeded onto a confocal dish and treated with various nanoparticles for 48 h. After stimulation with LPS and brefeldin A for 6 h, BMDC were fixed with 4% formaldehyde for 10 min, and then stained with APC-conjugated anti-mouse TNF-α antibody and

Hoechst 33342 dye. All antibodies were obtained from BioLegend. The fluorescence of cells was observed using confocal laser scanning microscopy.

4.2.9. In vitro ROS-scavenging effect of nanoparticles on DC

The in vitro ROS-scavenging effect of nanoparticles on DC was evaluated using a nitric oxide assay, intracellular ROS imaging, and flow cytometry. The isolated BMDC were incubated with various nanoparticles at a dose corresponding to 10 μM Dexa for 1 h. The medium was refreshed and the cells were incubated for another 24 h. The BMDC were activated with 1 μg/mL of LPS for 6 h. For the nitric oxide assay, the medium was collected and the amount of nitric oxide in the supernatant was measured using Griess reagent. For fluorescent imaging of intracellular ROS, the BMDC were stained with 10 μM CM-H2DCFDA in PBS for 30 min and the cells were fixed with 4% formaldehyde for 10 min and stained with Hoechst 33342 dye for 10 min. The fluorescence of cells was observed using a confocal laser scanning microscope. For flow cytometry, cells were stained with CM-H2DCFDA, harvested, washed with PBS, and analyzed by flow cytometry.

4.2.10. In vitro blockade of the interaction between DC and T cells

The ability of nanoparticles to block the co-stimulatory molecule interaction between DC and T cells was evaluated using confocal microscopy, a T cell proliferation assay, and an interleukin-2 (IL-2) secretion assay. T cells were isolated from the spleens of DBA/1 mice using nylon wool columns, as previously reported [24]. To visualize the interaction between DC and T cells, T cells were pre-stained with primary rat anti-mouse CD3 antibody (BioLegend) and PerCP/Cy5.5-tagged anti-rat IgG antibody (BioLegend). The cells were then seeded onto poly-l-lysine coverslips and co-cultured with DC that had been pre-stained with FITC-tagged anti-mouse CD11c antibody (BioLegend) at a T cell : DC ratio of 1:1. Cy5-labled nanoparticles (1 mg/mL) were added and the co-culture system was incubated for 1 h. The cells were then washed three times with PBS, fixed with 4% formaldehyde, and stained with Hoechst 33342 dye. The fluorescence of cells was visualized using a confocal laser-scanning microscope.

For assessment of IL-2 secretion, splenocytes were seeded onto anti-CD3 antibody- and recombinant CD80 protein-Fc conjugate-coated plates along with the various nanoparticles. A 96-well plate was coated with 10 μg/mL anti-CD3 antibody (Bio X Cell, Lebanon, NH, USA) and 10 μg/mL CD80-Fc (BioLegend) overnight at 4 °C. After washing the plate with PBS, either free abatacept (50 μg/mL) or various nanoparticles at a dose corresponding to 10 μM Dexa were added for 1 h. The splenocytes were washed with PBS and seeded at a density of 2 x 10^5 cells/well. The plate was incubated for 72 h, the supernatant was collected, and the amount of IL-2 in the supernatant

was measured using an IL-2 enzyme-linked immunosorbent assay (ELISA) kit (R&D Systems, Minneapolis, MN, USA).

For the T cell proliferation assay, splenocytes were pre-stained with 5 μM 5,6-carboxy-succinimidyl-fluoresceine-ester (CFSE) dye and seeded onto an anti-CD3 antibody- and CD80-Fc-coated plate. The plate was incubated for 72 h, and splenocytes were harvested and stained with APC-tagged anti-mouse CD3 antibody, PE-tagged anti-mouse CD4 antibody, and PerCP/Cy5.5-tagged anti-mouse CD8 antibody. All antibodies were from BioLegend. The proliferation of T cells was analyzed using flow cytometry.

4.2.11. Animals

Male 7-week-old DBA/1 mice were purchased from Orient Bio (Kyonggi-do, Republic of Korea) under standard pathogen-free conditions at the Animal Center for Pharmaceutical Research, Seoul National University. All animal experiments were carried out under approved protocols and in accordance with the Guidelines for the Care and Use of Laboratory Animals of the Institute of Laboratory Animal Resources, Seoul National University (approval number, SNU-210318-3-1, SNU-220227-1).

4.2.12. In vivo biodistribution study

The in vivo biodistribution of nanoparticles was evaluated using molecular imaging, flow cytometry. DBA/1 mice were injected subcutaneously injected at the center of the lower back with 0.2 mL of 1 mg/mL Cy5-labeled nanoparticles. For molecular imaging, the fluorescence of nanoparticles at lymph nodes and other organs was detected at various time points using an IVIS Spectrum in Vivo Imaging System (PerkinElmer, Waltham, MA, USA). For flow cytometry, lymph nodes were harvested, mashed, and passed through a cell strainer (70 μm). The obtained single-cell suspension was stained with PE-tagged anti-mouse CD11c antibody and PerCP/Cy5.5-tagged anti-mouse MHCII antibody. The overlap of the Cy5 signal with the CD11c$^+$ and MHCII$^+$ cell population was analyzed by flow cytometry. For imaging, cryosections of inguinal lymph nodes were stained with Alexa Fluor 594-conjugated anti-mouse CD11c antibody (BioLegend) and Hoechst 33342 dye and visualized using a THUNDER Imager (Leica Microsystems, Wetzlar, Germany).

4.2.13. In vivo immune tolerance study

The antigen-specific immune tolerance induced by AbaCitDTN was tested in the collagen-induced arthritis (CIA) mouse model, which was induced according to following methods [25]: On day 0, 8-week-old male DBA/1 mice were injected intradermally at the tail with 100 μg of chick type II collagen (CII, 2 mg/mL, Chondrex, Redmond, WA, USA) emulsified with an equal volume of Complete Freund's Adjuvant (CFA, 4 mg/mL, Chondrex). On day 21, the mice received a booster immunization at the tail

with 100 μg of chick CII in an equal volume of Incomplete Freund's Adjuvant (IFA, Chondrex).

To evaluate tolerogenic vaccination efficacy, the mice were divided into six groups and various nanoparticles were injected subcutaneously at the center of the lower back, at doses equivalent to 50 μg of tannic acid, 45 μg of Dexa, and 100 μg of CitP per mouse. Injections were done weekly for a total of four times, starting on the day of the first emulsion injection. The symptoms of mice were monitored every other day and scored using the following criteria described in the Chondrex protocol: 0, normal; 1, mild redness and swelling limited to the toes; 2, moderate redness and swelling of ankle joints or wrists; 3, enhanced redness and swelling of entire paws; 4, severe swelling of entire paws or ankylosed paws and toes. The paw thicknesses of the right and left paws were measured using a caliper.

4.2.14. Suppression of CitP-specific splenocytes by AbaCitDTN

The capability of nanoparticles to suppress CitP-specific splenocytes was evaluated using IFN-γ ELISpot assay and cytokine ELISA. The CIA mouse model was established as previously described, and spleens were harvested 7 days after the boost immunization, followed by dissociation into single-cell suspensions. Splenocytes were then incubated with various nanoparticles at a dose equivalent to 10 μM Dexa for 1 h. The medium was refreshed, and the cells were incubated for 72 h. Splenocytes (4 x 10^6 cells/well) were stimulated with 10 μg/mL CitP or 10 μg/mL OVA$_{323-339}$ (InvivoGen, San Diego, CA, USA), respectively. After 24 h, cells were used for the detection of IFN-γ-secreting cells using an ELISpot kit (BD Bioscience) according to the manufacturer's instructions, and the supernatant was collected for the detection of levels of IL-6, TNF-α, and GM-CSF using ELISA kits (R&D Systems).

4.2.15. Detection of cytokine and chemokine levels in CIA mice

The cytokine and chemokine levels in blood or synovial fluid were measured by ELISA. Mice were injected intradermally with type II collagen emulsion and injected subcutaneously with various nanoparticles. Mice received four weekly treatments with nanoparticles. Mice were sacrificed at 42 days after the first dose of nanoparticles, and blood and hind paws were collected. The hind paws were skinned and homogenized with PBS supplemented with a protease inhibitor (Roche, Basel, Switzerland) using a homogenizer. Each sample was centrifuged at 13,000 x g for 30 min and the supernatant was collected. The levels of IL-6, interferon (IFN)-γ, IL-1β, TNF-α, and C-C Motif Chemokine Ligand 2 (CCL2) were quantified using ELISA kits (R&D Systems, Minneapolis, MN, USA) according to the manufacturer's instructions.

4.2.16. Analysis of antigen-specific immune responses

Antigen-specific immune responses were evaluated by specific antibody titers and enzyme-linked immune absorbent spot (ELISpot) assay. Mice were subcutaneously treated each week with various nanoparticles for a total of four times, starting on the day of the first emulsion injection. For antibody titer analysis, blood samples were collected from the heart at 42 days after the first nanoparticle treatment and serum samples were obtained by centrifugation at 2,000 x g for 20 min. A 96-well immunoplate was coated with 100 μL/well of 10 μg/mL CII or 10 μg/mL CitP in PBS (pH 7.4) overnight at 4 °C. The plate was incubated with 100 μL/well of 100-times diluted serum samples for anti-CitP IgG detection and 10000-times diluted serum samples for anti-CII IgG detection. All serum samples were diluted in blocking buffer. The plate was incubated at room temperature for 2 h. The plate was treated with 100 μL/well of HRP-conjugated anti-mouse IgG (diluted 1:400, Santa Cruz Biotechnology, Dallas, TX, USA) for 2 h, and then with 100 μL/well of H_2O_2 and tetramethylbenzidine mixing solution (1:1, v/v). The optical density at 450 nm was determined immediately using a microplate reader.

For the IFN-γ ELISpot assay, splenocytes were seeded at 4 x 10^6 cells per well for detection of CitP-specific IFN-γ-secreting splenocytes or at 2 x 10^6 cells per well for detection of CII-specific IFN-γ-secreting splenocytes. The cells were then stimulated with 10 μg/mL of CitP or 100 μg/mL CII, respectively. After 24 h of stimulation, the numbers of IFN-γ-secreting cells were evaluated using an ELISpot kit (BD Bioscience) according to the manufacturer's instructions.

4.2.17. Analysis of immune cell profiles in CIA mice

The immune cells profiles of spleen and lymph nodes were analyzed by flow cytometry. Mice were subcutaneously treated each week with various nanoparticles for a total of four times, starting on the day of the first emulsion injection. On day 42 after the first injection, spleens and inguinal lymph nodes were harvested and dissociated into single-cell suspensions using 70-μm cell strainers. Red blood cells were removed using ACK lysis buffer (Thermo Fisher Scientific). The Treg population in the spleen was evaluated by staining cell suspensions with PE-tagged anti-mouse CD4 antibody, FITC-tagged anti-mouse CD25 antibody, and APC-tagged anti-mouse Foxp3 antibody. For IL-17A and IFN-γ analysis, splenocytes were stimulated with phorbol 12-myristate 13-acetate (Sigma-Aldrich), ionomycin (Sigma-Aldrich) and brefeldin A for 4 h.

The Th17 cell population in the spleen was assessed by staining stimulated splenocytes with FITC-tagged anti-mouse CD3 antibody, PE-tagged anti-mouse CD4 antibody, and APC-tagged anti-mouse IL-17A antibody. The pathogenic T cell population was analyzed by staining with FITC-tagged anti-mouse CD3 antibody, PE-tagged anti-mouse CD4 antibody, PerCP/Cy5.5-tagged anti-mouse CD8 antibody, and APC-tagged anti-mouse IFN-γ antibody. DC markers were evaluated by staining cell

suspensions of lymph nodes with FITC-tagged anti-mouse CD11c antibody, PerCP/Cy5.5-tagged anti-mouse MHCII antibody, APC-tagged anti-mouse CD86 antibody, APC-tagged anti-mouse CD80 antibody, or APC-tagged anti-mouse CD40 antibody (all antibodies were from BioLegend).

4.2.18. Microcomputed tomography

The bone architecture and bone erosion were observed by microcomputed tomography (Micro-CT). Mice were subcutaneously treated each week with various nanoparticles for a total of four times, starting on the day of the first emulsion injection. On day 42 after the first injection, hind paws were harvested, fixed in 4% formaldehyde in PBS, and scanned at 90 kV and 88 μA with a resolution of 36 μm using a Quantum GX2 microCT Imaging System (PerkinElmer). The scanned paws were then reconstructed into three-dimensional images. Bone assessment parameters, including the bone volume/total volume (BV/TV), bone surface/bone volume (BS/BV), and bone mineral density (BMD), were quantified for femurs and tibia using the AccuCT microCT Analysis Software (PerkinElmer).

4.2.19. Histology and immunohistochemical study

Mice were subcutaneously treated each week with various nanoparticles for a total of four times, starting on the day of the first emulsion injection. Knee joints were collected on day 42 after the first injection, fixed in 4% formaldehyde in PBS at 4 °C for 24 h, and decalcified with 10% EDTA solution at 4 °C for 4 weeks. The decalcified joints were then embedded in paraffin and stained with hematoxylin and eosin (H&E), safranin O, and toluidine blue. Stained tissues sections were imaged using a Vectra Automated Multispectral Imaging System (PerkinElmer). Semiquantitative scoring was performed as previously reported [26]. Inflammation and bone erosion were scored from H&E-stained images. Inflammation was scored using the following criteria: 0, normal; 1, mild infiltration of inflammatory cells, low cell density; 2, enhanced infiltration of inflammatory cells, increased cell density; 3, maximal infiltration of inflammatory cells, high cell density. Bone erosion was scored using the following criteria: 0, normal, intact bone architecture; 1, small bone erosion at the superficial area of cortical bone; 2, moderate bone erosion at the superficial area of cortical bone; 3, severe bone erosion and complete loss of cortical bone. Cartilage erosion was scored from safranin O-stained images using the following criteria: 0, normal; 1, mild loss of cartilage zone (red) in the superficial layer; 2, moderate loss of cartilage zone (red) in the superficial layer; 3, complete loss of cartilage zone (red) in the superficial layer with only counterstaining (blue) remaining.

For the immunohistochemical study, decalcified knee joints were incubated in 15% sucrose in PBS for 1 h and then in 30% sucrose in PBS for 24 h, and embedded in Tissue-Tek O.C.T. compound (Sakura Finetek, Torrance, CA, USA). The O.C.T. compound was solidified at -80 °C and the

embedded samples were cryosectioned at 10 μm using a microtome. Slide-mounted sections were blocked with 3% bovine serum albumin in PBS for 1 h at room temperature and incubated with Alexa Fluor 488-tagged anti-mouse F4/80 antibody (BioLegend) and Alexa Fluor 647-tagged anti-mouse Ly6G antibody (BioLegend) overnight at 4 °C. The slides were washed three times with PBS, stained with Hoechst 33342 dye for 1 h, and visualized using a THUNDER Imager (Leica Microsystems).

4.2.20. Defensive immune responses against hemagglutinin.

De novo priming of defensive immune responses was evaluated using a hemagglutinin model. DBA/1 mice were subcutaneously administered with various nanoparticles each week for a total of four times. On day 21 after the first injection, the mice were subcutaneously injected with 2 μg of hemagglutinin (Sino Biological, Beijing, People's Republic of China) emulsified with an equal volume of CFA (4 mg/mL). On day 35, a booster injection was performed with 2 μg of hemagglutinin emulsified with an equal volume of IFA.

For anti-hemagglutinin IgG detection, blood samples were collected from the tails each week from day 21 after the first nanoparticle injection, followed by centrifugation at 2,000 x g for 20 min. A 96-well immunoplate was coated with 100 μL/well of 2 μg/mL hemagglutinin in PBS (pH 7.4) overnight at 4 °C. The plate was then incubated with 100 μL/well of 1000-times diluted serum samples for 2 h, followed by incubation with HRP-conjugated anti-mouse IgG for 2 h. Then, the plate was incubated with 100 μL/well of H_2O_2 and tetramethylbenzidine mixing solution. The optical density was read at 450 nm.

For the hemagglutinin-specific IFN-γ ELISpot assay, the mice were sacrificed on day 42 after the first nanoparticle injection. Spleens were harvested, dissociated into single-cell suspensions, and seeded at 4 x 10^6 cells per well. The cells were stimulated with 10 μg/mL of hemagglutinin for 24 h. The hemagglutinin-specific IFN-γ ELISpot was performed using an ELISpot kit according to the manufacturer's instructions.

4.2.21. Statistical analysis

Results are presented as the mean ± standard deviation. GraphPad Prism version 8 (San Diego, CA, USA) was used for statistical analysis. For data sets with more than two groups, the Dunnett's post hoc test was conducted following a one-way analysis of variance (ANOVA). A p value of less than 0.05 was considered to be statistically significant (*$p<0.05$, **$p< 0.01$, ***$p<0.001$, and ****$p<0.0001$).

4.3. Results
4.3.1. Characterization of nanoparticles

To develop and validate the TN-based tolerogenic vaccine formulation, various nanoparticles were developed throughout the research. The TN core

was composed of tannic acid, PVA, and PEG. The driving force of TN synthesis was hydrogen bonding. Because of the polyphenol structure, which is identical to that of tannic acid, the hydroxyl group of PVA generated a hydrogen bond with tannic acid under simple physical mixing. The formed complex was stabilized by PEG, which possesses numerous ether groups. TN synthesis was confirmed by FT-IR spectrum analysis, which revealed all structural properties of each component. TN presented O-H stretching at 3262 cm^{-1}, indicating the polyphenol structure in tannic acid or the alcohol group in PVA [27]; C-H stretching at 2900-2880 cm^{-1}, representing the alkyl chains abundant in PEG and PVA; carbonyl group (C=O) stretching in tannic acid at 1729 cm^{-1}; and C-O stretching in PEG at 1100 cm^{-1} (Figure 2B) [28]. Additionally, TN demonstrated a concentration-dependent ability to scavenge radicals such as the superoxide anion (O_2^-), hydroxyl radical (OH·), and radical biomolecule (Figure 3B).
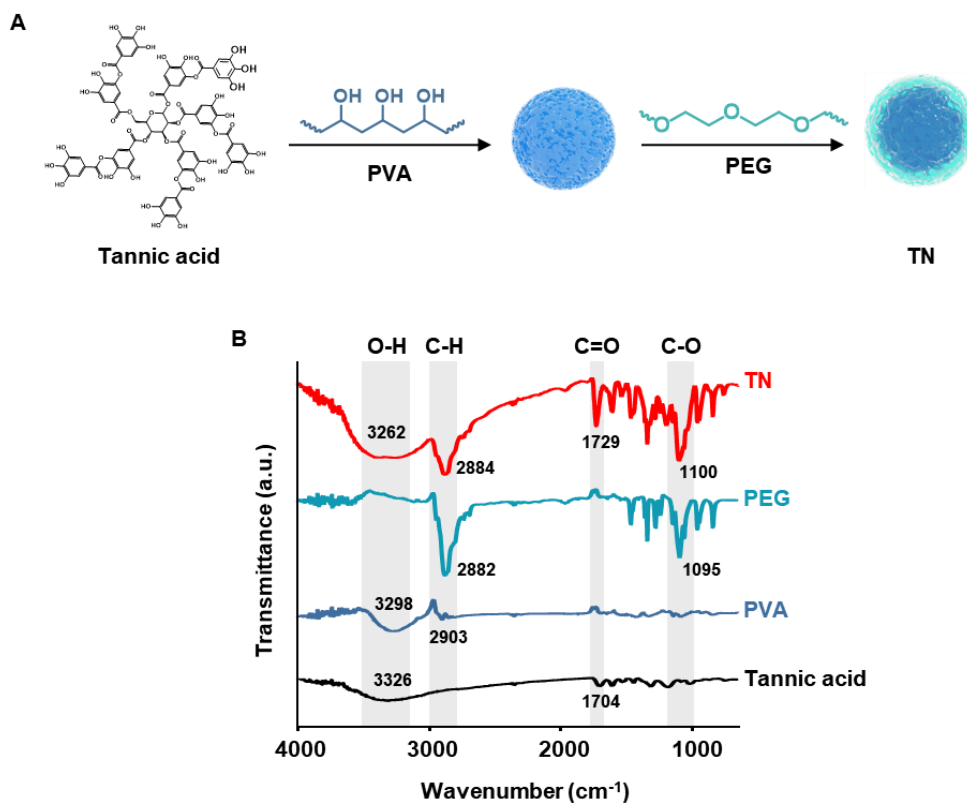

Figure 2. Characterization of TN. A) Procedure for synthesizing TN. B) FT-IR spectra of tannic acid, PVA, PEG, and TN, as analyzed by FT-IR spectrometry.
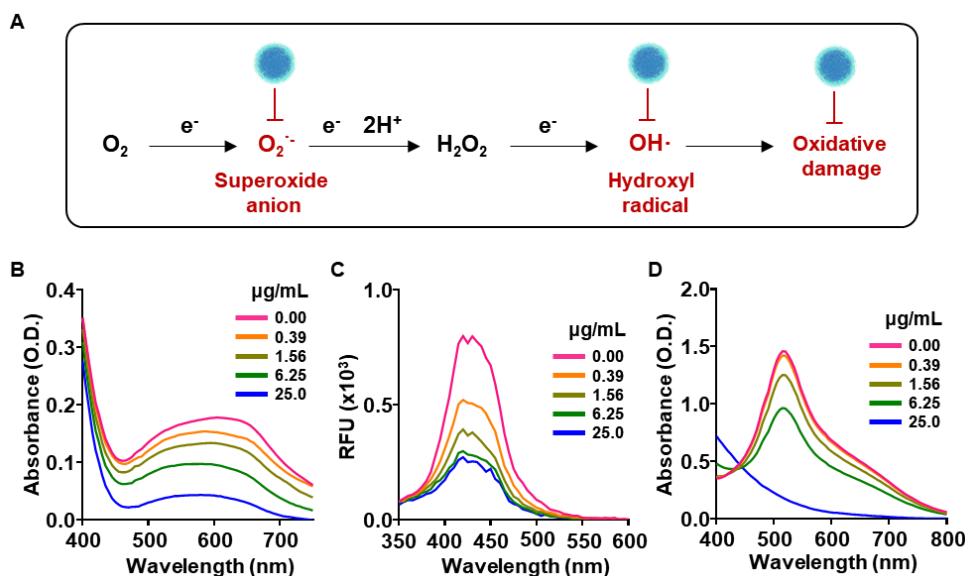
Figure 3. Radical scavenging activity of nanoparticles. A) Proposed radical scavenging mechanism of TN is illustrated. B) Superoxide anion scavenging activity of TN was evaluated using a NBT assay. C) Hydroxyl radical scavenging activity of TN was measured by the fluorescence intensity of 2-hydrxoyterephthalic acid. D) Organic radical compound scavenging activity of TN was measured using DPPH assay.

TEM revealed that AbaCitDTN, was a spherical nanoparticle of 100 nm in size (Figure 4B). SEM imaging confirmed the spherical morphology of AbaCitDTN, and elemental analysis showed that the particles contained carbon (C), oxygen (O) and phosphorus (P) (Figure 4C). The lipid layer was investigated by physicochemical characteristic analysis. The lipid-coated formulations were reduced in size compared to TN, due to the extrusion procedure performed during the core-encapsulation step (Figure 4D). TN can be considered as soft nanomaterials that possess a deformable and flexible nature. After coating with lipids and extruding through 0.4 μm pores, the large-sized lipid-coated TN undergo repolymerization, resulting in the formation of smaller-sized nanoparticles. Lipid coating slightly increased the zeta potential (Figure 4E). This may reflect characteristics of the component lipids, especially DPPC, which has a weak positive charge from an amine group when in water phase [30]. Characteristics of the TN core were found in all formulations by Raman spectroscopy. In range (I), covering 1400-1700 cm^{-1}, the results showed the signals for phenol structures including C-OH plane bending in the aromatic ring (1437 cm^{-1}) and aromatic C=C stretching 8a mode (1605 cm^{-1}). Aromatic C-H stretching was also found in range (II), as evidenced by a sharp and strong peak at 2881 cm^{-1} (Figure 4F), which is believed to represent the TN core structure [29].

The lipid layer coating was confirmed by analyzing the FT-IR spectrum

of the hydrocarbon region (Figure 4G). The lipid-coated formulations, DTN, CitDTN, AbaDTN, and AbaCitDTN, presented C-H stretching peaks due to the fatty acids, as inferred by the similarity of the signals to those obtained from palmitic acid chains, particularly, $\nu_{as}(CH_3)$, $\nu_{as}(CH_2)$, and $\nu_s(CH_2)$ at 2953, 2916, and 2849 cm^{-1}, respectively [31]. On the other hand, the signal at 2884 cm^{-1} can be attributed to the C-H stretching of the PEG in TN.

Abatacept conjugation was confirmed by flow cytometry. In the flow cytometry plots (Figure 4H), TN distributed to the lower-left quadrant due to the lack of a lipid layer and abatacept, which were labeled with Cy5 and PE, respectively. The lipid-coated formulations revealed the expected Cy5 fluorescent signal due to the lipid layer, and AbaDTN and AbaCitDTN further showed the PE signal, which confirmed the presence of abatacept on the nanoparticles.

An important component of the lipid layer, Dexa, was detected and quantified by HPLC. The retention time of Dexa was 15.5 min and each formulation revealed a Dexa peak except for TN. Area under the curve (AUC) analysis of the Dexa HPLC peak with concentration showed linearity. Calculation of the Dexa loading amount according to the AUC value revealed that 18.0 μg of Dexa was encapsulated in 1 mg of nanoparticles. In addition, the tannic acid in nanoparticles was quantified. The results revealed that TN, DTN, CitDTN, AbaDTN, and AbaCitDTN each possessed 9.5 μg of tannic acid in 1 mg of nanoparticles (Figure 5B). Cysteine residue at the C-terminus of CitP was used for conjugation with maleimide group of lipids on nanoparticles through the maleimide-thiol reaction (Figure 5C). CitP was observed by HPLC; the retention time was 8.6 min, which was consistent with the information provided by the manufacturer. To quantify the conjugated CitP for each formulation, the amount of unbound CitP remaining after the conjugation reaction were measured. The AUC-concentration correlation of CitP showed linearity and was found to be optimal for concentration calculation (Figure 5D). These results revealed that 1 mg of each nanoparticle conjugated with 34.0 μg of CitP (Figure 5E).

XPS spectral analysis of AbaCitDTN, provided information on its elemental composition, confirming the presence of a lipid layer and surface modification of nanoparticles. The narrow-scan spectrum of C 1s revealed diverse chemical bonds, including C-C (284.5 eV), C-O-C (285.6 eV), and O-C=O (288.4 eV). The P 2p spectrum indicated the phosphate group of the phospholipid that comprised a major component of the lipid layer, and the S 2p spectrum peak represented abatacept and peptide conjugation via a thioether linker (Figure 4I). The tannic acid-based core of AbaCitDTN retained its antioxidant activity, as tested using the stable radical producer, DPPH: AbaCitDTN time-dependently scavenged the DPPH radical, as analyzed by UV-Vis spectrum measurement (Figure 4J).

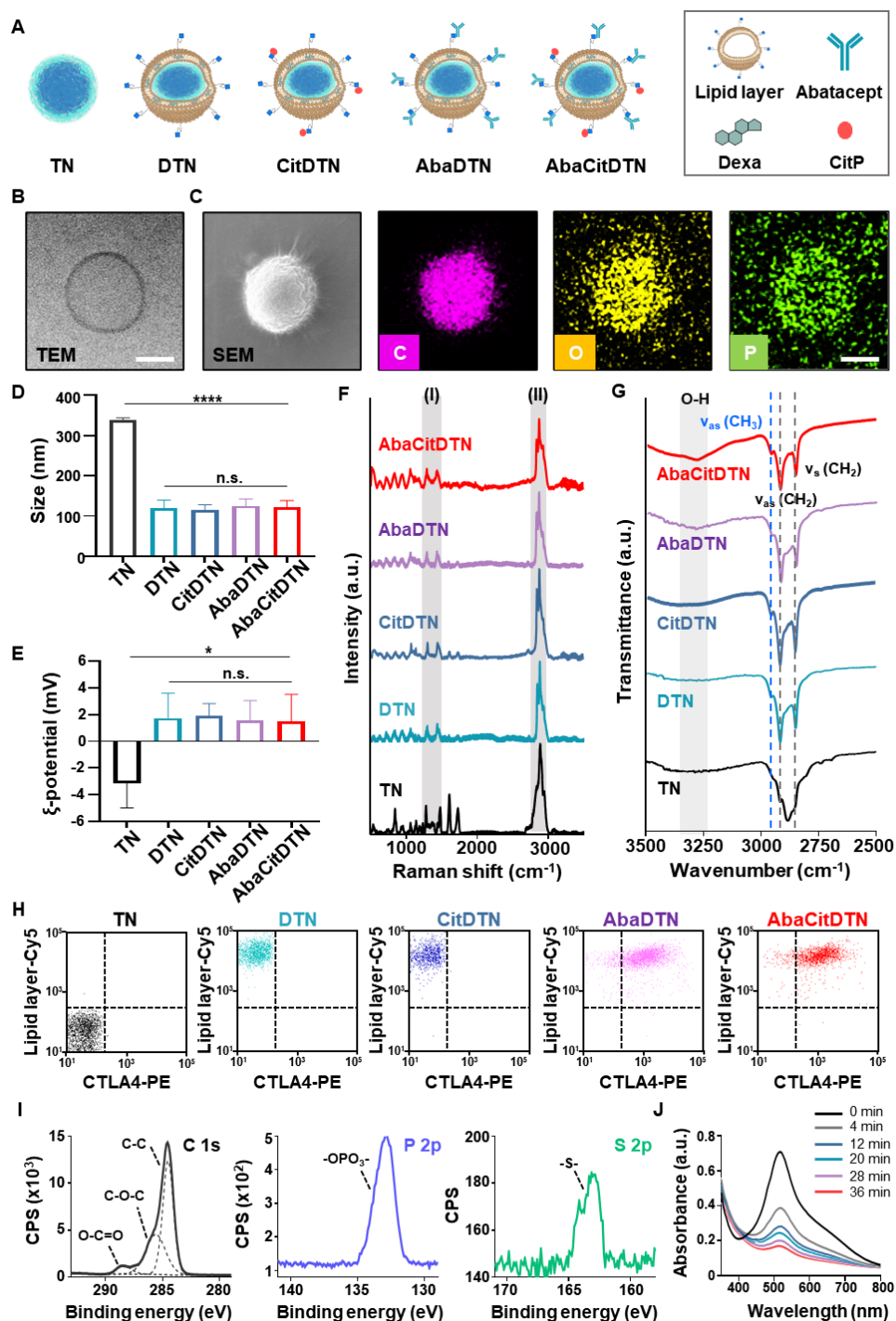**Figure 4.** Characterization of nanoparticles. A) Schematic illustration of various formulations. B) Morphology of AbaCitDTN, as visualized by TEM. Scale bar: 50 nm. C) Elemental analysis of carbon (C), oxygen (O) and phosphorus (P) in AbaCitDTN, as determined by EDS-SEM. Scale bar: 50 nm. D) Mean particle sizes of different nanoparticles, as determined by DLS. E) Zeta potentials of different nanoparticles, as measured by Laser Doppler

Microelectrophoresis. All statistical data are presented as mean $\pm$ SD (n=3; *$p<0.05$, ****$p<0.0001$, n.s., not significant). F) Raman spectra of various nanoparticles, conducted by Raman spectroscopy. G) FT-IR spectra of various nanoparticles were analyzed by FT-IR spectrometry. H) Conjugation of abatacept on nanoparticles was determined by flow cytometry. I) XPS spectra of AbaCitDTN were used for elemental analysis of carbon, phosphorus, and sulfur. J) DPPH radical-scavenging activity of AbaCitDTN was determined over time.
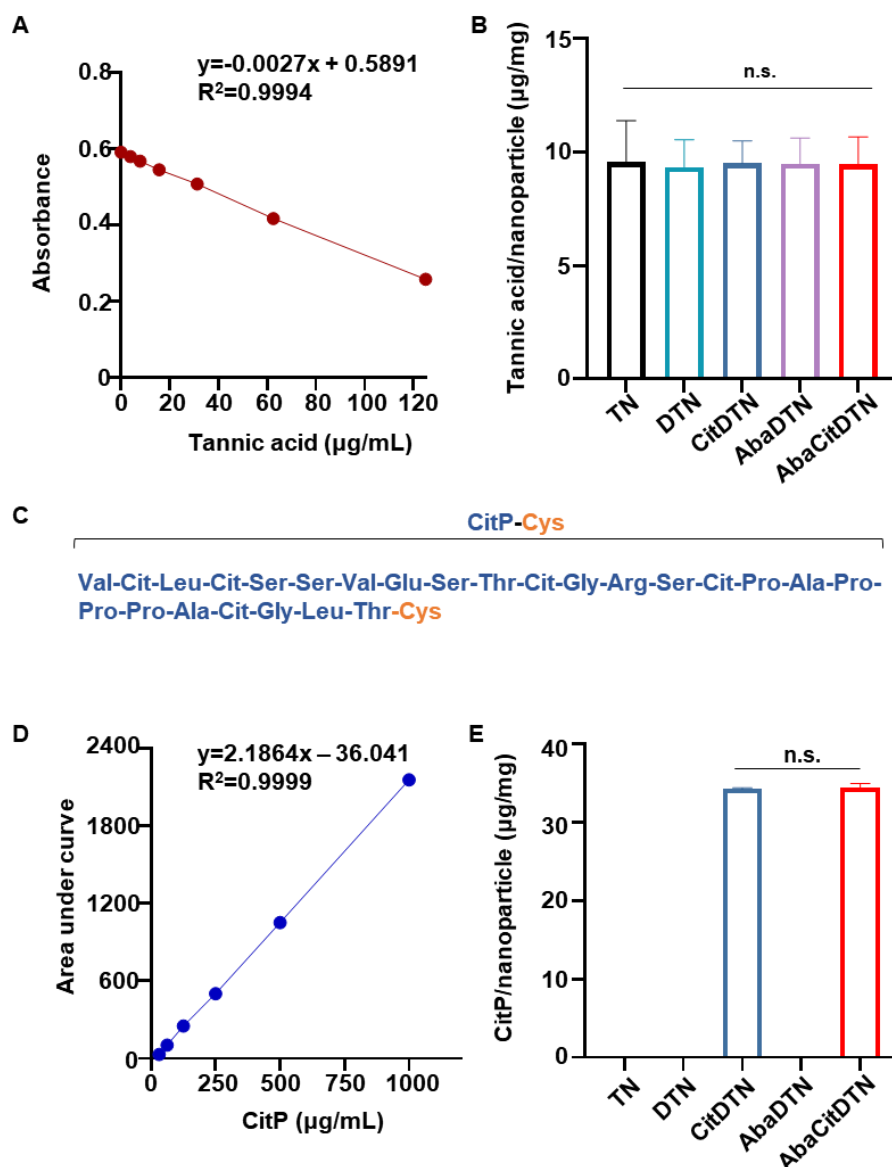

Figure 5. Quantification of tannic acid and CitP in nanoparticles. A) Standard curve of tannic acid. B) Amount of tannic acid in nanoparticles, as quantified by DPPH assay. All statistical data are presented as mean $\pm$ SD

(n=3; n.s., not significant). C) Amino acid sequence of CitP-Cys. D) Standard curve of CitP. E) Amount of CitP loaded in nanoparticles, as quantified by HPLC. All statistical data are presented as mean ± SD (n=3; n.s., not significant).

4.3.2. Cellular uptake of nanoparticles and CD80/CD86-blocking study

The cellular uptake by and CD80/CD86-blocking activity of nanoparticles against DC were evaluated by confocal microscopy and flow cytometry. Confocal imaging revealed negligible binding of DTN or CitDTN to BMDC at 4 h and 24 h after treatment of BMDC with nanoparticles (Figure 6A). In contrast, treatment with AbaDTN and AbaCitDTN resulted in strong binding of nanoparticles on the surface of BMDC by 4 h post-treatment. At 24 h post-treatment, AbaDTN and AbaCitDTN were observed to co-localize with LysoTracker, indicating that these nanoparticles had undergone endocytosis into BMDC. Consistent with the confocal imaging results, flow cytometry revealed that the fluorescence intensity of AbaCitDTN-treated BMDC was 2.73-fold higher than that of CitDTN-treated BMDC. The proposed mechanism underlying CD80 and CD86-mediated DC binding is shown in Figure 6B. Upon blockade of CD80 or CD86, the binding ability of AbaCitDTN was reduced by 18.7% and 21.3%, respectively. Blockade of both CD80 and CD86 completely inhibited the binding ability of AbaCitDTN on DC, such that the fluorescence intensity was similar to that seen in the CitDTN-treated group (Figure 6C, D).
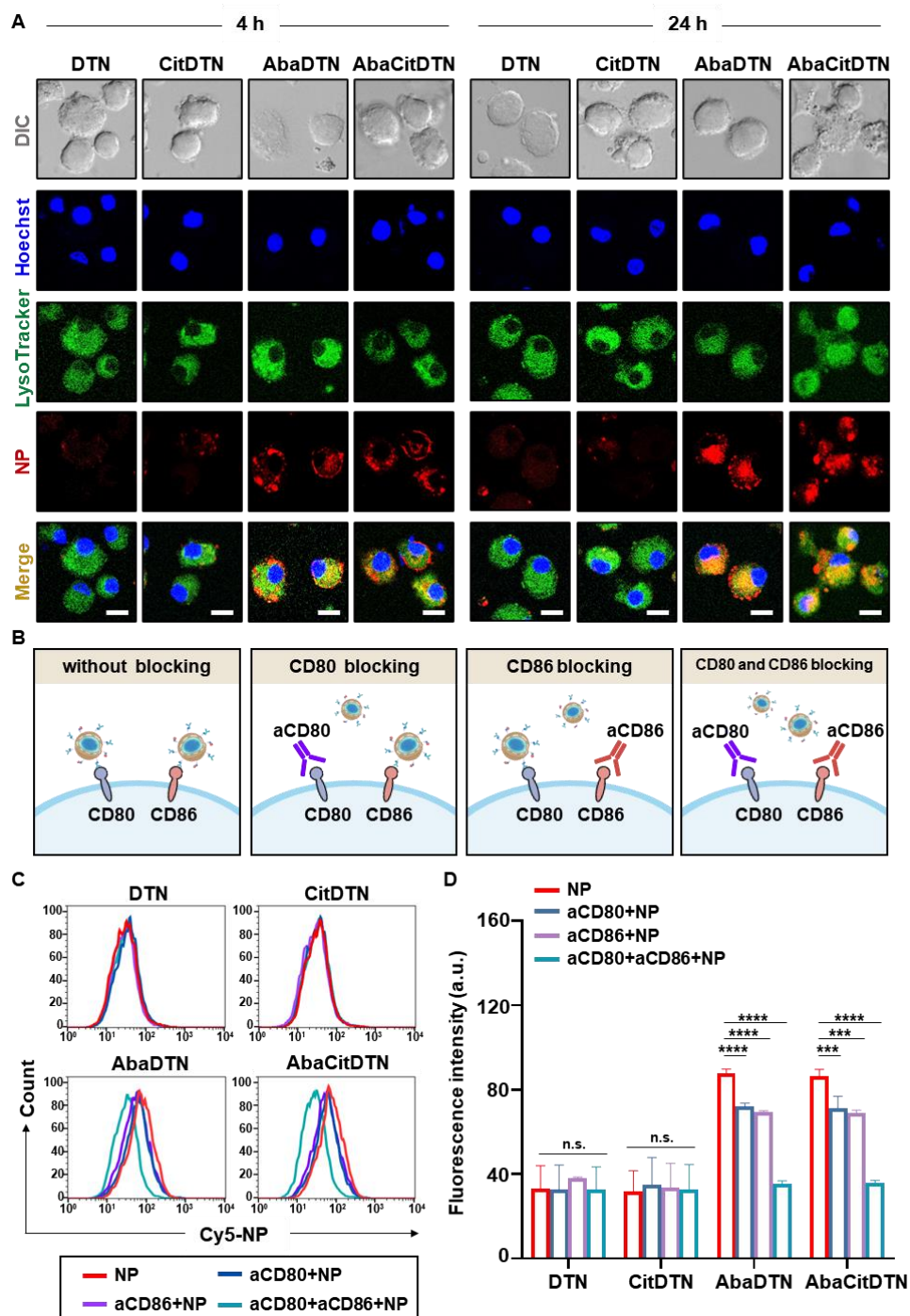
Figure 6. DC targeting and endocytosis of AbaCitDTN via co-stimulatory molecules. A) Nanoparticles were labeled with Cy5 (red) and lysosomes were marked by LysoTracker (green). Intracellular trafficking of nanoparticles in DC was visualized by confocal microscopy after 4 h and 24 h incubation with each nanoparticle. Scale bar: 10 μm. B) Schematic illustration of CD80 and CD86-mediated endocytosis. C) Binding ability of nanoparticles with or without CD80 or CD86 blockade was quantified by

flow cytometry. D) The fluorescence intensity of DC-bound nanoparticles was quantified. All statistical data are presented as mean ± SD (n=3; ***p<0.001, ****p<0.0001, n.s., not significant).

4.3.3. In vitro tolerogenic DC induction and ROS-scavenging effect

Treatment of BMDC with AbaCitDTN could induce tolerogenic DC and scavenge ROS in DC (Figure 7A, B). To evaluate tolerogenic DC induction, the expression levels of the surface markers, CD86, CD80, and CD40, and the intracellular levels of the pro-inflammatory cytokine, TNF-α, and the anti-inflammatory cytokine, TGF-β, were measured by flow cytometry. AbaCitDTN significantly reduced the expression levels of CD86, CD80, and CD40 by 70.1% (Figure 7C), 57.8% (Figure 7D), and 82.0% (Figure 7E), respectively, compared with those seen in CitDTN-treated cells. Moreover, AbaCitDTN decreased the expression levels of CD86, CD80, and CD40 by 58.3%, 55.8%, and 68.9%, respectively, compared to AbaCitDLN treatment, indicating the effect of tannic acid core for tolerogenic DC induction. Similarly, the intracellular level of TNF-α was decreased by 74.9% and 64.9% upon treatment with AbaCitDTN compared with CitDTN and AbaCitDLN, respectively (Figure 7F). AbaCitDTN treatment increased the expression of TGF-β by 1.62-fold more than CitDTN treatment (Figure 7G). Confocal imaging revealed that TNF-α expression was reduced in AbaCitDTN-treated DC compared with the CitDTN group (Figure 7I). To evaluate the effect of nanoparticles on radical scavenging in BMDC, nitric oxide concentration and intracellular ROS levels were measured. Compared to the CitDTN and AbaCitDLN groups, AbaCitDTN significantly reduced the secretion of nitric oxide by 75.4% and 60.8%, respectively (Figure 7H). Confocal imaging showed that the fluorescence of intracellular ROS was decreased in AbaCitDTN-treated cells compared to the untreated group (Figure 7J).
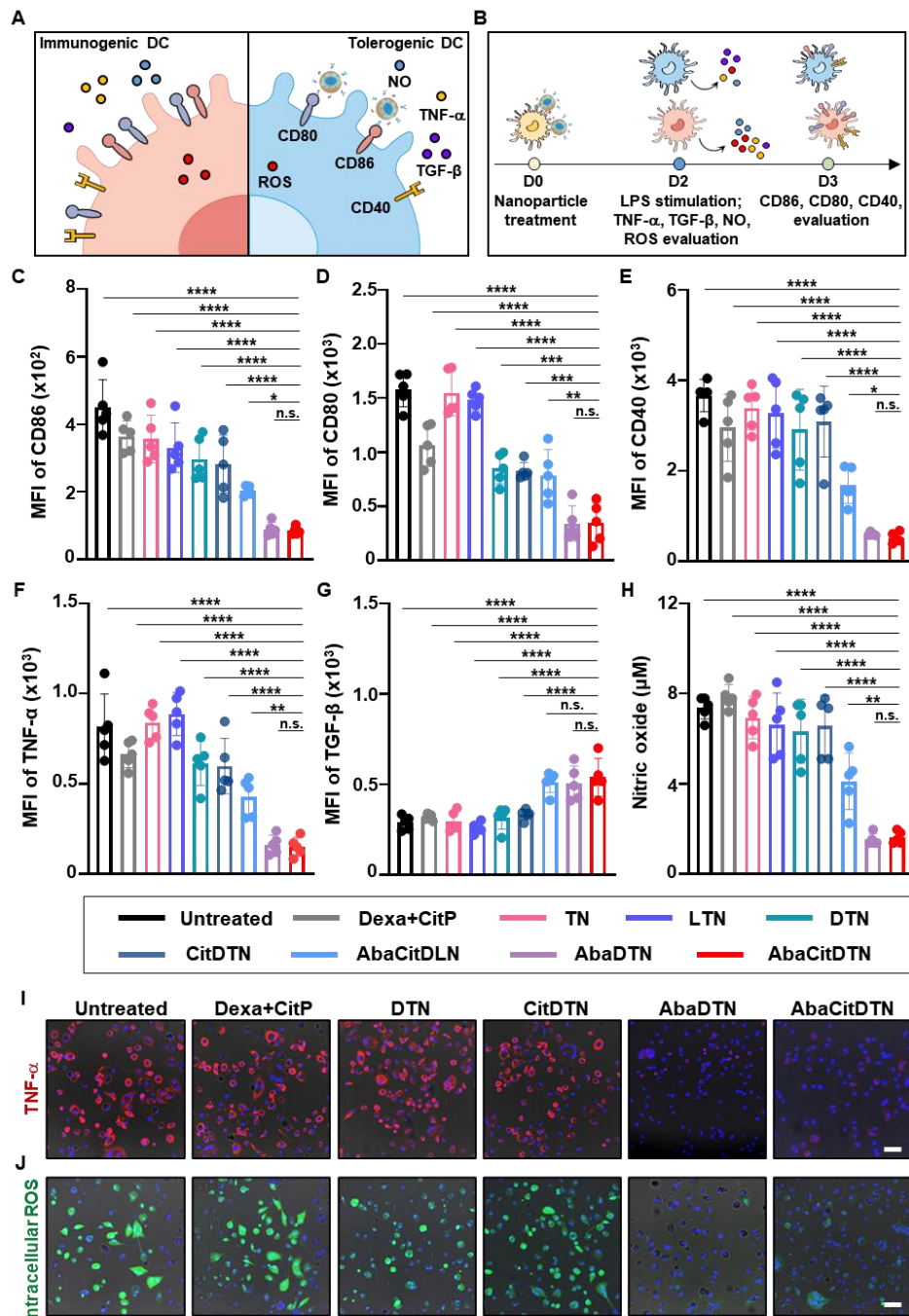
Figure 7. Tolerogenic DC induction by nanoparticles. A) Representative molecular markers of immunogenic DC and tolerogenic DC are illustrated. B) Schematic illustration of AbaCitDTN-mediated tolerogenic DC induction. C-E) The surface expression levels of CD86 C), CD80 D), and CD40 E) were measured by flow cytometry. F) The intracellular expression level of the pro-inflammatory cytokine TNF-α was evaluated by flow cytometry. G) The intracellular expression level of the anti-inflammatory cytokine TGF-β

was assessed using flow cytometry. H) Nitric oxide levels were evaluated using Griess reagent upon LPS stimulation. All statistical data are presented as mean ± SD (n=5; **$p<0.01$, ***$p<0.001$, ****$p<0.0001$, n.s., not significant). I) Expression of TNF-α in DC was visualized by confocal microscopy. Scale bar: 50 μm. J) Confocal imaging of intracellular ROS levels, as visualized using CM-H2DCFDA. Scale bar: 50 μm.

AbaCitDTN treatment suppressed the inflammatory signaling pathway through its tannic acid core-mediated ROS scavenging effect, as illustrated in Figure 8A. To evaluate this effect, the expression levels of nuclear factor kappa-light-chain-enhancer of activated B cells (NF-κB) translocation, hypoxia-inducible factor-1α (HIF1α), inducible nitric oxide synthase (iNOS), and cyclooxygenase-2 (COX-2) were assessed. AbaCitDTN-treated BMDC exhibited significantly decreased nuclear NF-κB p65 expression levels compared to AbaCitDLN-treated cells (Figure 8B, 8C). Furthermore, AbaCitDTN treatment resulted in a 54.1%, 75.8%, and 82.9% reduction in the mRNA expression levels of HIF1α, iNOS, and COX-2, respectively, compared to AbaCitDLN-treated cells (Figure 8D).
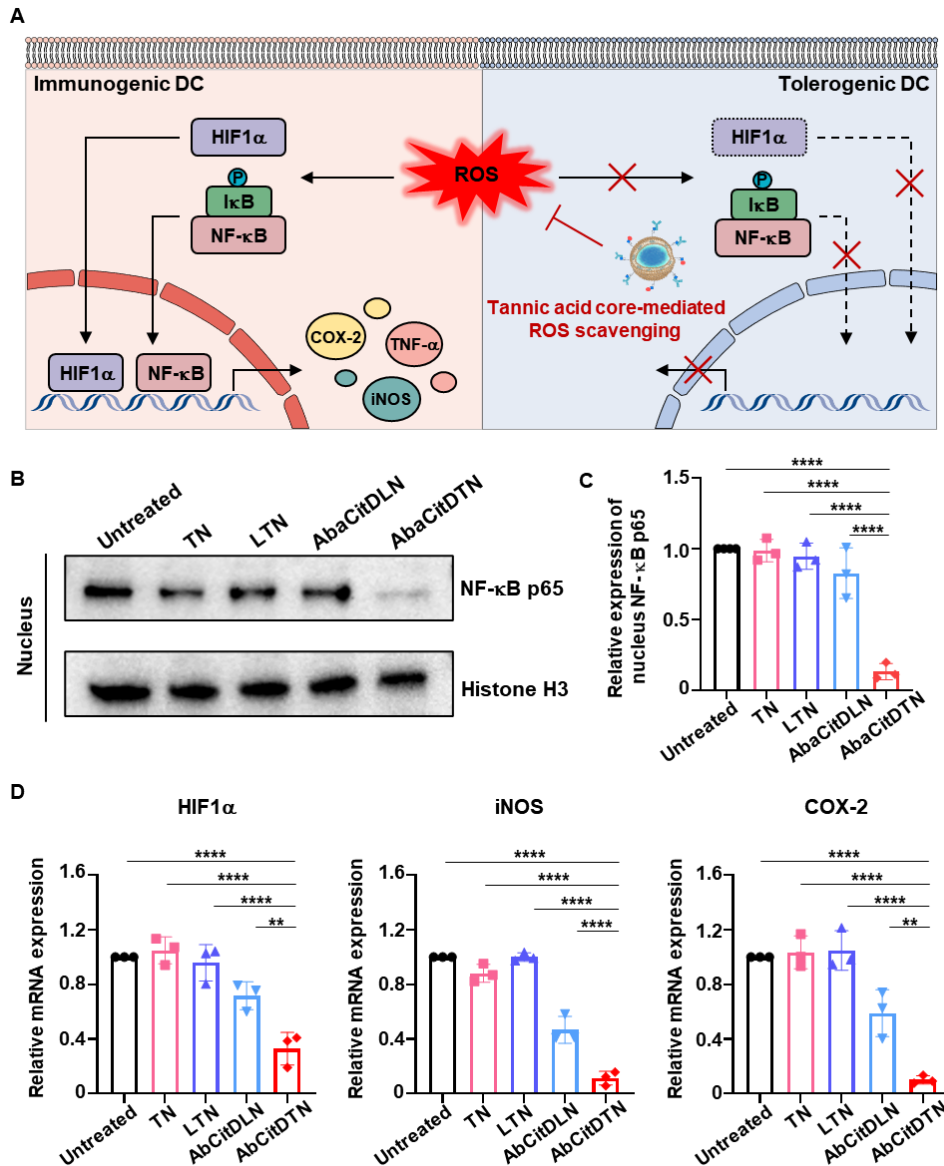
Figure 8. Inhibition of inflammatory signaling pathway by nanoparticles through tannic acid core-mediated ROS scavenging. A) Schematic illustration of the ROS scavenging effect mediated by the tannic acid core of the nanoparticles. B) The expression level of NF-κB p65 in the nucleus was evaluated by western blotting. C) The relative expression of NF-κB p65 was quantified. D) The expression levels of HIF1α, iNOS, and COX-2 were measured using RT-PCR. All statistical data are presented as mean ± SD (n=3; ** $p<0.01$, **** $p<0.0001$).

4.3.4. Inhibition of co-stimulatory molecule interaction, T-cell expansion, and IL-2 secretion

Co-culture of nanoparticle-treated BMDC with T cells blocked the

interaction between CD80/CD86 and CD28, as illustrated in Figure 9A. Confocal imaging revealed that negligible nanoparticles existed at the interface between DC and T cells in the CitDTN-treated groups (Figure 9B), whereas strong fluorescence signals could be observed for AbaCitDTN. These signals were specific to the surface of DC, not T cells, indicating the DC-specific binding ability of AbaCitDTN. To mimic co-stimulatory molecule activation in vitro, anti-CD3 antibody and CD80-Fc protein coated on a plate were used to activate T cells (Figure 9C). Pre-incubation of the plate with either free abatacept or AbaCitDTN resulted in lower expansion indexes of CD4$^+$ T cells (Figure 9D) and CD8$^+$ T cells (Figure 9E) compared to untreated and CitDTN-pre-treated plates. The free abatacept-treated group showed a 67.3% reduction in the expansion indexes of CD4$^+$ T cells (Figure 9F) and a 68.6% reduction in the expansion indexes of CD8$^+$ T cells (Figure 9G) compared to the untreated group. Furthermore, free abatacept treatment significantly reduced the secretion of IL-2 by 99.8% compared to the untreated group (Figure 9H). The expansion indexes of CD4$^+$ T cells and CD8$^+$ T cells treated with AbaCitDTN were decreased by 58.3% and 60.8%, respectively, compared to those in the CitDTN-treated group. The AbaCitDTN-treated group also reduced the secretion of IL-2 by 99.7% compared to that seen in the CitDTN group.
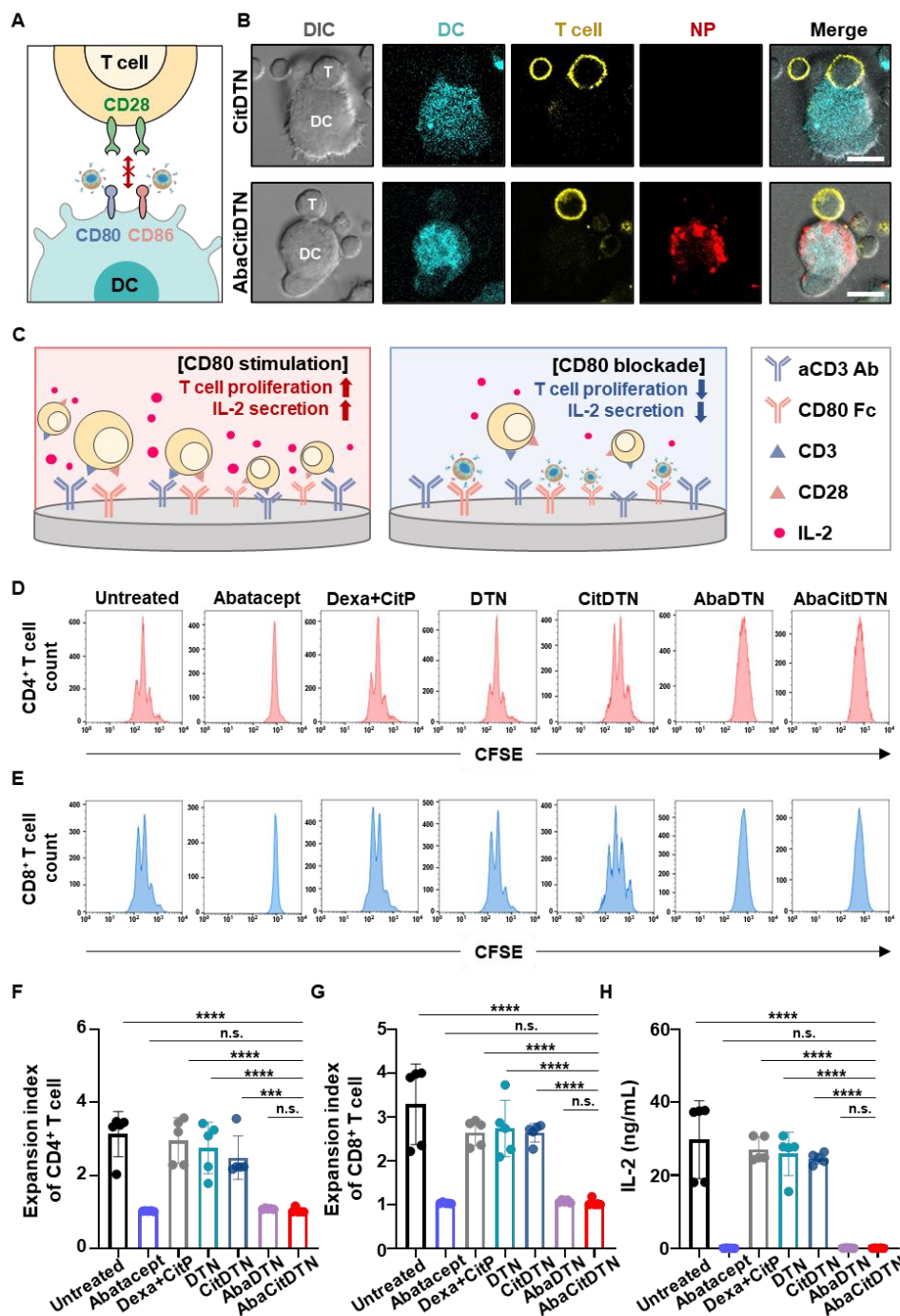
Figure 9. Co-stimulatory signal blockade by nanoparticles. A) Illustration of co-stimulatory signal blockade between DC and T cells. B) DC-specific binding with AbaCitDTN interrupted the interaction between DC and T cells, as visualized by confocal microscopy. Scale bar: 10 μm. C) Schematic illustration of the CD80 blockade study. D, E) Representative flow cytometry data of CFSE assay for CD4$^+$ T cells D) and CD8$^+$ T cells E). F, G) Expansion indexes of CD4$^+$ T cells F) and CD8$^+$ T cells G) were

evaluated by flow cytometry. H) The IL-2 secretion level from splenocytes was evaluated by ELISA. All statistical data are presented as mean ± SD (n=5; ***$p<0.001$, ****$p<0.0001$, n.s., not significant).

4.3.5. In vitro suppression of CitP-specific splenocytes by AbaCitDTN

The in vitro suppression of CitP-specific splenocytes was evaluated by IFN-γ ELISpot and cytokine ELISA. In order to investigate the role of CitP as auto-antigen, ovalbumin (OVA) was introduced as an irrelevant antigen for the studies. Splenocytes isolated from CIA mice were treated with various nanoparticles and stimulated with CitP or OVA$_{323-339}$ in vitro (Figure 10A). The AbaCitDTN-treated group was decreased by 53.7% in the population of IFN-γ-secreting splenocytes compared to that of the AbaOVADTN-treated group upon CitP stimulation, while negligible IFN-γ-secreting cells could be observed upon OVA$_{323-339}$ stimulation (Figure 10B, C). Moreover, AbaCitDTN treatment showed a 51.2% (Figure 10D), 63.6% (Figure 10E), and 82.2% (Figure 10F) decrease in IL-6, TNF-α, and GM-CSF secretion compared to those of the AbaOVADTN-treated group upon CitP stimulation. Few cytokines were detected in all nanoparticle-treated groups upon OVA$_{323-339}$ stimulation.
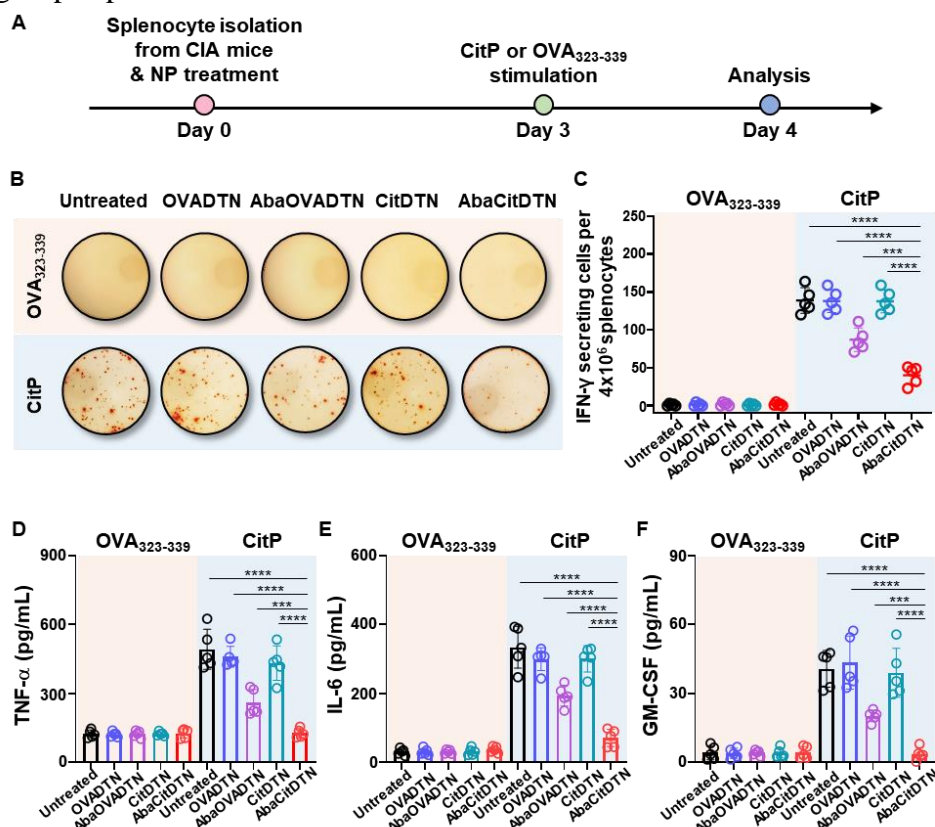

Figure 10. Suppression of CitP-specific immune responses by nanoparticles at cellular level. A) The experimental schedule for the suppression of CitP-specific splenocytes by AbaCitDTN is presented. B) Representative spots of

IFN-γ-secreting cells after stimulation with OVA$_{323-339}$ or CitP. C) Immune responses against OVA$_{323-339}$ and CitP were analyzed using IFN-γ ELISpot. D-F) Cytokine levels, including TNF-α D), IL-6 E), and GM-CSF F) after stimulation with OVA$_{323-339}$ or CitP were measured by ELISA. All statistical data are presented as mean ± SD (n=5; ***$p<0.001$, ****$p<0.0001$).

4.3.6. In vivo biodistribution of nanoparticles

The in vivo biodistribution of nanoparticles was monitored by fluorescence molecular imaging and an imaging system. Mice treated with Cy5-labeled AbaDTN and AbaCitDTN showed greater fluorescence signals in the inguinal lymph nodes compared with the Cy5-labeled DTN and CitDTN groups (Figure 11A). In the right and left inguinal lymph nodes, the distributions of AbaDTN and AbaCitDTN peaked at 12 h post-injection (Figure 11B, C).

Three-dimensional reconstructed imaging, which integrated IVIS optical and micro-CT imaging, revealed that there was higher accumulation of AbaDTN and AbaCitDTN than DTN and CitDTN in the inguinal lymph nodes of mice at 12 h post-treatment (Figure 11D). Lymph node staining revealed that there was higher co-localization of AbaDTN and AbaCitDTN with CD11c$^+$ DC in the inguinal lymph nodes (Figure 11E).
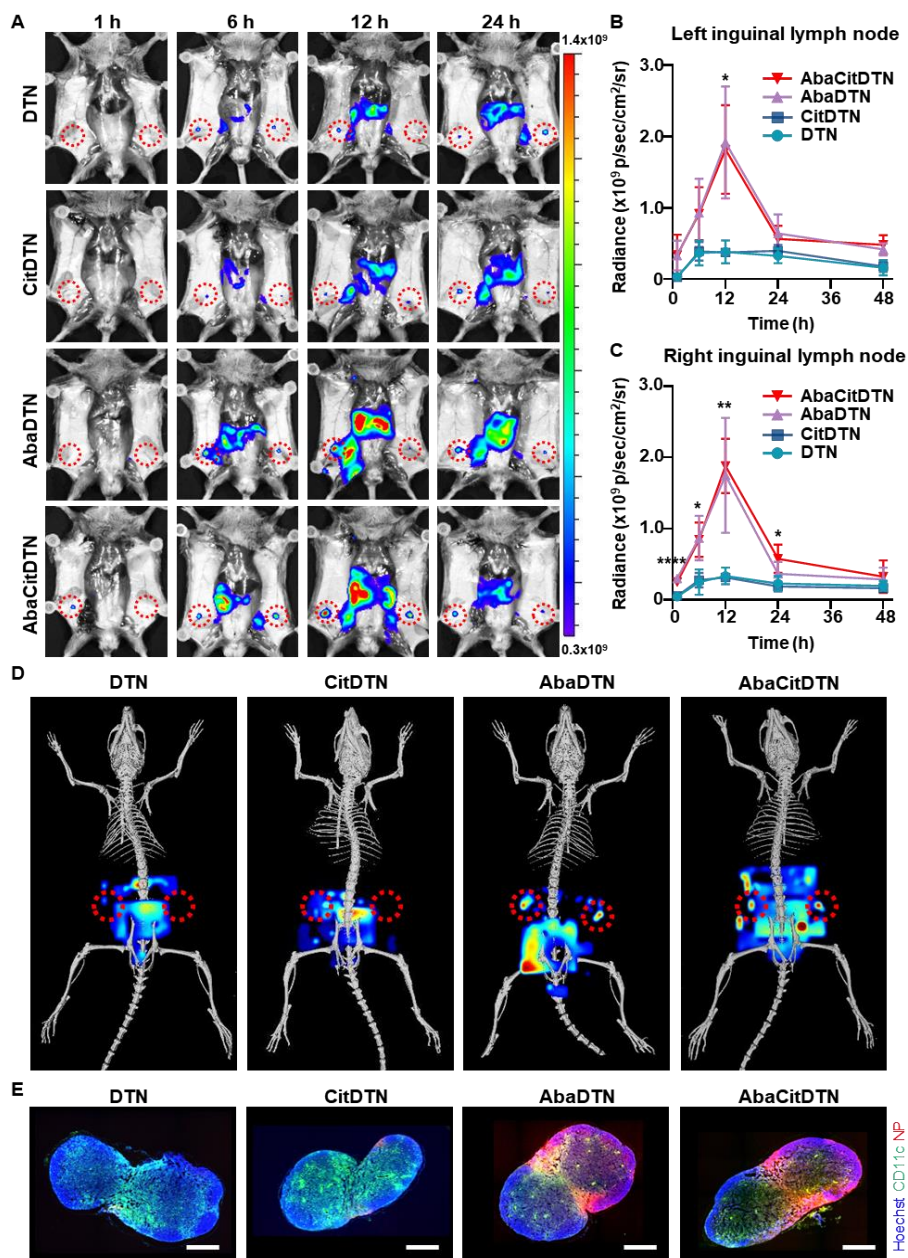
Figure 11. In vivo lymph node targeting ability of AbaCitDTN. A) DBA/1 mice were subcutaneously administered with Cy5-labeled nanoparticles at the center of the lower back. Fluorescence intensity in inguinal lymph nodes over time was observed by IVIS spectrum analysis. Quantification of fluorescence in left B) and right inguinal lymph nodes C) at different time points. All statistical data are presented as mean ± SD (n=3; *$p<0.05$, **$p<0.01$, ****$p<0.0001$). D) Molecular imaging of lymph nodes at 12 h post-injection was visualized using IVIS spectrum analysis combined with micro-CT imaging. E) Immunofluorescence imaging of nanoparticle accumulation in inguinal lymph nodes at 12 h post-injection. Scale bar: 0.5 mm.

4.3.7. Prophylactic efficacy of tolerogenic nanoparticles in CIA mice

To evaluate the prophylactic efficacy of AbaCitDTN in treating rheumatoid arthritis, CII-induced arthritis (CIA) was established in DBA/1 mice. To generate this model, DBA/1 mice were injected subcutaneously with free Dexa and CitP or various nanoparticle preparations every week for a total of four times, beginning on day 0 (Figure 12A). AbaCitDTN treatment led to a significant reduction in clinical score at the end of the study (Figure 12B). Moreover, AbaCitDTN-treated CIA mice showed a minimal increase in hind paw thickness throughout the treatment period, with hind paw thickness increasing by 81.0%, 77.3%, 76.7%, and 69.7% less than that in the CitDTN, AbaDTN, AbaOVADTN, and AbaCitDLN groups, respectively, by the end of the study (Figure 12C). Additionally, hind paw photographs demonstrated that AbaCitDTN-treated CIA mice exhibited higher therapeutic efficacy than the other treatment groups (Figure 12D).
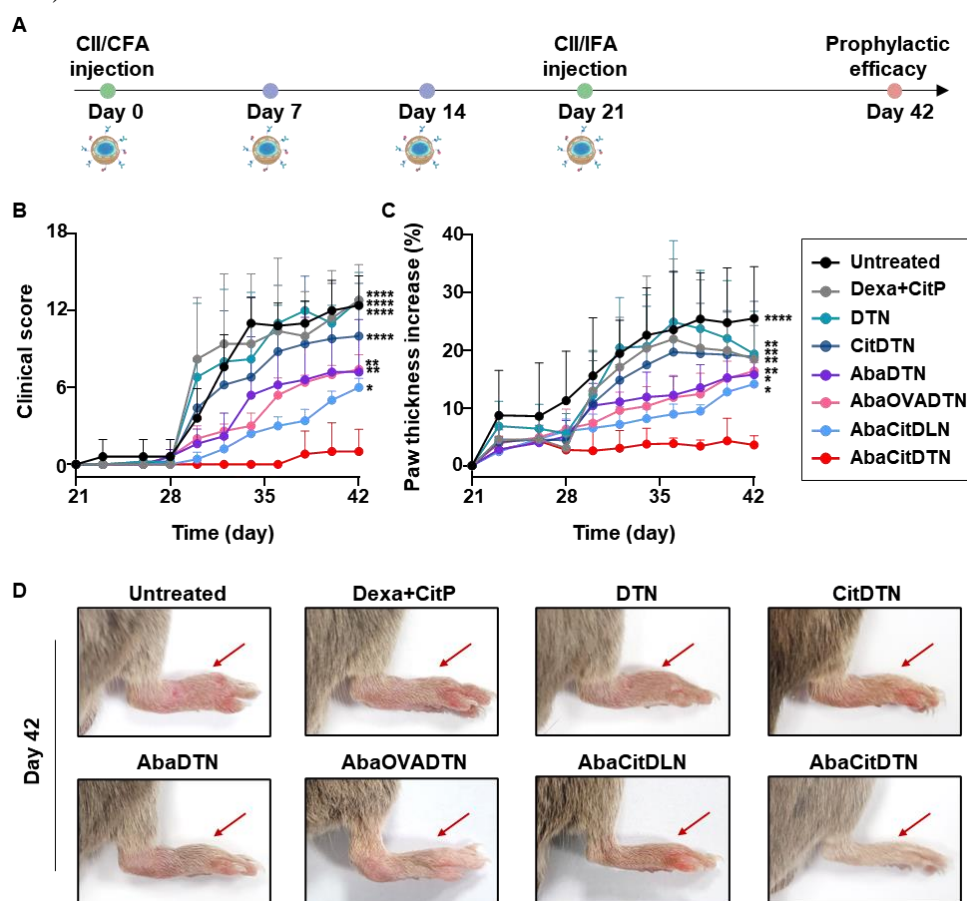

Figure 12. Prophylactic efficacy of nanoparticles in CIA mouse model. A) Experimental schedule for CIA mouse model establishment and nanovaccine administration. B) Clinical scores were assessed every other day using a scoring system as follows: 0, normal; 1, mild redness and swelling limited to the toes; 2, moderate redness and swelling of ankle joints

or wrists; 3, enhanced redness and swelling of entire paws; 4, severe swelling of entire paws or ankylosed paws and toes. C) Paw thickness was measured throughout the in vivo experiment. D) Representative images of hind paws in each treatment group. All statistical data are presented as mean ± SD (n=5; *p<0.05, **p<0.01, ****p<0.0001).

The hind paw and joint architecture were observed via micro-CT. Three-dimensional imaging showed that AbaCitDTN-treated mice exhibited decreased bone erosion, whereas untreated and CitDTN-treated mice suffered from severe bone erosion in hind paws and knee joints (Figure 13A). The bone BV/TV, BS/BV, and BMD of femurs from AbaCitDTN treated mice were 2.68-fold, 0.63-fold, and 1.09-fold, respectively, compared to those of CitDTN-treated mice (Figure 13B). Similarly, these three bone parameters of tibia from AbaCitDTN-treated mice were 1.90-fold, 0.61-fold, and 1.08-fold, respectively, compared to the CitDTN group (Figure 13C).
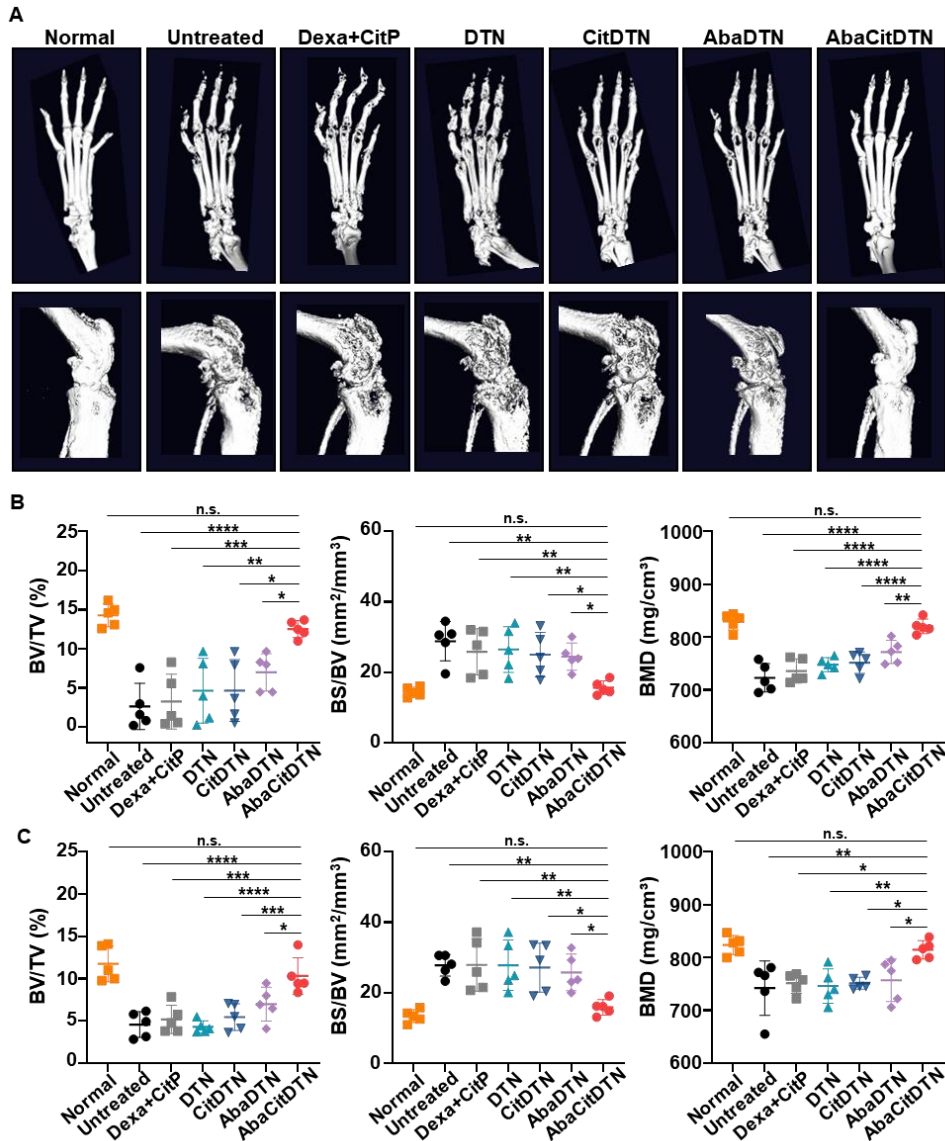
Figure 13. Bone architecture and bone erosion observation. A) Experimental schedule for CIA mouse model establishment, nanovaccine administration, and micro-CT analysis. B) Three-dimensional imaging of hind paw and knee joint architectures, as observed by micro-CT imaging. Quantitative analyses of bone erosion for femur C) and tibia D) were based on BV/TV, BS/BV, and BMD. All statistical data are presented as mean $\pm$ SD (n=5; $*p<0.05$, $**p<0.01$, $***p<0.001$, $****p<0.0001$, n.s., not significant).

Next, the pro-inflammatory cytokine and chemokine levels in the serum and synovial fluid were evaluated on day 42 (Figure 14A). Consistent with the in vivo efficacy results, the serum levels of pro-inflammatory cytokines and chemokines, such as IL-6, IFN-γ, and CCL2, were significantly reduced

in the AbaCitDTN-treated group; these levels were reduced by 57.1% (Figure 14B), 91.3% (Figure 14C), and 63.8% (Figure 14D), respectively, compared to those in the CitDTN group. In addition, AbaCitDTN treatment led to dramatic declines of the IL-6, IL-1β, TNF-α, and CCL2 levels in synovial fluid; these levels were reduced by 81.5% (Figure 14E), 96.0% (Figure 14F), 43.2% (Figure 14G), and 70.9% (Figure 14H), respectively, compared to those in CitDTN-treated CIA mice.
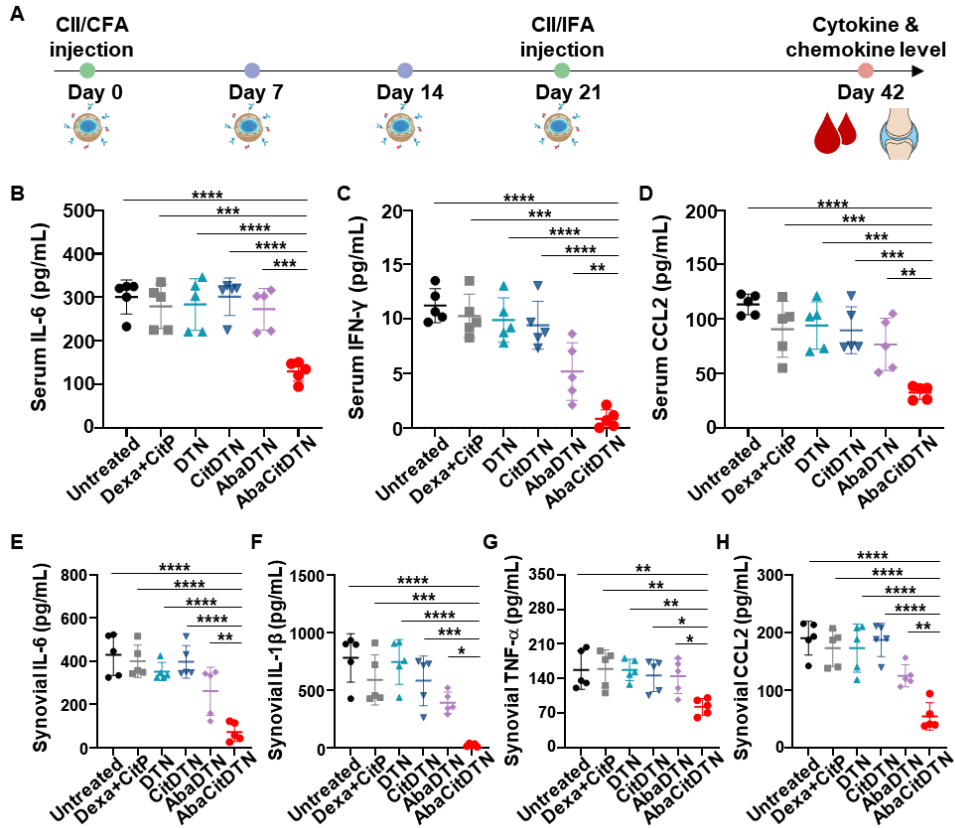
Figure 14. Cytokine and chemokine evaluation in serum and synovial fluid. A) Experimental schedule for CIA mouse model establishment, nanovaccine administration, and cytokine and chemokine level evaluation. B-D) Serum levels of pro-inflammatory cytokines and chemokines, including IL-6 B), IFN-γ C), and CCL2 D), were measured by ELISA. E-H) Synovial fluid levels of pro-inflammatory cytokines and chemokines, including IL-6 E), IL-1β F), TNF-α G), and CCL2 H), were measured by ELISA. All statistical data are presented as mean ± SD (n=5; *$p<0.05$, **$p<0.01$, ***$p<0.001$, ****$p<0.0001$).

4.3.8. Antigen-specific regulation in CIA mice

To assess the effects of AbaCitDTN on antigen-specific immune responses in CIA mice, the autoantibody level in serum and the population of antigen-responsive IFN-γ-secreting splenocytes were quantified. The serum level of anti-CitP IgG in AbaCitDTN-treated CIA mice was reduced

by 83.4% and 81.5% compared to that in the CitDTN and AbaDTN groups, respectively (Figure 15B). The serum level of anti-CII IgG in the AbaCitDTN-treated group was reduced by 63.8% and 62.1% compared to those of CitDTN and AbaDTN-treated mice, respectively (Figure 15C). Thus AbaCitDTN-treated mice developed strong immune tolerance with significant CitP and CII specificity. Under CitP or CII stimulation, the AbaCitDTN-treated group exhibited lower populations of CitP- and CII-specific IFN-γ-secreting splenocytes compared to the other groups, demonstrating that AbaCitDTN effectively reduced antigen-specific immune responses toward RA (Figure 15D, E).
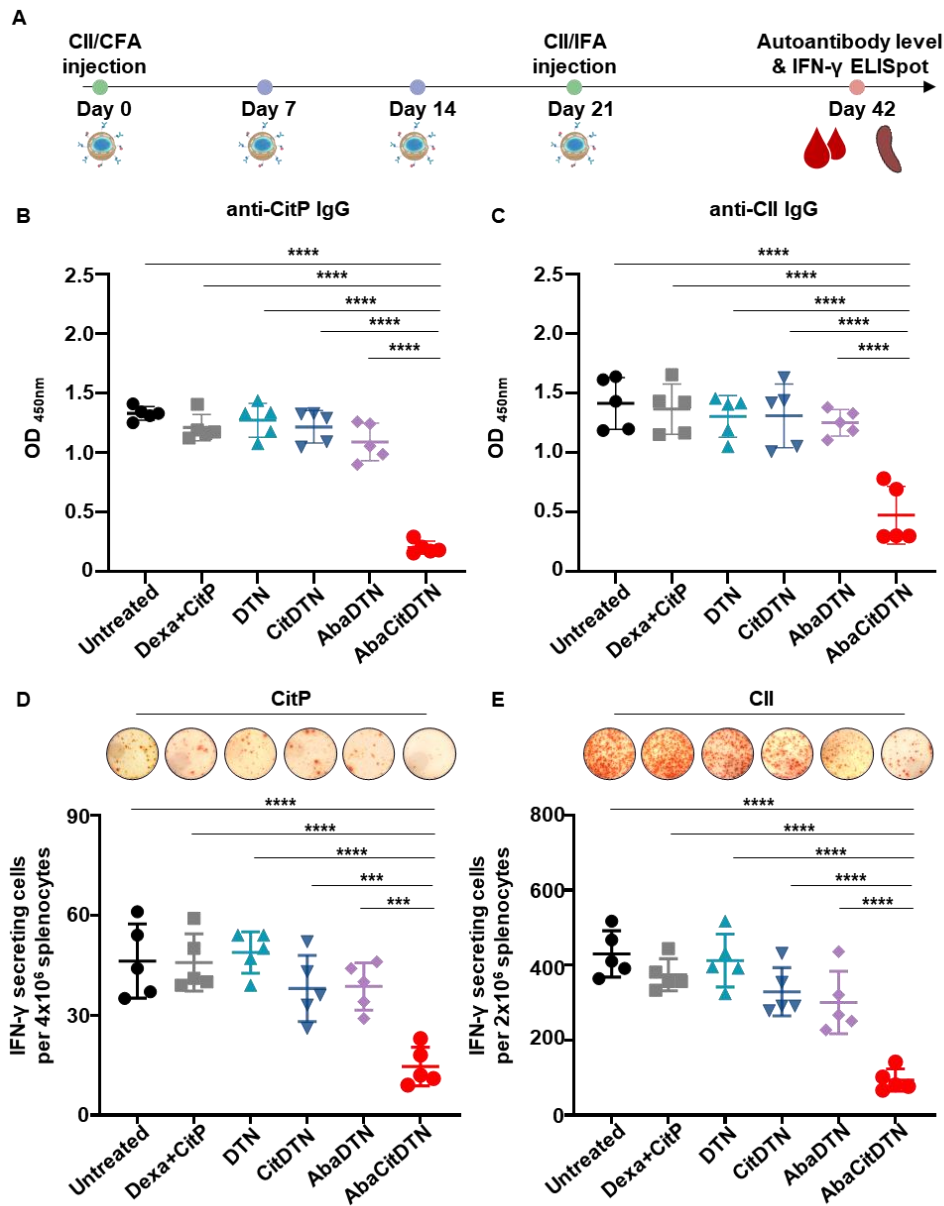
Figure 15. Regulation of antigen-specific immune responses by the tolerogenic vaccine. A) Experimental schedule of CIA mouse model establishment, nanovaccine administration, and analysis of antigen-specific immune responses. Humoral immune responses were evaluated by measuring anti-CitP IgG B) and anti-CII IgG C) in serum. Antigen-specific immune responses against CitP D) and CII E) were analyzed by IFN-γ ELISpot. All statistical data are presented as mean ± SD (n=5; ***p<0.001, ****p<0.0001).

4.3.9. Immune cell profiles in CIA mice

To study the mechanism underlying the prophylactic efficacy of AbaCitDTN in CIA model mice, the T cell polarization on day 42 was analyzed by flow cytometry. Treatment with AbaCitDTN resulted in a significant increase of the Treg proportion in the spleen, which was 4.80-fold higher than that in the CitDTN-treated group (Figure 16B, F). In addition, AbaCitDTN treatment yielded the lowest proportion of IL-17A-expressing CD4$^+$ T cells, IFN-γ-secreting CD4$^+$ T cells, and IFN-γ-secreting CD8$^+$ T cells; these levels were reduced by 72.2% (Figure 16C, G), 89.2% (Figure 16D, H), and 86.4% (Figure 16E, I), respectively, compared to those in the CitDTN-treated group.
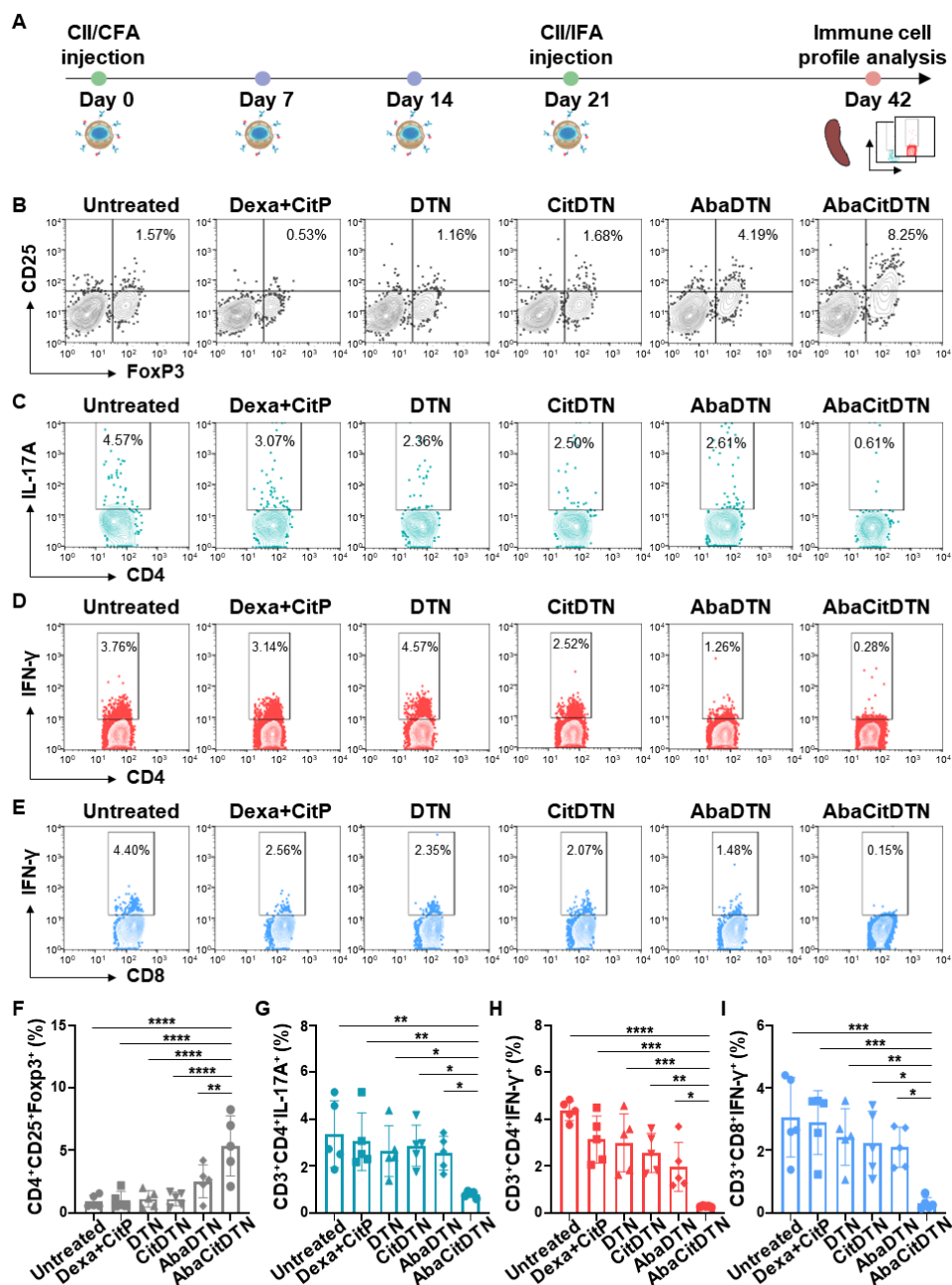
Figure 16. Immune cell profiling in lymphoid organs. A) Experimental schedule of CIA mouse model establishment, nanovaccine administration, and immune cell profiling in lymphoid organs. Populations of $CD4^+CD25^+Foxp3^+$ Tregs B, F), $CD3^+CD4^+IL\text{-}17A^+$ T cells C, G), $CD3^+CD4^+IFN\text{-}\gamma^+$ T cells D, H), and $CD3^+CD8^+IFN\text{-}\gamma^+$ T cells E, I) were determined by flow cytometry. All statistical data are presented as mean ± SD (n=5; *$p<0.05$, **$p<0.01$, ***$p<0.001$, ****$p<0.0001$).

4.3.10. Amelioration of joint destruction by AbaCitDTN

The subcutaneous injection of AbaCitDTN reduced inflammation and maintained the structure of bone and cartilage in knee joints. Immunofluorescence imaging showed that few neutrophils were infiltrated into knee joints of the AbaCitDTN-treated group, while considerable infiltration of neutrophils was observed in knee joints of the CitDTN and AbaDTN groups (Figure 17A). H&E-stained images demonstrated that AbaCitDTN ameliorated inflammation and maintained the bone integrity of CIA mice, whereas the other formulations did not prevent joint inflammation or bone erosion (Figure 17B). Inflammation and bone erosion were both scored according to H&E staining; the scores of AbaCitDTN-treated mice were reduced by 80.0% (Figure 17E) and 81.8% (Figure 17F), respectively, compared to those of the CitDTN-treated group. Safranin O (Figure 17C) and toluidine blue staining image analysis (Figure 17D) revealed that AbaCitDTN protected cartilage from erosion, as the cartilage erosion score was reduced by 80.0% (Figure 17G) compared to that of the CitDTN group.

Figure 17. Histological analysis of knee joints. At day 42 after the first administration of nanovaccines, mice were sacrificed and knee joints were isolated for histological analysis. A) Immunofluorescence imaging of knee joint- infiltrated neutrophils. Scale bar: 600 μm. Representative images of paraffin-embedded knee joint tissues of CIA mice stained with H&E B), safranin O C), and toluidine blue D). Scale bar: 600 μm. Inflammation E) and bone erosion F) were scored from H&E-stained images. Cartilage

erosion G) was scored from safranin O-stained images. All statistical data are presented as mean ± SD (n=4; *$p<0.05$, **$p<0.01$, ***$p<0.001$, ****$p<0.0001$, n.s., not significant).

4.3.11. Maintenance of defensive immune responses after tolerogenic vaccination

The impact of nanovaccine administration on defensive immune responses against irrelevant antigens was investigated using a hemagglutinin model system. After four administrations of nanovaccines, hemagglutinin/CFA and hemagglutinin/IFA were injected into DBA/1 mice on day 21 and day 35 after the first nanovaccine injection (Figure 18A). The immune response against hemagglutinin was evaluated by measuring anti-hemagglutinin IgG in serum and analyzing hemagglutinin-specific IFN-γ-secreting cells. Nanovaccine administration did not impair the development of neutralizing antibodies and IFN-γ secreting cells against hemagglutinin (Figure 18B-D).
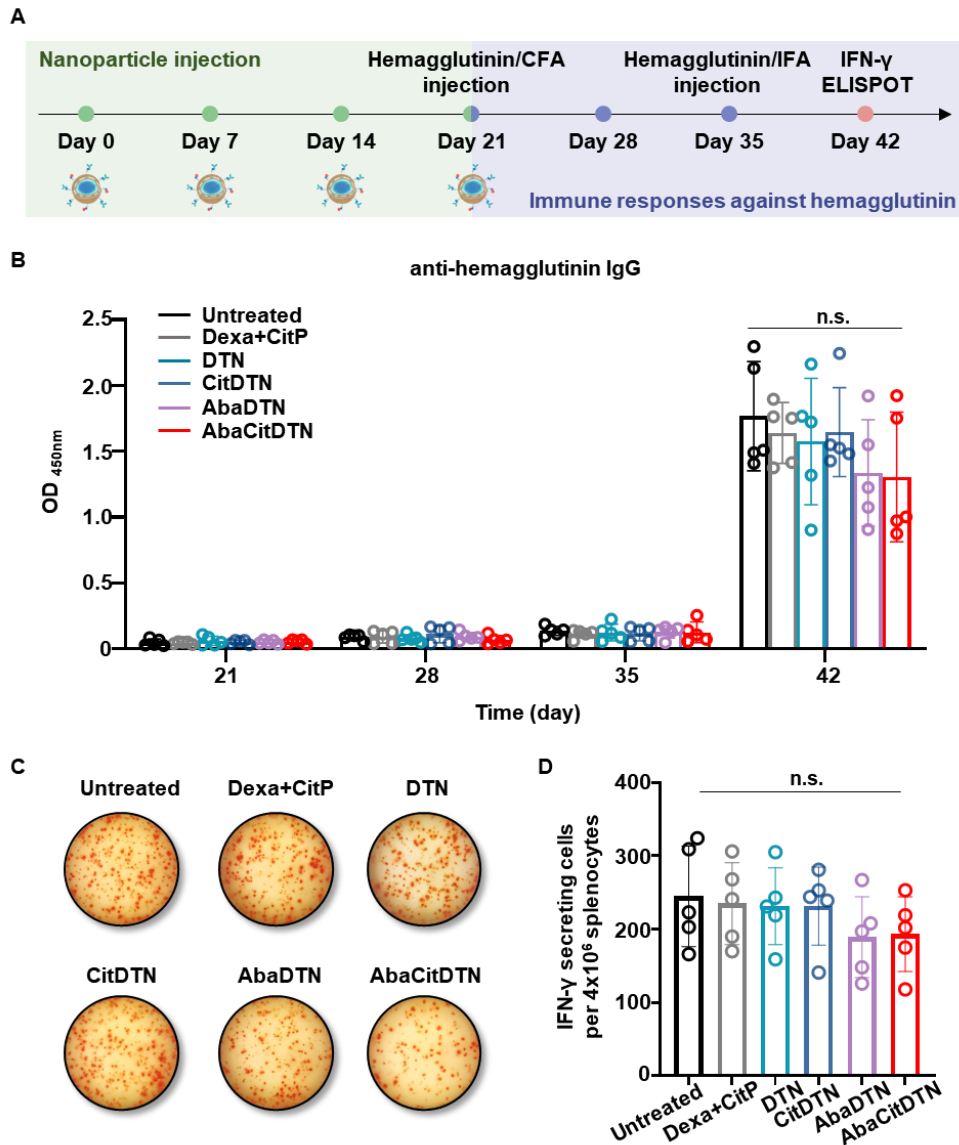
Figure 18. Defensive immune responses against hemagglutinin. A) Experimental schedule for the administration of the nanovaccine and induction of immune response against hemagglutinin. B) Humoral immune response was evaluated by measuring anti-hemagglutinin IgG in serum. C) Representative images of IFN-γ ELISpot against hemagglutinin. D) The number of IFN-γ-secreting cells was counted. All statistical data are presented as mean ± SD (n=5; n.s., not significant).

4.4. Discussion

This research demonstrated that abatacept-mediated targeted delivery of CitP and Dexa to DC could induce antigen-specific immune tolerance and ameliorated symptoms in the CIA mouse model. APC-targeting delivery of two cargos was achieved by surface modifying CitDTN with abatacept

using a thiol-maleimide reaction. The surface binding and cellular uptake of AbaCitDTN by DC blocked the co-stimulatory interactions between DC and T cells, and further reprogrammed the DC phenotypes toward tolerogenicity. The tolerogenic reprogramming of DC by AbaCitDTN efficiently enhanced the Treg population in vivo and reduced the levels of anti-CitP IgG and anti-CII IgG in CIA model mice.

Intracellular ROS plays a crucial role in regulating immunological function, including the tolerogenic characteristics of DC [33]. Therefore, using radical scavengers, such as tannic acid, to remove ROS is a reasonable way to regulate immunological reactions. Tannic acid is a natural polyphenolic compound that contains a gallic acid moiety, making it an effective radical scavenger. Due to its antioxidant activity, tannic acid has been widely used in the treatment of inflammatory and autoimmune diseases [34]. The tannic acid core can effectively induce a tolerogenic phenotype in DC by regulating intracellular ROS. TN showed radical scavenging activity and were able to remove superoxide anions, hydroxyl radicals, and organic radical compounds that are associated with oxidative damage (Figure 3).

The radical scavenging activity of TN made it possible for AbaCitDTN to regulate intracellular inflammatory signaling in DC through ROS. ROS can increase HIF1α expression or facilitate the translocation of NF-κB p65 from the cytosol to the nucleus, both of which are associated with inflammation. These transcription factors are known to promote the expression of pro-inflammatory genes, such as iNOS and COX-2, resulting in an immunogenic phenotype in DC [35]. Thus, the elimination of ROS and induction of a tolerogenic phenotype are critical functions of TN in AbaCitDTN. AbaCitDTN demonstrated significant efficacy in removing radical species in DC, including nitric oxide and intracellular ROS, under LPS stimulation (Figure 7H, 7J).

In addition, AbaCitDTN was able to suppress the activation of NF-κB, inhibiting the translocation of NF-κB p65 to the nucleus upon LPS stimulation. However, AbaCitDLN, which lacked TN, was unable to suppress NF-κB activation (Figure 8). Although TN and LTN showed radical scavenging activity, they were not able to regulate the NF-κB signaling pathway due to the lack of the DC targeting molecule, abatacept. Moreover, AbaCitDTN downregulated the expression of the HIF1α, iNOS, and COX-2 genes. In contrast, AbaCitDLN could not sufficiently regulate the expression of those genes.

These epigenetic regulations through ROS modulation are closely linked to the induction of a tolerogenic phenotype in DC. For instance, inhibition of NF-κB activity may downregulate costimulatory molecules and pro-inflammatory cytokines [36]. AbaCitDLN was not able to effectively suppress the activation of epigenetic regulations. Therefore, it could not efficiently downregulate the expression levels of CD86, CD80, CD40, and TNF-α as AbaCitDTN (Figure 7).

CD80 and CD86 are the critical co-stimulatory molecules predominantly expressed on DC, and are upregulated upon inflammatory stimulation in autoimmune disorders. These transmembrane proteins are capable of binding CTLA4, which is a CD28 superfamily-inhibiting molecule expressed on T cells. Abatacept is a recombinant fusion protein composed of the CTLA4 extracellular domain and the Fc region of human IgG1 [8]. The results showed that DTN and CitDTN did not undergo significant cellular uptake by DC, whereas AbaDTN and AbaCitDTN exhibited strong DC binding affinity at 4 h post-treatment and showed high accumulation in lysosomes at 24 h post-treatment (Figure 6A).

To investigate the binding mechanism of abatacept-conjugated nanoparticles with DC, a CD80/CD86 blocking study was conducted. In the absence of this blockade, AbaDTN and AbaCitDTN treatment yielded higher fluorescence intensity on DC compared to DTN and CitDTN. Single blockade of CD80 or CD86 did not affect the binding of DTN and CitDTN to DC, but did decrease the fluorescence intensity of DC in the AbaDTN and AbaCitDTN groups. Moreover, dual blockade of CD80 and CD86 completely inhibited the binding ability of AbaDTN and AbaCitDTN with DC, but had no significant effect on this parameter in the DTN and CitDTN groups (Figure 6C, D). These results agree with a previous report demonstrating that abatacept can bind to CD80 and CD86 and undergo vesicular internalization via a clathrin-dependent pathway [14].

Efficient generation of tolerogenic DC is a critical step in tolerogenic therapy. The purpose of tolerogenic DC induction is to convert autoimmunity to peripheral immune tolerance toward self-antigens by enhancing disarming or deleting autoreactive T cells and promoting Treg differentiation. Thus, tolerogenic agents capable of generating tolerogenic DC are considered to be major components in this reprogramming process. The glucocorticoid drug Dexa is commonly used to alleviate inflammation in a variety of inflammatory diseases, including RA and uveitis. Due to its clinical limitations, such as low solubility and bioavailability, it has been extensively investigated for the development of nanoformulations [37, 38] Additionally, Dexa is a potent tolerogenic agent that can induce tolerogenic phenotypes among DC. It has been reported that culturing ex vivo-isolated DC with Dexa can increase anti-inflammatory cytokine secretion and reduce the expression levels of activation markers [39, 40]. The results showed that AbaCitDTN treatment significantly decreased the in vitro expression levels of DC for the surface markers, CD86, CD80, CD40, and the pro-inflammatory cytokine, TNF-α. Moreover, the expression level of the anti-inflammatory cytokine, TGF-β, was increased upon AbaCitDTN treatment (Figure 7).

Although treatment with AbaDTN and AbaCitDTN did not result in a difference in the expression levels of tolerogenic DC markers or cytokine secretion in vitro, this can be attributed to the inability of CitP, a self-antigen, to induce tolerogenic DC as effectively as Dexa. Thus, the efficacy of

AbaCitDTN in suppressing CitP-specific immune responses for RA treatment to confirm the benefits of delivering CitP and Dexa simultaneously to DC was investigated. To explore this efficacy, OVA as an irrelevant antigen was used for comparison. Upon CitP stimulation, splenocytes isolated from CIA mice without nanoparticle treatment showed a significant increase in IFN-γ, TNF-α, IL-6, and GM-CSF secretion. In contrast, negligible levels were observed in the $OVA_{323-339}$-stimulated group, suggesting that CitP acted as a self-antigen in the CIA mice model. AbaCitDTN treatment significantly suppressed CitP-specific immune responses, as demonstrated by the reduction in IFN-γ, TNF-α, IL-6, and GM-CSF secretion compared to the AbaOVADTN-treated group (Figure 10). This supports the ability of AbaCitDTN to deliver CitP to DC and induce a tolerogenic phenotype. The tolerogenic DC can disarm autoreactive T cells in an antigen-specific manner, leading to anergy of pathogenic T cells that recognize CitP as a self-antigen [6]. Thus, upon restimulation with CitP, pathogenic T cells could not respond efficiently, resulting in reduced pro-inflammatory cytokine secretion. In contrast, the AbaOVADTN-treated group, which delivered the irrelevant antigen OVA to DC, could not efficiently suppress CitP-specific immune responses due to the presence of remaining pathogenic T cells that recognize CitP as a self-antigen.

As secondary lymphoid organs, lymph nodes play a critical role in adaptive immune systems. To induce efficient immune tolerance to treat RA, antigen presentation by DC should be performed properly and rapidly within the lymph nodes. In this study, the nanoparticles were injected subcutaneously, which involves the injection of the nanoparticles below the dermis and epidermis. It is known that nanoparticles with a diameter of 10-100 nm are mainly taken up by lymphatics and transported to lymph nodes. On the other hand, nanoparticles larger than 100 nm tend to be trapped in the interstitial matrix at the injection site and require capture by skin DC to migrate to lymph nodes [41]. Since the size of CitDTN and AbaCitDTN is around 120 nm, they may not passively diffuse to the lymph nodes. However, AbaCitDTN exhibited rapid binding to skin DC and subsequently migrated to the lymph nodes within several hours after injection (Figure 11). In contrast, CitDTN had poor DC-binding ability and thus could not efficiently travel to the lymph nodes. Due to the limited ability of subcutaneously injected CitDTN to enter lymphatic circulation compared to AbaCitDTN, it may primarily enter the systemic circulation through capillaries, leading to limited distribution to other organs and retention at the injection site.

In order to assess the effectiveness of this tolerogenic nanovaccine for the treatment of RA, the CIA mouse model was used, which is the most widely used preclinical animal model for RA studies [25]. Joint damage that has occurred during the development of RA is irreversible. Therefore, early diagnosis and treatment are crucial to prevent and minimize further damage to the joints. To evaluate whether the nanovaccine could prevent or mitigate

the development of arthritis symptoms, a prophylactic treatment approach was used (Figure 12A), which involves administering the therapeutic agent prior to the onset of symptoms. The nanovaccine were injected subcutaneously at the center of the backs of mice every week for a total of four injections from the first day of administration of CII/CFA emulsion. Since RA is characterized by joint swelling and bone erosion, changes of paw thickness and bone architecture are key parameters for evaluating the progression of RA. The results showed that AbaCitDTN treatment ameliorated the RA symptoms and paw swelling of model mice, whereas the symptoms progressed in the other groups. Although treatment with AbaDTN, AbaCitDLN, and AbaOVADTN showed some prophylactic efficacy at the early stage, they were not able to prevent arthritic symptoms as efficiently as AbaCitDTN at the end of study (Figure 12). This indicated the importance of delivery of CitP to DC and inducing CitP-specific immune tolerance-mediated by AbaCitDTN. Clinically, three-dimensional visualization of bone erosion in RA patients using micro-CT offers convenience for diagnosis. The results showed that AbaCitDTN treatment ameliorated the RA symptoms and paw swelling of model mice, whereas the symptoms progressed in the other groups. Parameters measured by micro-CT, including BV/TV, BS/BV, and BMD, were similar between AbaCitDTN-treated and normal mice (Figure 13). Consistent with previous studies, the results showed that CIA model mice showed a low Foxp3$^+$ Treg population and abundant populations of IL-17A$^+$IFN-γ^+CD4$^+$ T cells and IFN-γ^+CD8$^+$ T cells in spleens (Figure 16). Efficient tolerogenic DC induction by AbaCitDTN was attributed to its ability to enhance Foxp3$^+$ Treg differentiation and suppress autoreactive CD4$^+$ and CD8$^+$ T cell differentiation.

In this study, the induction of immune tolerance was a critical aspect of AbaCitDTN treatment. However, this treatment should not negatively impact de novo immune responses against other antigens. To assess this, an influenza hemagglutinin model system was sued and the results showed that the administration of AbaCitDTN did not impair the development of neutralizing antibodies and hemagglutinin-specific IFN-γ-secreting cells. These results suggest that AbaCitDTN-induced immune tolerance against CitP did not interfere with the generation of defensive immune responses against non-CitP antigens.

Tolerogenic DC therapies have been investigated for their ability to treat various autoimmune diseases and support organ transplantation. Autologous tolerogenic DC loaded with B29 peptide for RA treatment have been studied in clinical trials that have entered phase II. However, the clinical application of injectable tolerogenic DC therapy is still challenging. The choice of autologous cell type and source is the first challenge in DC-based therapy. Although monocyte-derived DC have been used to generate ex vivo tolerogenic DC, they do not adequately represent the natural properties of DC in the human body. Also, the ex vivo manufacturing of tolerogenic DC

is time-consuming; this process includes cell harvesting, tolerogenic DC differentiation, and quality control before administration [42].

In this study, the phenotypes of DC were converted directly in the lymphatic systems by targeting two critical co-stimulatory molecules that are expressed on DC and involved in autoreactive T cell stimulation. CD80 and CD86, are predominantly expressed on APC and are considered to be specific biomarkers of activated DC. These results indicate that the rapid migration of AbaCitDTN into lymph nodes can initiate antigen presentation in a short period of time, thereby overcoming one main problem of DC-based therapy. Clinically, ex vivo-cultured DC have been administered via the intranodal route, which directly introduces DC to lymphoid organs. Intranodal injection is rarely used because it is a complicated procedure that requires anesthesia and ultrasound guidance [43]. In this study, nanovaccines were administered via subcutaneous injection, which is a friendly approach for vaccination in clinical settings.

Although AbaCitDTN were used to re-educate DC to a tolerogenic phenotype for RA treatment, this formulation could potentially be applied to other autoimmune diseases and organ transplantation. Instead of simply reducing local or systemic inflammation using anti-inflammatory drugs, the strategy of restoring immune tolerance using AbaCitDTN without causing systemic immune suppression offers a safe and efficient approach for RA treatment. CitP-loaded nanovaccines can rapidly traffic to the lymph node and induce antigen-specific immune tolerance toward RA, avoiding unwanted immune responses.

4.5. Conclusion

In summary, this research has developed a tolerogenic nanovaccine, AbaCitDTN, to effectively induce antigen-specific immune tolerance for treating RA. The efficient delivery of CitP and Dexa by tannic acid nanoparticles into DC was shown to reduce the expression of co-stimulatory molecules and the secretion of pro-inflammatory cytokines of DC. This resulted in the suppression of autoreactive T cells and promotion of Treg differentiation, thereby enabling the maintenance of peripheral tolerance and control of arthritis symptoms. Moreover, this approach overcomes the limitations of injectable tolerogenic DC-based therapy. Taken together, this research have proposed a highly promising nanovaccine system to accomplish the maintenance of peripheral tolerance without causing systemic immune suppression, showing potential for treating autoimmune diseases.

4.6. Reference

[1]   J. S. Smolen, D. Aletaha, A. Barton, G. R. Burmester, P. Emery, G. S. Firestein, A. Kavanaugh, I. B. McInnes, D. H. Solomon, V. Strand, K. Yamamoto. Rheumatoid arthritis. *Nat. Rev. Dis. Primers.* **2018**, *4*, 18001.

[2] Q. Guo, Y. Wang, D. Xu, J. Nossent, N. J. Pavlos, J. Xu. Rheumatoid arthritis: pathological mechanisms and modern pharmacologic therapies. *Bone Res.* **2018**, *6*, 15.

[3] J. S. Smolen, G. Steiner. Therapeutic strategies for rheumatoid arthritis. *Nat. Rev. Drug Discov.* **2003**, *2*, 473-88.

[4] S. Bindu, S. Mazumder, U. Bandyopadhyay, *Biochem. Pharmacol.* **2020**, *180*, 114147.

[5] S. Ness, S. Lin, J. R. Gordon. Regulatory Dendritic Cells, T Cell Tolerance, and Dendritic Cell Therapy for Immunologic Disease. *Front Immunol.* **2021**, *12*, 633436.

[6] A. Cifuentes-Rius, A. Desai, D. Yuen, A. P. R. Johnston, N. H. Voelcker. Inducing immune tolerance with dendritic cell-targeting nanomedicines. *Nat. Nanotechnol.* **2021**, *16*, 37.

[7] G. Steiner. Auto-antibodies and autoreactive T-cells in rheumatoid arthritis: pathogenetic players and diagnostic tools. *Clin. Rev. Allergy Immunol.* **2007**, *32*, 23-36.

[8] V. Malmström, A. I. Catrina, L. Klareskog. The immunopathogenesis of seropositive rheumatoid arthritis: from triggering to targeting. *Nat. Rev. Immunol.* **2017**, *17*, 60-75.

[9] E. R. Vossenaar, T. J. M. Smeets, M. C. Kraan, J. M. Raats, W. J. van Venrooij, P. P. Tak. The presence of citrullinated proteins is not specific for rheumatoid synovial tissue. *Arthritis Rheum.* **2004**, *50*, 3485-94.

[10] G. S. Firestein, I. B. McInnes. Immunopathogenesis of Rheumatoid Arthritis. *Immunity* **2017**, *46*, 183-196.

[11] S. Gertel, G. Serre, Y. Shoenfeld, H. Amital. Immune tolerance induction with multiepitope peptide derived from citrullinated autoantigens attenuates arthritis manifestations in adjuvant arthritis rats. *J. Immunol.* **2015**, *194*, 5674-80.

[12] X. Chen, G. Du, S. Bai, L. Dijia, C. Li, Y. Hou, Y. Zhang, Z. Zhang, T. Gong, Y. Fu, M. Bottini, X. Sun. Restoring immunological tolerance in established experimental arthritis by combinatorial citrullinated peptides and immunomodulatory signals. *Nano Today* **2021**, *41*, 101307.

[13] C. Li, X. Chen, X. Luo, H. Wang, Y. Zhu, G. Du, W. Chen, Z. Chen, X. Hao, Z. Zhang, X. Sun. Nanoemulsions Target to Ectopic Lymphoids

in Inflamed Joints to Restore Immune Tolerance in Rheumatoid Arthritis. *Nano Lett.* **2021**, *21*, 2551-2561.

[14] R. Lorenzetti, I. Janowska, C. R. Smulski, N. Frede, N. Henneberger, L. Walter, M.-T. Schleyer, J. M. Hüppe, J. Staniek, U. Salzer, A. Venhoff, A. Troilo, R. E. Voll, N. Venhoff, J. Thiel, M. Rizzi. Abatacept modulates CD80 and CD86 expression and memory formation in human B-cells. *J. Autoimmun.* **2019**, *101*, 145-152.

[15] L. Moreland, G. Bate, P. Kirkpatrick. Abatacept. *Nat. Rev. Drug Discov.* **2006**, *5*, 185-6.

[16] N. M. Edner, G. Carlesso, J. S. Rush, L. S. K. Walker. Targeting co-stimulatory molecules in autoimmune disease. *Nat. Rev. Drug Discov.* **2020**, *19*, 860-883.

[17] J. Mu, Y. Du, X. Li, R. Yan, H. Zhong, M. Cai, N. Yu, J. Zhang, X. Yuan, X. Hua, S. Guo. Collagen-anchored cascade nanoreactors with prolonged intratumoral retention for combined cancer starvation and chemotherapy. *J. Chem. Eng.* **2023**, *451*, 138554.

[18] H. Yang, Q.-V. Le, G. Shim, Y.-K. Oh, Y. K. Shin. Molecular engineering of antibodies for site-specific conjugation to lipid polydopamine hybrid nanoparticles. *Acta Pharm. Sin. B* **2020**, *10*, 2212-2226.

[19] İ. Gülçin, Z. Huyut, M. Elmastaş, H. Y. Aboul-Enein. Radical scavenging and antioxidant activity of tannic acid. *Arab. J. Chem.* **2010**, *3*, 43-53.

[20] H.-K. Lon, D. Liu, D. C. DuBois, R. R. Almon, W. J. Jusko. Modeling pharmacokinetics/pharmacodynamics of abatacept and disease progression in collagen-induced arthritic rats: a population approach. *J. Pharmacokinet. Pharmacodyn.* **2013**, *40*, 701-12.

[21] X. Bao, J. Zhao, J. Sun, M. Hu, X. Yang. Polydopamine Nanoparticles as Efficient Scavengers for Reactive Oxygen Species in Periodontal Disease. *ACS Nano* **2018**, *12*, 8882-8892.

[22] W. Li, Z. Liu, C. Liu, Y. Guan, J. Ren, X. Qu. Manganese Dioxide Nanozymes as Responsive Cytoprotective Shells for Individual Living Cell Encapsulation. *Angew. Chem. Int. Ed.* **2017**, *56*, 13661-13665.

[23] Y. Wu, Q. Li, G. Shim, Y.-K. Oh. Melanin-loaded CpG DNA hydrogel for modulation of tumor immune microenvironment. *J. Control. Release* **2021**, *330,* 540-553.

[24] D. Kim, Y. Wu, Q. Li, Y.-K. Oh. Nanoparticle-Mediated Lipid Metabolic Reprogramming of T Cells in Tumor Microenvironments for Immunometabolic Therapy. *Nanomicro. Lett.* **2021**, *13*, 31.

[25] D. D. Brand, K. A. Latham, Edward F Rosloniec. Collagen-induced arthritis. *Nat. Protoc.* **2007**, *2*, 1269-75.

[26] S. Hayer, M. J. Vervoordeldonk, M. C. Denis, M. Armaka, M. Hoffmann, J. Bäcklund, K. S. Nandakumar, B. Niederreiter, C. Geka, A. Fischer, N. Woodworth, S. Blüml, G. Kollias, R. Holmdahl, F. Apparailly, M. I. Koenders. 'SMASH' recommendations for standardised microscopic arthritis scoring of histological sections from inflammatory arthritis animal models. *Ann. Rheum. Dis.* **2021**, *80*, 714-726

[27] W. Wang, H. Wang, J. Zhao, X. Wang, C. Xiong, L. Song, R. Ding, P. Han, W. Li. Self-healing performance and corrosion resistance of graphene oxide–mesoporous silicon layer–nanosphere structure coating under marine alternating hydrostatic pressure. *Chem. Eng. J.* **2019**, *361*, 792.

[28] M. A. Ghalia, Y. Dahman. Radiation crosslinking polymerization of poly (vinyl alcohol) and poly (ethylene glycol) with controlled drug release. *J. Polym. Res.* **2015**, *22*, 218.

[29] A. Espina, S. Sanchez-Cortes, Z. Jurašeková. Vibrational Study (Raman, SERS, and IR) of Plant Gallnut Polyphenols Related to the Fabrication of Iron Gall Inks. *Molecules* **2022**, *27*, 279.

[30] M. A. Morini, M. B. Sierra, V. I. Pedroni, L. M. Alarcon, G. A. Appignanesi, E. A. Disalvo. Influence of temperature, anions and size distribution on the zeta potential of DMPC, DPPC and DMPE lipid vesicles. *Colloids Surf. B. Biointerfaces.* **2015**, *131*, 54-8.

[31] A. Derenne, T. Claessens, C. Conus, E. Goormaghtigh, in *Encyclopedia of Biophysics* (Eds: G. C. K. Roberts), Springer, Berlin/Heidelberg **2013**, pp. 1074-1081.

[32] K. D. Pile, G. G. Graham, S. M. Mahler, in *Compendium of Inflammatory Diseases* (Eds: M. J. Parnham), Springer, Basel **2016**, pp. 1-4.

[33] T. Saksida, B. Jevtić, N. Djedović, Đ. Miljković, I. Stojanović. Redox Regulation of Tolerogenic Dendritic Cells and Regulatory T Cells in the Pathogenesis and Therapy of Autoimmunity. *Antioxid. Redox Signal* **2021**, *34*, 364-382.

[34] R. Lu, X. Zhang, X. Cheng, Y. Zhang, X. Zan, L. Zhang. Medical Applications Based on Supramolecular Self-Assembled Materials From Tannic Acid. *Front. Chem.* **2020**, *8*, 583484.

[35] T. Liu, L. Zhang, D. Joo, S. C. Sun. NF-κB signaling in inflammation. *Signal Transduct. Target Ther.* **2017**, *2*, 17023.

[36] A. E. Morelli, A. W. Thomson. Tolerogenic dendritic cells and the quest for transplant tolerance. *Nat. Rev. Immunol.* **2007**, *7*, 610-21.

[37] Y. Xu, J. Mu, Z. Xu, H. Zhong, Z. Chen, Q. Ni, X. J. Liang, S. Guo. Modular Acid-Activatable Acetone-Based Ketal-Linked Nanomedicine by Dexamethasone Prodrugs for Enhanced Anti-Rheumatoid Arthritis with Low Side Effects. *Nano Lett.* **2020**, *20*, 2558-2568.

[38] M. Cai, Z. Xu, X. Zhou, L. Li, X. Hua, S. Guo, X. Yuan. Long-acting acid-sensitive ketal-linked dexamethasone microcrystals for treating experimental autoimmune uveitis. *APL Bioeng.* **2022**, *6*, 046101.

[39] J.-H. Lee, C.-S. Park, S. Jang, J.-W. Kim, S.-H. Kim, S. Song, K. Kim, C.-K. Lee. Tolerogenic dendritic cells are efficiently generated using minocycline and dexamethasone. *Sci. Rep,* **2017**, *7*, 15087.

[40] M. A. A. Jansen, R. Spiering, I. S. Ludwig, W. van Eden, C. M. U. Hilkens, F. Broere. Matured Tolerogenic Dendritic Cells Effectively Inhibit Autoantigen Specific CD4+ T Cells in a Murine Arthritis Model. *Front Immunol.* **2019**, *10*, 2068.

[41] A. Schudel, D. M. Francis, S. N. Thomas. Material design for lymph node drug delivery. *Nat. Rev. Mater.* **2019**, *4*, 415-428.

[42] C. M. U. Hilkens, J. D. Isaacs. Tolerogenic dendritic cell therapy for rheumatoid arthritis: where are we now? *Clin. Exp. Immunol.* **2013**, *172*, 148-57.

[43] C. Zeng, C. Zhang, P. G. Walker, Y. Dong, in mRNA Vaccines (Eds: D. Yu, B. Petsch), Springer Nature, Switzerland AG 2020, pp. 71-110.

Chapter 5

Summary

Chapter 5. Summary

In this Ph.D. dissertation, three nano-delivery systems were developed to effectively modulate immune cells and aimed to address limitations in current immunotherapeutic approaches for cancer and autoimmune diseases. Although immunotherapy has achieved significant success in clinics, there are still remaining challenges that require ongoing research and advancements to be made to improve the overall effectiveness of immunotherapy.

In Chapter 2, the research provides evidence that metabolic reprogramming of T cells can serve as a novel approach for anticancer immunometabolic therapy. It demonstrated that T cell targeting nanomedicine effectively enhanced the delivery of fenofibrate to T cells, leading to the activation of fatty acid oxidation metabolic pathways and restoration of mitochondrial functions in glucose-deficient environments of T cells. Moreover, lipid metabolic reprogramming of T cells in tumor tissues resulted in increased effector functions of T cells against tumor cells. This study underscores the potential of nanomedicine-enabled fatty acid metabolic reprogramming of tumor-infiltrating lymphocytes as an innovative strategy to overcome the hurdle of nutrient deficiency in immunotherapy.

In Chapter 3, the research demonstrates that the PIC-loaded mannose-conjugated nanovaccine could efficiently target lymph nodes and activate the immune system. The subcutaneous injection of the immunogenic nanovaccine showed a remarkable ability to target DC and facilitate their migration to lymph nodes, suggesting its potential as a promising vaccine delivery system. Considering the crucial role of DC in bridging the innate and adaptive immune systems, mannose-modified nanovaccine holds promise for inducing robust adaptive immune responses against infectious diseases or cancers.

In Chapter 4, a tolerogenic nanovaccine with properties to effectively induce antigen-specific immune tolerance for the treatment of RA was developed. The research demonstrates the efficient delivery of CitP and Dexa into DC using tannic acid nanoparticles, resulting in the reduction of co-stimulatory molecule expression and pro-inflammatory cytokine secretion by DC. This leads to the suppression of autoreactive T cells specific to self-antigens and the promotion of Treg differentiation, ultimately maintaining peripheral tolerance and controlling arthritis symptoms. Overall, this research presents a highly promising nanovaccine capable of maintaining peripheral tolerance without inducing systemic immune suppression.

Taken together, the development of nanomedicine for immunotherapy offers significant advantages in terms of targeted delivery, overcoming biological barriers, and immunomodulation. These advancements have the potential to revolutionize the field of immunotherapy, overcome the limitations associated with current immunotherapeutic approaches, and improve patient outcomes in the treatment of various diseases.

요약

암 대사 리프로그래밍 및 류마티스 관절염 백신을 위한 면역조절 나노의약품의 활용

서울대학교 대학원

약학과 약제학 전공

오예나

면역체계는 외부로부터 침입한 병원체를 비롯하여 각종 질환으로부터 우리 몸을 보호하는 중추적인 역할을 하고 있다. 하지만, 면역체계는 항상 완벽하게 작동하는 것이 아니며, 면역체계의 불균형으로 인한 과잉 혹은 결핍된 면역반응은 질환을 유발할 수 있다. 대표적으로 암은 면역 감시체계에 의하여 인지되지 못하여 제거되지 않고 비정상적으로 성장하는 종양 조직을 특징으로 하고 있다. 자가면역질환의 경우는 우리 몸에 존재하는 정상적인 항원 또는 비 병원성 항원에 대한 과잉 면역반응을 특징으로 한다. 그러므로, 면역체계의 불균형을 해소하여 암 또는 자가 면역질환과 같은 질환을 치료하는 전략은 중요하게 여겨진다. 나노의약품은 최신의 나노기술들을 도입하여 혁신적인 진단과 치료 방법들을 제시할 것으로 기대된다. 특정 세포 또는 조직을 표적화 할 수 있는 나노소재를 디자인하여 해당 병변으로 약물을 효과적으로 전달할 수 있다. 본 박사학위 논문은 세 가지 나노 약물전달 체계에 대한 개발과 연구에 대해서 다룰 것이며, 특히, 현재 사용되고 있는 암과 자가면역질환에 대한 면역치료요법의 한계점 극복에 초점을 맞추고 있다.

제 1장에서는 현재 임상에서 사용되는 암과 자가면역질환의 면역치료 전략에 대해서 다루고 있다. 또한 이러한 치료접근법들의 한계점에 대해서 살펴보고, 면역체계의 효율적인 조절을 위해 활용될 수 있는 나노약물전달시스템의 중요성에 대해서 중점적으로 설명하고 있다.

제 2장에서는 포도당이 결핍된 종양미세환경 내에서 나노의약품을 이용하여 T 세포의 지질대사 리프로그래밍을 유도하고 암세포에 대한 면역반응을 활성화하는 연구에 대하여 소개하고 있다. 본 나노의약품은 폴리감마글루탐산을 기반으로 한 나노 입자 내에 페노피브레이트를 봉입하고 있으며 (F/ANs) 표면에는 항−CD3 항체의 f(ab')2로 수식되어 있다 (aCD3/F/ANs). 이렇게 설계된 나노의약품은 T 세포의 지방산 대사를 자극하여 포도당이 결핍된 종양미세환경에서도 T 세포의 효과적인

증식에 도움을 줄 수 있고, 궁극적으로는 종양 조직 내에서 T 세포의 싸이토카인의 분비를 증진시키고 암세포의 성장을 억제할 수 있었다. 본 연구는 나노의약품을 활용한 종양 조직 내의 림프구들의 지방산 대사를 개선하는 항암치료전략의 잠재성에 대해서 강조하고 있으며, 이는 영양 결핍에 의한 한계점을 나타내고 있는 현재 항암면역치료요법의 돌파구가 될 것으로 기대된다.

제 3장에서는 만노오스로 수식되어 있는 양전하성 지질나노입자 (M-NP)를 이용하여 항원 제시 세포에 특이적으로 핵산면역증강제 폴리이노신산: 폴리시스티딜산 (PIC)을 전달하는 방법에 대한 연구에 대해 소개하고 있다. PIC가 탑재된 M-NP (PIC/M-NP)는 골수 유래 수지상세포에 대하여 매우 제한된 세포독성을 보이며 나노의약품에 수식된 만노오스의 비율에 따라서 수지상세포내 함입 율을 조절할 수 있음을 보여주고 있다. 또한, 본 나노의약품은 효과적으로 수지상세포의 성숙을 유도하며 피하 주사 시 림프절에 효율적으로 분포가 되는 것을 확인하였다. 따라서 본 연구는 만노오스로 수식되어 있는 나노 입자의 백신 전달치 로서의 가능성을 시사하고 있다.

제 4장에서는 탄닌산을 기반으로 설계한 나노 백신을 이용하여 항원 특이적인 면역 관용을 유도하고 류마티스성 관절염을 치료하는 전략에 대해서 소개하고 있다. 본 나노백신은 탄닌산 중심부에 지질로 표면을 감싸고 있으며 덱사메타손과 자가 항원 시트룰린산화 펩타이드를 탑재하고 있도록 설계하였다 (CitDTN). 또한, 본 나노 백신의 표면에는 아바타셉트를 결합하고 있다 (AbaCitDTN). AbaCitDTN은 수지상 세포를 효과적으로 면역 관용 성질을 갖도록 유도하였으며, T세포와 수지상세포 간의 공동자극분자 신호를 차단할 수 있으며 이는 T 세포의 증식을 저해하고 인터루킨-2의 분비를 효과적으로 억제하였다. DBA/1 mouse을 이용한 콜라겐 유도 관절염 동물모델에서 AbaCitDTN은 주 1회 피하 주사하였으며 총 4회를 주사하였다. 이는 윤활강 내의 염증반응을 완화하였으며 제 2형 콜라겐 및 시트룰린산화 펩타이드에 대하여 면역반응을 억제할 수 있었다. 이는 결과적으로 동물모델에서 류마티스 관절염에 대한 임상증상을 효과적으로 개선할 수 있었다. 본 연구결과는 탄닌산 기반의 나노 소재를 통한 항원 특이적 면역반응을 억제하여 류마티스성 관절염을 치료하고, 현재 활용되는 면역억제제들에 대한 부작용을 개선할 수 있다는 것을 보여주었다.

주요어 : 나노의약품, 면역 제어, 대사 리프로그래밍, 면역 관용 백신, 암, 류마티스 관절염
학번 : 2017-28204

감사의 글

어느덧 제가 박사졸업을 앞두고 이제 박사로서 앞으로의 길을 걷게 되었습니다. 지난 시간들을 되돌아보니 그래도 열심히 박사과정에 매진하였고 제 자신이 많이 성장하였다는 생각이 들어 뿌듯하기도 합니다. 이제 박사과정을 마무리를 하면서 그동안 저에게 도움과 응원을 주신 많은 분들께 감사의 말씀을 드리고 싶습니다.

우선 저를 지도해주시고 많은 응원과 격려를 해 주신 오유경 교수님께 깊은 감사의 말씀을 올리고 싶습니다. 교수님께서 부족한 저를 기다려 주시고 또 많은 기회를 주셔서 제가 성장할 수 있었습니다. 교수님께서 저에게 주신 격려의 말씀은 저에게 자신감을 심어 주셨고 또 저의 가능성을 열어 주셨습니다. 앞으로 교수님의 기대에 부응할 수 있는 여성 과학자로 발전하는 모습으로 교수님의 은혜에 보답하겠습니다.

심사과정 마지막까지 신경 써 주시고 저의 학위논문에 많은 조언과 좋은 말씀을 해 주신 김대덕 교수님께 깊은 감사의 말씀을 올리고 싶습니다. 교수님 덕분에 제가 졸업준비를 순조롭게 진행할 수 있었다고 생각합니다. 앞으로 더욱 발전한 모습으로 교수님의 은혜에 보답하겠습니다.

그리고 바쁘신 와중에 저의 학위 논문심사위원을 맡아 주신 변영로 교수님, 이우인 교수님, 윤유석 교수님, 심가용 교수님께 감사의 말씀을 드립니다. 교수님들께서 저에게 주신 조언은 앞으로 제가 연구자로서 나아가는 길에 큰 도움이 될 것이라고 생각합니다.

저를 학부때부터 많이 아껴 주시고 저의 시야를 넓혀 주신 Chang-qing Yang 교수님께 감사의 말씀을 드리고 싶습니다. 교수님께서는 저에게 더 넓은 세상에서 도전할 수 있는 용기를 주셨고 오늘의 제가 있다고 생각합니다. 앞으로 더욱 성장한 모습을 보여드릴 수 있도록 노력하겠습니다.

저희 NBD 가족들에게도 그 동안 감사했습니다. 저희 연구실의 기둥을 맡아 주신 이재우 박사님, 처음부터 실험을 가르쳐 주신 김동윤 박사님, 그 누구보다 연구에 대해 열정적인 Viet 박사님, 언제든 부탁하면 도움을 주신 변준호 박사님, 함께한 시간이 길지 않지만 저에게 많은 도움을 주신 김정석 박사님, 항상 저를 응원해주고 저의 작은 성취에도 함께 기뻐해준 진주언니, 묵묵히 연구를 열심히 수행하는 교운언니, 열정적으로 연구실 생활에 매진하는 재현이, 정이 많고 창의적인 남조씨, 연구에 대한 아이디어가 많은 동언이, 그리고 착한 우리 막내 은정이. 모든 분들께 감사의 말씀을 드립니다.

비롯 같은 연구실은 아니지만 멀지 않는 곳에서 저에게 많은 응원과 도움을 주신 하린언니, 성진오빠, 민준오빠, 승찬오빠, 성룡오빠, 주찬쌤, 영석오빠에게도 감사하다는 말을 전하고 싶습니다. 이렇게 멋진 분들을 만나게 되어 저의 행운이라고 생각합니다.

제가 하고 싶은 일을 항상 응원해주신 우리 아빠 엄마 너무 고맙고 사랑합니다. 항상 제 뒤에서 묵묵히 기대려 주고 그 어떤 상황에서도 제 편이 되어 주셔서 제가 실패를 두려워하지 않고 하고 싶은 일에 매진할 수 있었습니다. 아빠 엄마에게 자랑스러운 딸 그리고 지혜로운 사람이

될 수 있도록 노력하겠습니다. 제가 많이 사랑하는 우리 할아버지, 하늘에 게신 우리 할머니 많이 사랑하고 보고싶습니다. 그리고 항상 저를 응원하고 제 편이 되어준 진원오빠에게 감사하다는 말을 전하고 싶습니다. 연구자로 또 한 사람으로 많는 지혜를 가르쳐 줘서 너무 감사합니다.

　마지막으로 포기하지 않고 박사과정을 완주한 제 자신한테도 그 동안 수고했다고 말하고 싶습니다. 앞으로 더 많는 것을 경험하고, 도전하고 제가 좋아하고 성취감을 느끼는 일을 하는 삶을 살아 가기를 제 자신한테 바래 봅니다.

2023년 7월 7일
오예나 올림.